ANALYSES OF PRECIPITATION SIGNAL USING VHF VERTICALLY-POINTING RADAR

by

Edwin Campos

Department of Atmospheric and Oceanic Sciences

McGill University, Montréal, Québec, Canada

Submitted to the Faculty of Graduate and Postdoctoral Studies

in partial fulfillment of the requirements for the degree of Doctor of Philosophy

December, 2006

Your file Votre référence
ISBN: 978-0-494-32161-4
Our file Notre référence
ISBN: 978-0-494-32161-4

To my wife,

Adriana Quesada

CONTENTS:

ABSTRACT:

In addition to a proper radar calibration, quantitative estimation of precipitation from VHF radars requires the extraction of the precipitation signal out of the Doppler spectra. It also requires the proper conversion of this precipitation signal into a reflectivity factor.

This research develops a multi-faceted approach for the calibration of VHF vertically-pointing radars, by combining a first calibration method that compares the recorded VHF signal to power coming from a noise generator and a second calibration method that compares recorded VHF signal to cosmic radiation. This approach allows the retrieval of antenna and receiver parameters (such as noise levels, efficiency, and gain), and four other equations for the corresponding errors. In addition, we develop an equation for calibrating Doppler spectra.

The analysis is focused on rain observations with VHF radar. We verify the hypothesis that $|K|^2 = 0.93$ for most of the rain observations at VHF band. A signal-processing algorithm for extracting the rain signal out of the VHF power spectra is then presented. This work also derives a general version of the radar equation valid for vertically pointing radars, as well as a particular version of this equation valid for the McGill VHF radar. The study then makes numerical simulations of several profiles of precipitation signal at VHF band, by combining high-resolution profiles of precipitation signal (from a calibrated X-band radar) and the VHF antenna pattern in our general version of the radar equation. The analyses indicate that VHF reflectivity at gates above the melting layer is artificially enhanced by the precipitation signal collected from the side lobes.

This work also studies the effect of precipitation in the scattering properties of clear air. We analyze several cases of stratiform and convective rain, occurring in a continental mid-latitude environment (Montreal, Lat.45.41°N, Long.73.94°W). For these cases, Doppler spectra taken by a VHF vertically-pointing radar were used to retrieve simultaneous co-located values of precipitation intensity (rainrates) and degrees of refractive index fluctuation (structure-function parameter for refractivity turbulence, C_n^2). We validated these retrievals using co-located, calibrated measurements of precipitation signal at X-band. The comparison between equivalent reflectivity factors at X and VHF bands agrees within 1 dB. The study includes rainrates between 0.3 and 78 mm/h, and C_n^2 values between 10^{-16} and 10^{-12} $m^{-2/3}$, retrieved from the VHF spectra at 2.5 km height. The study finds that the occurrence of rain is associated with distinctive changes in the structure of air refractive index fluctuations, and that these changes are of a turbulent nature for the most intense rainrates.

RÉSUMÉ:

En plus d'une calibration appropriée, l'estimation quantitative des précipitations à partir de radars VHF nécessite l'extraction du signal précipitant du spectre Doppler. Ceci nécessite également une conversion adéquate de ce signal en facteur de réflectivité.

Ce travail de recherche a pour objectif de développer une approche multi-facette pour la calibration des radars VHF à visée verticale. Ceci est réalisé en combinant deux méthodes de calibration : la première méthode compare le signal VHF enregistré au le signal issu d'un générateur de bruit et la seconde compare le signal VHF enregistré aux radiations cosmiques. Cette approche permet de restituer les paramètres de l'antenne et du récepteur (comme le niveau de bruit, efficacité, et le gain), ainsi que les équations des erreurs correspondantes. De plus, nous avons développé une équation pour calibrer le spectre Doppler.

Cette étude est axée sur des observations de pluie d'un radar VHF. Nous avons vérifié l'hypothèse $|K|^2 = 0.93$ pour la pluie en bande VHF. Un algorithme de traitement du signal permettant d'extraire le signal de pluie des spectres Doppler VHF est présenté. Ce travail présente également une version générale de l'équation radar, valide pour les radars a visée verticale, ainsi qu'une version spécifique de cette équation dédiée au radar VHF de McGill. Des simulations numériques de quelques profils de signaux précipitant en bande VHF, sont réalisées en combinant des profils de fines résolution issus de radar bande X calibrés et du champ d'antenne VHF de notre équation radar générale. L'analyse indique que la réflectivité radar VHF au dessus de la zone de fonte est artificiellement augmentée par le signal précipitant provenant de la direction des lobes secondaires.

Cette étude est également axeé sur l'effet des précipitations sur les propriétés de rétrodiffusion de l'air clair. Nous analysons certains cas de pluies stratiformes et convectives, survenus dans un environnement continental de moyenne latitude (Montréal, Lat.45.41°N, Long.73.94°O). Pour ces différents cas, le spectre Doppler issu du radar VHF à visée verticale a été utilisé pour restituer simultanément les valeurs d'intensité des précipitations (taux de pluie) et la fluctuation de l'index de réfraction (paramètres de la fonction de réfractivité turbulente, C_n^2). Nous avons validé ces restitutions en utilisant des mesures co-localisées de précipitations, issues de radars en bande X calibrés. La comparaison entre les facteurs de réflectivité équivalente radar en bandes X et VHF sont en bon accord, à 1dB près. L'étude prend en compte des taux de précipitations variant entre 0.3 et 78 mm/h et des valeurs de C_n^2 comprises entre 10^{-16} et 10^{-12} $m^{-2/3}$, celles-ci étant restituées à partir du spectre VHF à 2.5 km d'altitude. Il a été montré que l'occurrence des précipitations est associée avec les changements de structures de l'index de réfraction de l'air et que ces changements sont de nature turbulente pour les taux de précipitations les plus intenses.

RESUMEN:

Además de una adecuada calibración del radar, la estimación cuantitativa de la precipitación a partir de radares VHF requiere de la extracción de la señal de precipitación en el espectro Doppler. También se requiere una conversión apropiada de esta señal de precipitación al factor de reflectividad de radar.

Esta investigación desarrolla una estrategia mixta para la calibración de radares VHF que apunten verticalmente, la cual combina un primer método de calibración que compara la señal registrada en VHF y la potencia proveniente de un equipo generador de señal ruido, así como un segundo método de calibración que compara la señal registrada en VHF con la radiación cósmica. Esta estrategia permite obtener los parámetros de la antena y el receptor (tales como los niveles de ruido, eficiencia y ganancia), así como las ecuaciones para calcular los errores respectivos. Además, se desarrolla una ecuación para la calibración del espectro Doppler.

El análisis se enfoca en observaciones de lluvia con radar VHF. Se verifica la hipótesis de que $|K|^2 = 0.93$ para la mayoría de las observaciones de lluvia en la banda VHF. Se presenta un algoritmo de procesamiento de la señal para extraer la señal de lluvia a partir del espectro de potencias en VHF. Este trabajo también deriva una versión general de la ecuación del radar, válida para radares que apuntan verticalmente, así como una versión particular de esta ecuación válida para el radar VHF de McGill. Este estudio continúa haciendo simulaciones numéricas de varios perfiles de la señal de precipitación en la banda VHF, mediante la combinación de perfiles de señal de precipitación a alta resolución (obtenidos con un radar en banda X, previamente calibrado) y el patrón de dispersión de la antena, ambos combinados en nuestra versión general de la ecuación del radar. Los análisis indican que la reflectividad en VHF, para rangos arriba del nivel de fusión, queda artificialmente aumentada por la señal de la precipitación que es recogida en la dirección de los lóbulos laterales del patrón de la antena.

Este trabajo también estudia el efecto de la precipitación en las propiedades de dispersión del aire claro. Se analizan varios casos de lluvia estratiforme y convectiva, que ocurren en un ambiente continental de latitudes medias (Montreal, Lat.45.41ºN, Long.73.94ºO). Para estos casos se utiliza el espectro Doppler, obtenido por un radar VHF que apunta verticalmente, para obtener valores correspondientes de la intensidad de precipitación (lluvia) y el grado de fluctuación en el índice de refracción (el parámetro de la función estructura para la refractividad por turbulencia, C_n^2). Se validan estas estimaciones utilizando medidas calibradas de la señal de la precipitación en la banda X, las cuales son simultáneas y representativas de un volumen similar a las medidas en VHF. La comparación entre los factores de reflectividad equivalente en bandas X y VHF concuerda dentro de 1 dB de diferencia. El estudio incluye intensidades de lluvia entre 0.3 y 78 mm/h, así como valores de C_n^2 entre 10^{-16} y 10^{-12} $m^{-2/3}$, todos obtenidos a partir de espectros en VHF a una altura de 2.5 km. El estudio encuentra que la ocurrencia de lluvia está asociada con cambios distintivos en la estructura de las fluctuaciones del índice de refractividad del aire, y que estos cambios son de naturaleza turbulenta para las lluvias más intensas.

STATEMENT OF ORIGINALITY:

Elements of this thesis that constitute original scholarship and an advancement of knowledge are the following:

- Development of a multi-faceted approach for the calibration of VHF (vertically-pointing) radars, which provides the values and uncertainties for various antenna and receiver parameters (such as noises, efficiency, and gain).

- Development of a signal-processing algorithm to retrieve rain intensity, air-turbulence signal, and vertical air velocities, all these over the same sampling volume and using only observations from a VHF radar.

- Derivation of a general version of the radar equation, which is valid for vertically-pointing radars with targets within a few kilometers range, but still within the antenna far-field region.

- Development of a numerical model to simulate how the scatter signal received through antenna sidelobes can affect the measured profile of precipitation reflectivity.

- Analysis of a unique dataset for rainrates, vertical air velocities, and air-turbulence signals (simultaneously measured during several rain events, typical of continental mid-latitude environments), which illustrates how rain affects the scattering properties of the clear air.

CONTRIBUTION OF AUTHORS:

Chapters 2, 3 and 4 of this thesis have been submitted for publication into the journal *Radio Science* (chapters 2 and 3) and the *Journal of Atmospheric and Oceanic Technology* (chapter 4). Professors Frederic Fabry and Wayne Hocking supervised all these studies. For these chapters, the antenna pattern computations for the McGill VHF radar are based on a computer model developed by Prof. Hocking. The analyses presented in Section 2.4 were provided by Professor Hocking. Figures 5.3, 5.4, 5.5 and 5.6 were generated by Professor Fabry. The thesis author provided the rest of the contributions.

ACKNOWLEDGMENTS:

I wish to thank my thesis supervisors, Prof. Frédéric Fabry (McGill University) and Prof. Wayne Hocking (University of Western Ontario), for their patience, guidance, and financial support throughout this project.

I am also indebted to Dr. Bernard Campistron, from the Aeronomy Laboratory at the Midi-Pyrénées Observatory, Université Paul Sabatier (Lannemezan, France), for providing the sky survey datasets by *Campistron et al.* [2001] and by *Milogradov-Turin and Smith* [1973]. Dr. Tom Landecker, from the Dominion Radio Astrophysical Observatory (Penticton, British Columbia, Canada), kindly provided me with the sky survey dataset by *Roger et al.* [1999].

The VHF- and X-band radars, as well as the POSS distrometer, which I used in this research are operated and funded by the Marshall Radar Observatory of McGill University, under the direction of Prof. Isztar Zawadzki. The computer code used in this work for reading the VHF Doppler spectra is based on an early program by Dr. Monique Petitdidier, from the *Centre d'Etudes des Environnements Terrestre et Planétaires* (Vélizy, France). The author also appreciates the collaboration given by Dr. Trevor Carey-Smith, from the Air Quality Research Branch at the Meteorological Service of Canada (Downsview, Ontario, Canada), when taking the antenna-matching measurements in Figure 2.14 and Table 2.3. I am also grateful to Dr. Barry Turner, from the Department of Atmospheric and Oceanic Sciences at McGill University, for proofreading several portions of this thesis. For permission to use Figures 1.1 and 1.2, I thank the American Meteorological Society.

I owe a debt of gratitude to my wife Adriana Quesada, the person with whom I found material and spiritual support. She nourished me with consent, advice and love, while we walked together this Ph.D. trail. To her I dedicate this thesis.

LIST OF SYMBOLS:

The following symbols are those used most frequently in this thesis.

au	Digital units of the analog-to-digital converter in the radar receiver
A_e	Antenna effective area (in m^2)
A_{NG}	First radar-calibration coefficient (the constant, in Watts), from the noise-generator method
A_{sky}	First radar-calibration coefficient (the constant, in Watts), from the sky-noise method
B_{NG}	Second radar-calibration coefficient (the slope, in W/au), from the noise-generator method
B_{sky}	Second radar-calibration coefficient (the slope, in W/au), from the sky-noise method
BPF_{width}	Band-pass filter width of the radar receiver (in Hz)
c	Speed of light in a vacuum
c'	Speed of light in the atmosphere
C_n^2	Structure-function parameter for refractivity turbulence (in $m^{-2/3}$)
dA_t	Finite area that is perpendicular to the direction of the radar-transmitted radiation.
dA_s	Average scattering cross-section of radar targets.
D	Antenna directivity
D_{max}	Antenna maximum directivity
D_e	Equivalent-spherical raindrop diameter (in mm)
DSR	Doppler spectral range (in Hz), corresponding to those spectral frequency bins recorded after signal processing
e	Antenna efficiency
e_R	Antenna efficiency during reception of radar signal
e_T	Antenna efficiency during transmission of radar signal
e_v	Water-vapour pressure (in mb or Pa)
f	Doppler frequency shift (in Hz)
f_j	Doppler frequency at the j-th spectral bin, corresponding to the clear-air peak (in Hz)
$f_{\min}$	Smallest Doppler frequency of retrieved precipitation spectrum
f_{precip}	Doppler frequencies in the precipitation spectrum (in Hz)
f_R	Radar operating frequency (in Hz)
$f_{sampling}$	Radar sampling rate (in Hz)
f_0	Relaxation frequency of pure water
F	Normalized one-way antenna polar-diagram (or antenna pattern)
F_{NG}	Factor of the noise-generator hardware (one unit increment in F_{NG} corresponds to 290 Kelvins increase in brightness temperature)
g	Shape of transmitted pulse (as a function of range)
G	Antenna gain
g_{Rx}	Receiver gain (in au/W)
$k_{Boltzmann}$	Boltzmann constant (1.381×10^{-23} J/K)

l_0	Transition scale between viscous and inertial subranges of turbulence (i.e., the Inner scale)
L	Transmitted pulse length (in m)
L_B	Transition scale between inertial and buoyancy subranges of turbulence
L_0	Outer scale of turbulence (inside the inertial subrange)
m	Complex refractive index for a given scatterer
M	Vertical gradient of the potential refractive index
n	Atmospheric refractive index
n	Number of spectral bins
n'	Real part of the complex refractive index, for a given scatterer
n''	Imaginary part of the complex refractive index, for a given scatterer
N	Drop size distribution (in mm^{-1} m^{-3})
N_a	Antenna noise (in Watts)
N_{coh}	Number of samples used for coherent averages during radar signal processing
N_e	Number density of free electrons (in m^{-3})
N_{Rx}	Receiver noise (in au)
p	Atmospheric pressure (in mb or Pa)
P_{cal}	Calibrated received power (in Watts)
P_{NG}	Power input by the noise generator into the radar receiver (in Watts)
P_{out}	Digital value of the total received power (in arbitrary units), output by the computer after signal processing, and corresponding to the integral of S_{out}.
P'_{out}	Digital value of the received power (in arbitrary units), in the recorded spectral range, corresponding to the integral of S'_{out}.
P_r	Backscatter power input into the radar antenna
PRF	Pulse repetition frequency (in Hz)
P_{Rx}	Power output from the antenna into the receiver hardware
P_{sky}	Sky power (from cosmic radio emissions, in Watts)
P_t	Power transmitted by the radar antenna into the space
P_{Tx}	Power transmited by the radar transmitter into the antenna
r	Range to scatterer, as variable
R	Range, as constant (in m)
R	Rainfall rate (in mm/h)
S	Doppler spectral density
S_{cal}	Calibrated power-density spectra (in W/Hz)
S_{precip}	Doppler power density of precipitation signal
S_{POSS}	Doppler spectrum of reflectivity factors from POSS measurements
S_{VHF}	Doppler spectrum of reflectivity factors from VHF precipitation signals
S_{out}	Full spectral density (in au/Hz), corresponding to Doppler frequencies within $\pm 0.5\, f_{\text{sampling}}$
S'_{out}	Stored Doppler spectra (in au/Hz), corresponding to Doppler frequencies within $\pm 0.5\, DSR$
T	Temperature (in Kelvins or degrees Celsius)
T_{Rx}	Receiver noise temperature (in Kelvins)
v	Doppler velocity (in m/s)
v_T	Terminal fall velocity (in m/s) of a raindrop at any given height

v_0	Raindrop terminal fall velocity (in m/s) at sea level
V	Radar sampling volume
Z	Radar reflectivity factor (in mm^6 m^{-3})
Z_e	Equivalent reflectivity factor (in mm^6 m^{-3})
Z_{POSS}	Reflectivity factor from POSS measurements (i.e., S_{POSS} integration)
Z_{VHF}	Reflectivity factor from VHF measurements (i.e., S_{VHF} integration)
β	Spectral index (for our studies, it is approximately equal to 2.5)
Δf	Bin resolution of the Doppler spectra (in Hz)
$<\Delta n^2>$	Mean square fluctuations of the refractive index
Δr	Width of radar range gate (in meters)
ε	Turbulent energy dissipation rate (in m^2 s^{-3})
ξ	Relative dielectric constant
ξ'	Real part of the relative dielectric constant (i.e., the relative permittivity)
ξ''	Imaginary part of the relative dielectric constant (i.e., the lost factor)
ξ_s	Static dielectric constant
ξ_∞	High-frequency dielectric constant
ς	Amplitude reflection coefficient of a refractive-index discontinuity
$\lvert K\rvert^2$	Scatterer dielectric factor
λ	Radar wavelength (in m)
η	Radar reflectivity (in m^{-1})
η_{precip}	Radar reflectivity from precipitation signal (in m^{-1})
Ω_M	Solid angle of the one-way main lobe
Ω_p	Solid angle of the one-way full-antenna-pattern
ϕ	Azimuth angle (in degrees or radians)
ρ	Air density at a given height (in kg m^{-3})
ρ_0	Air density at sea level (in kg m^{-3})
σ_{AIR}	Spectral width of clear-air Doppler spectrum (in m/s)
$(\sigma_+)_i$	Back-scattering cross section of the *i*th isotropic scatterer
θ	Zenith angle (in degrees or radians)
θ_S	Aspect sensitivity factor (in degrees)
θ_t	Zenith angle of an off-vertical tilt direction
θ_0	One-way half-power half-beamwidth (in degrees or radians)
ω_B	Brunt-Vaisala frequency (in Hz)

CHAPTER 1:

INTRODUCTION

1.1. Motivation

While precipitation intensity is one of the most important scalars measured in meteorology, the wind can be consider as the most important meteorological vector to be measured. There is a sensor that has the potential to achieve simultaneous measurements of precipitation and wind. Consider for example vertical velocities. Although these are difficult to measure, they can be determined from the Doppler velocity obtained by clear-air-sensitive radars pointing vertically. Furthermore, by alternating the direction of the transmitter and receiver antenna beam, in at least two particular off-vertical directions, it is possible to construct time series of the vertical profile of the 3-D wind above the radar. These radars have also the potential of receiving additional signal from precipitation.

The radars described in the previous paragraph are called wind profilers, and their measurements are used in fields such as air traffic safety, weather numerical modeling, severe weather forecasting, and pollution dispersion [e.g., *Benjamin et al.*, 2004]. Applications of wind profilers also include climatic analysis of long-term variations in the wind field, as well as diagnosis and forecasting of the severity of specific events (e.g. atmospheric waves, clear-air turbulence, and mesoscale convective systems). The real-time monitoring of wind profiles can provide information related to air pollution, air traffic hazards, and safety in high-risk areas such as chemical and nuclear plants. Furthermore, radar wind profiles could be assimilated into numerical models of continental-scale and local weather, as well as air pollution. A single wind profiler or a network may be used in connection with other instruments and models to describe specific phenomena such as fronts, topographic induced effects, and exchange of air masses between the troposphere and the stratosphere.

Traditionally, radar meteorology applied to precipitation physics has been done mainly using the microwave band (electromagnetic wavelengths between 1 m to 1 mm, or frequencies between 300 MHz and 300 GHz; *AMS* [2000]). However, wind-profiler radars operating at VHF band (wavelengths between 10 m to 1 m, or frequencies between 30 MHz and 300 MHz) may present some advantages since they measure backscatter from both clear air and precipitation. (Both signals produce independent contributions in VHF Doppler power spectra.) It is then possible to quantify the amounts of precipitation and clear air turbulence.

Unfortunately, precipitation signal has been traditionally considered as clutter (unwanted echoes) by the VHF community. Thus, most of the VHF signal processing and analysis have avoided the treatment of the precipitation signal. This research proposal will proceed differently by identifying the potential that VHF radars have in the study of precipitation physics.

It is also a very opportune time to pursue this line of research, since the McGill University radar observatory has recently acquired a VHF wind profiler [described in *Campos and Hocking*, 2003]. Although the radar design is such that its mode of operation requires some modification in order to retrieve meteorological information other than winds, this radar was able to perform the data collection for this research. Furthermore, extensive data were available to complement these VHF measurements, from other instruments co-located at the McGill VHF site (e.g. raindrop sizes at ground and Doppler spectra from an X-band, vertically-pointing radar).

The next section will discuss the basic scientific principles involved in the operation of VHF radars. The final section will state the scientific problems to be addressed in this Thesis, which includes the objectives and detailed plan of this research.

1.2. Literature review

Radars that operate with electromagnetic radiation of wavelengths between 1 and 10 m (frequencies between 300 and 30 MHz) are called VHF (Very High Frequency) radars. Using VHF electromagnetic waves allows simultaneous detection of "clear air" signals as well as precipitation signals. By transmitting and receiving electromagnetic waves that propagate in the vertical direction, VHF radars are capable of measuring signals returned from the troposphere, stratosphere, and in some cases even from the mesosphere. Due to these capabilities, they have also been called MST (Mesosphere-Stratosphere-Troposphere) radars, ST (Stratosphere-Troposphere) radars, clear-air radars, and wind profilers.

In addition to the basic capabilities, VHF radars can be optimized to produce measurements of one or more of the following meteorological variables [see

Röttger and Larsen, 1990, and references therein]: 3-D wind, momentum flux, turbulence, Rainfall Drop-Size Distributions (DSDs), temperature and humidity profiles, and lightning. Later in this thesis, we will discuss some important methods to retrieve fundamental atmospheric variables from VHF radar observations.

The capabilities of the VHF radar make it a valuable tool for the study of cloud formation and precipitation development. In fact, the understanding of these processes is the fundamental goal of cloud physics.

1.2.1. General backscatter radar equation

In general, electromagnetic waves transmitted by the radar will be backscattered (or reflected) by the propagating medium according to the radar equation. (The Appendix and Chapter 3 will consider a general form of the radar equation; however, the current Chapter 1 will use a simplified form of the radar equation, which facilitates the introduction of some basic concepts.) For a Gaussian beam pattern, and for scatterers in the far-field being uniformly distributed throughout the entire volume (from which power is scattered back to the receiver), a simplified form of the radar equation can be given by [e.g., *Balsley and Gage*, 1980]

$$P_r = \frac{e^2 \, P_{Tx} \, A_e \, \Delta r}{8\,\pi} \left(\frac{\eta}{r^2} \right) ; \tag{1.1}$$

where P_r (in units of watts) is the average returned power, e is an efficiency factor for the antenna transmission lines, P_{Tx} (in watts) is the transmitted power,

A_e is the effective antenna area, and Δr is the range gate width. The value of η (in m^{-1}) is the radar reflectivity per unit volume, and r (in meters) is the range.

The radar reflectivity is determined by the scattering elements present in the sampling volume (the medium through which the electromagnetic wave propagates). Thus, the radar reflectivity is defined in terms of the total backscattering cross-sectional area as [e.g., *Battan*, 1973, equation 4.8]

$$\eta \equiv \frac{\sum_{vol} (\sigma_+)_i}{vol} ; \tag{1.2}$$

where $(\sigma_+)_i$ is the back-scattering cross section of the ith isotropic scatterer, and *vol* is the sampling volume (i.e., the entire volume from which power is scattered back to the receiver at any instant). Note that, strictly speaking, the propagating medium may also produce reflection in addition to scatter.

Whether the scatter elements are solid, liquid, gas, or plasma, the theory is similar. The special appealing of the VHF radar resides in its capability to differentiate the backscatter from clear air from the signal due to precipitation particles (and even from lightning). We will discuss these capabilities in the following sections.

1.2.2. Scattering from clear air

1.2.2.1. Refractive index

As the electromagnetic wave propagates in a medium, or as it passes through the interface between two media, the wave is affected by the composition changes of the medium. These density changes produce changes in the speed of propagation of the electromagnetic wave. For instance, the speed of the wave may slow down while the frequency stays constant. As a consequence, the direction of energy propagation can be changed. This is called refraction. The amount of refraction is determined by the atmospheric refractive index, n, and this index is defined by [e.g. *Rottger and Larsen*, 1990, eqn.1]

$$n \equiv \frac{c}{c'} = 1 + 77.6\times10^{-6}\,\frac{p}{T} + 3.73\times10^{-1}\,\frac{e_v}{T^2} - 40.3\,\frac{N_e}{f_R^{\,2}}\ ; \tag{1.3}$$

where c' is the actual wave speed and c is the speed of light in a vacuum. The value p is the atmospheric pressure (in mb), T is the absolute temperature (in Kelvin), e_v is the partial pressure of water vapor (vapor pressure, in mb), N_e is the number density of free electrons (in m^{-3}), and f_R is the radar operating frequency (in Hz; $f_R = c'/\lambda \approx c/\lambda$, and λ is the radar wavelength). Note that the term dependent on N_e needs not to be considered for heights below the mesosphere. With respect to the refractive index gradient, the term proportional to e_v is most important in the lower troposphere, while the term proportional to p dominates in the upper troposphere and the stratosphere.

For a given volume (the one sampled by the VHF radar), the refractive index gradients occur due to: (a) mixing of the vertical profile of refractive index by atmospheric turbulence, and / or (b) the presence of a boundary between two distinct stratified layers. Scattering and reflection processes associated with vertical gradients of refractive index will be discussed in the following subsections.

1.2.2.2. Scattering models

Scattering of electromagnetic waves can be produced by fluctuations of n. Models for scattered power based on turbulent mixing of n can be traced back to *Megaw* [1957], *Silverman* [1956], *Booker and Gordon* [1950], and many others. However, the theory is brought together in a general framework by *Tatarski* [1961]; he provides the context of electromagnetic wave propagation through turbulent media. Specific applications to backscattering from the clear atmosphere have been considered by *Atlas et al.* [1966] and *Ottersten* [1969 and 1969c]. Experimental confirmation of the theory was forthcoming in a series of experiments conducted at Wallops Island [*Kropfli et al.*, 1968], in Virginia, USA.

There is not yet a complete model that explains all the backscattering mechanisms observed with VHF radiation in clear air. However, we can simplify the problem by considering a few basic scattering and reflection mechanisms that explain various aspects of the observed radar echoes. These basic mechanisms include scattering from isotropic turbulence, scattering from anisotropic turbulence, Fresnel reflection from isolated layers, and Fresnel scattering from multiple stable layers. They provide statistical estimates of the magnitude of backscattered power that can be useful in designing new radar systems. Furthermore, these mechanisms provide a rationale for relating backscattered power to atmospheric parameters (such as eddy dissipation rate and atmospheric stability).

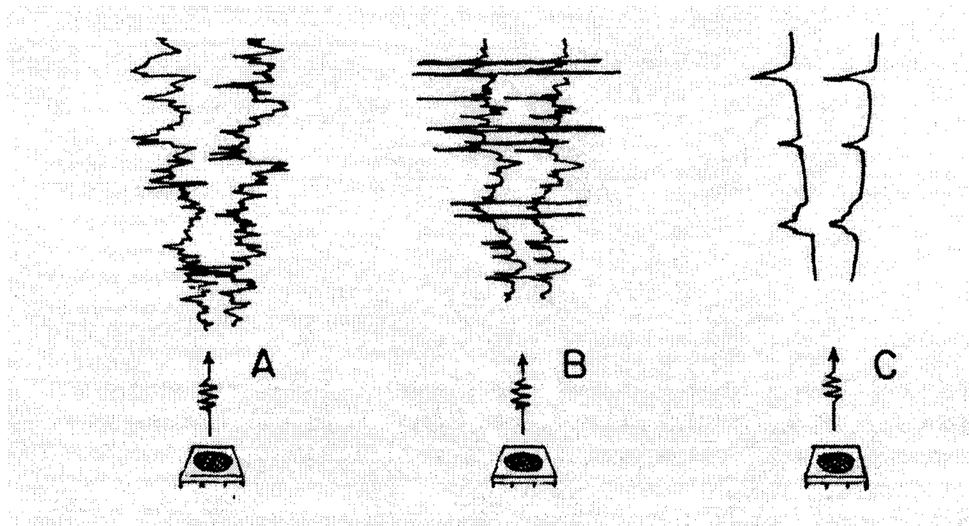

Figure 1.1. Three different vertical profiles of the refractive index gradient (as observed by a VHF radar). In each panel, two nearby vertical profiles of *dn/dz* illustrate the structure illuminated by the radar beam. Panel A illustrates isotropic turbulence pertinent to isotropic turbulence scattering. Panel B illustrates random yet transversely coherent structure pertinent to Fresnel scattering. Panel C illustrates a few isolated sharp coherent gradients pertinent to Fresnel reflection. [From *Gage*, 1990.]

In order to explain these simplified backscattering mechanisms, let us first analyze the profile of refractivity in the atmosphere. As an idealized picture of the refractivity structure in the atmosphere, Figure 1.1 shows different vertical profiles of the refractive-index vertical gradients, *dn/dz*. Three different panels are presented, where each one characterizes a particular simplified model of scattering. In each panel, two vertical profiles of *dn/dz* illustrate the structure illuminated by the radar beam. In panel A, the beam illuminates a volume of turbulence with random structure evident in the radio refractive index. There is no pronounced horizontal coherency in the case of active turbulence (i.e., the two random profiles of refractive-index gradient are not significantly correlated). This pattern of refractive-index gradient is related to the so-called Turbulence scattering. A much different structure is illustrated in panel C, where isolated sharp gradients that are horizontally coherent are shown. Each layer would cause a partial reflection of an incident radar pulse. This second pattern is associated to Fresnel reflection. An intermediate example of atmospheric structure is illustrated in panel B. In this case, the profile illustrates randomness in the vertical but maintains some horizontal coherence. This structure is thought to be pertinent to a multiple partial reflection process that will be referred to as Fresnel scattering.

1.2.2.2.1. Turbulence scatter

The principal scattering mechanism was introduced to tropospheric radio propagation by *Booker and Gordon* [1950] and has been extended to include radar backscattering from the clear air by *Ottersten* [1969, 1969b and 1969c]. The process is called turbulence scatter. This type of backscatter was also named Bragg scatter [*Gossard et al.*, 1982] because of its similarity to X-ray diffraction in crystals, as originally put forward by Sir Lawrence Bragg and his father, Sir William Bragg, for which they jointly received the 1915 Nobel Prize in Physics.

Turbulence scatter can be isotropic if the turbulent irregularities of the refractive index are homogeneously random and statistically similar in all directions (homogeneous and isotropic). Turbulence scatter can be anisotropic if the statistical properties of the irregularities, namely their correlation distances, are dependent on direction. The angular (spatial) dependence of the radar echoes is called the aspect sensitivity, and it can be different for isotropic and anisotropic turbulence scatter. Isotropic turbulence scatter does not cause an aspect sensitivity, while anisotropic turbulence scatter does cause an aspect sensitivity [e.g., *Hocking and Hamza*, 1997]. The temporal variations of the radar echoes should be similar in both isotropic and anisotropic turbulence scattering. This is due to the randomly fluctuating irregularities, and the Doppler spectrum should show a shape that is approximately Gaussian.

In these cases, the magnitude of the backscattered echo from the clear atmosphere depends on the intensity of refractivity turbulence, which is parameterized by [e.g., *Hocking*, 1985, p.1405]

$$C_n^{\ 2} = \frac{\overline{|n(\mathbf{x}+\mathbf{r}) - n(\mathbf{x})|^2}}{|\mathbf{r}|^{2/3}} \ ; \tag{1.4}$$

where **x** represent a position vector, **r** a spatial displacement, and the average is over space and time. Here C_n^2 (in units of $m^{-2/3}$) is the structure-function parameter for refractivity turbulence, and it is defined for locally homogeneous isotropic turbulence in the inertial subrange by [*Ottersten*, 1969]:

$$C_n^{\ 2} = a <\Delta n^2> L_0^{-2/3} \ ; \tag{1.5}$$

where a is a constant (about 5), $<\Delta n^2>$ is the mean square fluctuations of the refractive index, and L_0 is the outer scale of turbulence in the inertial subrange, which is proportional to the square root of the turbulent energy dissipation rate ε and the -3/2 power of the buoyancy frequency ω_B.

The radar reflectivity for scattering from volume-filling, isotropic turbulence in the inertial subrange is given in terms of C_n^2 by [*Ottersten*, 1969c]:

$$\eta = 0.38\, C_n^{\ 2}\, \lambda^{-1/3} \ ; \tag{1.6}$$

where λ is the radar wavelength (in units of meters).

It should be noted that the assumption of isotropic turbulence is questionable for the wavelength range that characterizes VHF radars. In reality, these clear-air scatterers are anisotropic, twisted, contorted, string-like structures, which have a broadly ellipsoidal shape on average [e.g., *Hocking*, 1997b; *Hocking and Hamza*, 1997]. The effect of this anisotropy is to produce underestimates of the mean wind. To illustrate this, consider the fact that the scatter is preferentially produced from angles closer to overhead than the true angle of the radar transmitted beam [e.g., *Hocking*, 1997b]. Thus when horizontal velocities are estimated from a relation such as $v_{horizontal} = {}^{v_{radial}}\!/_{\sin\theta}$, where θ is the true zenith angle of the transmitted beam, then the computed horizontal wind speed is an underestimate.

Equation (1.6) is appropriate only if the scales of refractive index fluctuations (of size equal to half the radar wavelength) lie within the inertial subrange of the spectrum of turbulence. In this range, the rate at which turbulent energy is transferred to smaller scales as larger eddies fragment depends only on the dissipation rate ε of turbulent energy. However, as the scale becomes smaller, the kinetic energy density of the eddies is diminished due to viscous effects, and much of the turbulent energy is dissipated as heat. This small scale range is often called the 'viscous' (or dissipation) range. In this scale range, the radar power density spectrum decreases more rapidly with decreasing turbulence intensity than for scales within the inertial subrange. The transition between inertial and viscous ranges is defined by the scale where the kinetic energy starts to be lost as heat. This is l_0, the inner scale for density fluctuations. In the troposphere, this transition scale is roughly between 3×10^{-3} m and 2×10^{-2} m [*Hocking*, 1985, fig.1].

At very large scales, buoyancy effects become important, and turbulent eddies adopt an elongated appearance, with horizontal scales much larger than their vertical dimensions ('pancake'-like). The scale for determining the transition region between the inertial and buoyancy range is [*Weinstock*, 1978; *Hocking*, 1985]

$$L_B = \left(\frac{2\,\pi}{0.62}\right)\varepsilon^{1/2}\,\omega_B^{-3/2}\ ; \tag{1.7}$$

where ε is the turbulent energy dissipation rate and ω_B is the Brunt-Vaisala frequency of the atmosphere at the height of the turbulence (about 1 oscillation every 8 minutes). Notice that $L_0 = 0.035\,L_B$ [*Hocking*, 1985, equation 44]. In the troposphere, L_B is roughly between 80 m and 3000 m [*Hocking*, 1985, Figure 1].

The inertial range of turbulence only applies strictly for scales somewhat less than L_B and larger than the inner scale l_0. For approximated values of L_B and l_0 see *Hocking* [1985, page 1410].

The appearance of a height continuum of echoes observed with VHF radars may be a result of their capability to detect layers of weaker ε for which $\lambda_{VHF} > \lambda_{transition}$ (where $\lambda_{transition} \equiv 2\,l_0$), so that irregularities of n are still within the inertial subrange. However, if radar does not have adequate resolution, the intermittent turbulence occurring in various layers could appear continuous in height. High-resolution VHF observations by *Rottger and Schmidt* [1979] clearly show the layered structure of reflectivity η.

1.2.2.2.2. Fresnel reflection

The aspect sensitivity and persistence of radar echoes observed by vertically pointing VHF radars cannot be explained by the theory of isotropic-turbulence scatter. In fact, these echoes are often related to partial reflections from steep vertical gradients of the refractive index (discontinuities). The radar equation has to be extended to cover this condition.

Fresnel reflection is observed if a single, dominating discontinuity of the refractive index with a large horizontal extent exists in the vertical direction. A distinct aspect sensitivity should be observed. High-resolution, vertical power profiles should reveal prominent spikes, and height-time intensity plots should show thin and persistent structures. The temporal variations should indicate long coherence times. The process is also called partial reflection, because only a small fraction of the incident power is reflected. Fresnel reflection is also called specular reflection by some authors if the height of the horizontal surface of the discontinuity is assumed to vary slowly as a function of horizontal distance, and diffuse reflection if the discontinuity is assumed to be corrugated or somewhat rough.

In this case, the power received from a single refractivity discontinuity is [*Friend*, 1949; *Rottger and Larsen*, 1990]

$$P_r = \frac{e^2\, P_{Tx}\, A_e^{\,2}}{4\,\lambda^2\, r^2} |\varsigma|^2 \; ; \tag{1.8}$$

where ς is the amplitude reflection coefficient of the refractive-index discontinuity, which is a function of the radar wavelength and the vertical refractive index gradient. As we would expect, the power received from Fresnel reflection is a maximum when the radar antenna beam is normal to the length extension of the discontinuity.

1.2.2.2.3. Fresnel scatter

Instead of a single discontinuity, there can be several (or many) refractive index discontinuities along the pointing direction of the radar beam in the range resolution cell. Then Fresnel scatter occurs. In this case, the radar reflectivity is given by [*Hocking and Rottger*, 1983]

$$\eta = \left(F_r <M>\right)^2 \left[\frac{\gamma_M(\Delta r)}{\Delta r}\right]\left(\frac{2\,\pi\,A_e}{\lambda^2}\right)\ ; \tag{1.9}$$

where F_r is a calibration constant (which must be determined empirically for each radar), dependent on the radar wavelength and on altitude, $<M>$ is the mean gradient of potential refractive index (potential here refers to conditions where potential temperature and specific humidity are constant with height), and $M \equiv \frac{dn}{dz}$. The value of $\gamma_M(\Delta r)$ depends on the form of $<M>$ as a function of height, such that $\gamma_M(\Delta r) = \Delta r$ if $<M>$ is constant with height. The quantity $\left(F_r <M>\right)^2$ is called the generalized reflection coefficient.

An alternative interpretation of Fresnel scatter at vertical incidence is quasi-specular reflection. Horizontally oriented facets of waves on a number of layers are assumed to exist within the pulse volume, and the reflections from all the facets then add incoherently.

The stratification in the atmosphere generally causes the refractive index discontinuities to be randomly distributed along an axis close to the vertical direction, having a large correlation distance in the horizontal direction. Because the refractive-index discontinuities are statistically independent, the temporal echo characteristics are similar to those of turbulence scatter, but the average power profile varies smoothly with altitude.

The terms Fresnel scatter and Fresnel reflection have been introduced because the horizontal correlation distance of the discontinuities is longer than the radar wavelength but of the order of the Fresnel zone, $(r\,\lambda)^{1/2}$. The definition of Fresnel scatter and Fresnel reflection depends, in some sense, on the radar range resolution. Fresnel scatter is more likely to be observed with coarse height resolution, and Fresnel reflection is more likely to be observed with good height resolution. The discontinuities must be of the order of a radar wavelength or less in the vertical direction but of broad extent in the horizontal direction, which, because of diffusion, should be more likely to happen at larger vertical scales. Thus, radars using smaller wavelengths (e.g. UHF band) in clear air probably detect only turbulence scatter, whereas VHF radars will usually detect a combination of the different processes, particularly when using a vertical beam.

1.2.2.3. Real atmosphere

The previous discussion on simplified scattering models lead us toward some operational considerations: 1) Non-volume filling scatter and reflection from several layers have an influence on the accuracy of velocity determinations, since the effective beam angle is changed due to anisotropic scatter and reflection (see section 2.2.2.1). 2) If off-vertical beams are used, antenna sidelobes close to the zenith direction have to be sufficiently suppressed to reduce unwanted signals from reflected components. Otherwise signal power and velocity estimates will be inaccurate. 3) The echoes due to Fresnel scatter and Fresnel reflection are frequently much stronger than the echoes due to turbulence scatter, enhancing the radar sensitivity and allowing VHF radars to detect echoes from higher altitudes with a vertical beam than with off-vertical beams.

Discrimination between Fresnel reflection, Fresnel scatter, and anisotropic and isotropic turbulence scatter is possible for observed echoes using a near-vertical beam at VHF wavelengths. *Hocking and Hamza* [1997] develop a discrimination method based on the aspect sensitivity factor, defined as [e.g., *Mardoc*, 2002, p.23]

$$\theta_S = \sin^{-1}\left(\sqrt{\frac{\sin^2\theta_t}{\ln\left(\frac{P_r(0)}{P_r(\theta_t)}\right)} - \sin^2(\theta_0)}\right);$$

where $P_r(0)$ is the power received by the radar from the vertical direction, $P_r(\theta_t)$ is the power received by the radar in the tilted direction θ_t, and θ_0 is the one-way half-power half-beamwidth of the antenna pattern. According to this method, θ_S should be greater than 5° in all cases of turbulent scatter. Smaller values (θ_S approaching to zero) are indicative of Fresnel reflection. Using the operational θ_S observations from the McGill VHF radar in the summer months, over Montreal, we observe turbulence scattering conditions to persist over the lower troposphere (up to 4 km height) and Fresnel reflection conditions to persist around the tropopause (near 10 km height).

Partially reflecting layers evolve with time and possess varying degrees of spatial (transverse) coherence. They generally will be tilted by internal wave motions causing the quasi-specular echoes to fade. Furthermore, the echoing medium appears different when probed by radio waves possessing different wavelengths. As a result of these and many other complications a statistical approach is often needed to account for the echoes observed by VHF radars.

1.2.3. Scattering from precipitation

Raindrops, snowflakes, and hail are examples of an important class of radar targets known as distributed precipitation targets. In all these cases, the scatter elements are precipitation particles with dimensions much smaller than the radar wavelength. Thus, Rayleigh scatter occurs and the radar cross section is inversely proportional to the fourth power of the wavelength. The instantaneous returned power from precipitation scatterers is then given by the weather radar equation [e.g., *Probert-Jones*, 1962, eqn.3]

$$P_r = \frac{P_{Tx}\,\lambda^2\,L\,G^2\,\theta_0^{\,2}}{256\pi^2\,(\ln 2)}\left(\frac{\eta}{r^2}\right); \tag{1.10}$$

where P_r (in units of watts) is the average returned power, P_{Tx} (in watts) is the transmitted power, λ (in meters) is the radar wavelength, L (in meters) is the pulse length, G is the antenna gain, θ_0 is the 3-dB beamwidths, and r (in meters) is the range. The radar reflectivity per unit volume, η (in m^{-1}), is given by [e.g. *Rinehart*, 1997, eqn. 5.13]

$$\eta = \frac{\pi^5 \left|\mathrm{K}\right|^2 \sum_{vol} D_e^{\,6}}{\lambda^4} \; ; \tag{1.11}$$

where D_e is the equivalent-spherical diameter of the precipitation particle, and the quantity $\sum_{vol} D_e^{\,6} \equiv Z$ is defined as the radar reflectivity factor. For equation (1.11), $\sum_{vol} D_e^{\,6}$ is expressed in m^3, but Z is usually given in $mm^6 \; m^{-3}$. Note also that the quantity $dBZ \equiv 10 \log_{10} Z$. Then,

$$\eta = \frac{\pi^5 \left|\mathrm{K}\right|^2}{\lambda^4} 10^{\frac{(dBZ-180)}{10}} = \frac{\pi^5 \left|\mathrm{K}\right|^2 Z}{\lambda^4 \, 10^{18}} \; . \tag{1.12}$$

$|\mathrm{K}|$ is the magnitude of a parameter related to the complex index of refraction. The value of $|\mathrm{K}|^2$ depends upon the material composition, the temperature, and the radar wavelength. Unfortunately, the exact values for $|\mathrm{K}|^2$ in the VHF band are still unknown. Generally, the typical values at S-band, $|\mathrm{K}|^2 \approx 0.93$ for water, and $|\mathrm{K}|^2 \approx 0.21$ for ice, are used [e.g., *Chilson et al.*, 1993].

Equation (1.10), expresses P_r in terms of constants, radar parameters, and scatter parameters. However, this equation is only valid for targets that can be approximated as spherical particles having a diameter size that is small when compared to the radar wavelength (a condition for the Rayleigh approximation) and for electromagnetic waves that are attenuated by precipitation. Both conditions are generally valid for VHF wavelengths, while these conditions are not always fulfilled for shorter wavelengths (e.g. measurement of large particles such as hail using weather radars operating at X, C, or S band).

1.2.4. Comparison of precipitation vs. clear air

The VHF band is optimal for obtaining independent, simultaneous signal from precipitation and clear air. This is put in context by *Chilson et al.* [1993], here in Figure 1.2, where the reflectivities for turbulent and for precipitation scatterers are shown as a function of the radar wavelength. The plotted values correspond to Z between 30 and 50 dBZ and are typical of those observed in moderate and heavy rainfall, respectively. The values of C_n^2 equal to 10^{-15} $m^{-2/3}$ and 10^{-13} $m^{-2/3}$ are likewise representative of what one might find in moderate and severe turbulence similar to that expected in a thunderstorm. It is clear that the returned VHF (6 m) signal should exhibit some contribution from both precipitation as well as turbulence, whereas at smaller wavelengths (e.g. at UHF, 70 cm) the signal will be dominated only by precipitation.

Unfortunately, ranges for Z and C_n^2 in Figure 1.2 are still very wide. As well, these estimates assume that $|K|^2$ is the same at S, UHF, and VHF bands. Notice also that the C_n^2 values in Figure 1.2 are simply approximate estimations [*Chilson et al.*, 1993, p.665], which still have to be corroborated for particular locations, although some C_n^2 estimates can be inferred from more recent measurements of turbulence within clouds and precipitation [i.e., *White et al.*, 1996; *Knight and Miller*, 1998; and *Meischner et al.*, 2001].

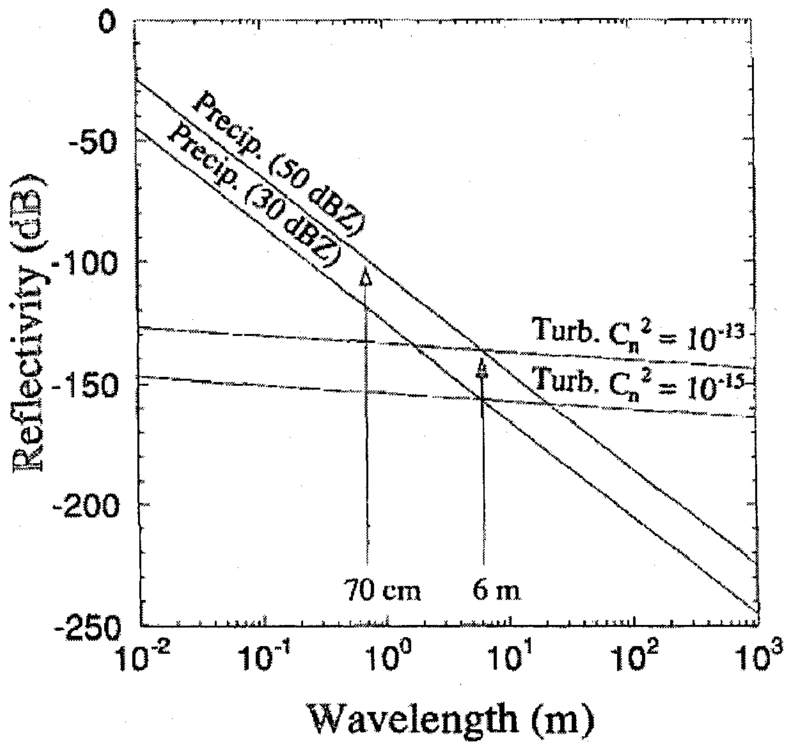

Figure 1.2. C_n^2 and Z as a function of the radar wavelength. By plotting the values of reflectivity η as a function of radar wavelength λ, for precipitation and clear-air turbulence, the values of C_n^2 and Z are compared. The values presented (for C_n^2 and Z) are typical of those found in a thunderstorm environment. Note that at VHF band (wavelengths near 6 m) $\eta(Z) \approx \eta(C_n^{\,2})$, which indicates that the radar is more or less equally sensitive to precipitation and to clear-air turbulence. At UHF band (wavelengths near 70 cm) the radar is much more sensitive to precipitation than to clear air. [From *Chilson et al.*, 1993.]

1.2.5. Emissions at VHF band

In addition to the backscattered signal, a VHF radar will also receive electromagnetic radiation that has been emitted by other sources. When these VHF emissions correspond with a very broad spectrum of Doppler frequency shifts, then they are called white noise. In general, noise in VHF radars has a large contribution from environmental, cosmic, and atmospheric sources, and it is not easily quantified. Therefore, antenna design and the specific radar location and frequency band of operation define the system noise. The main sources of white noise in VHF band (applied to the study of the atmosphere) are Cosmic VHF emissions. These cosmic emissions vary with time and space.

In addition, every lightning discharge emits a broadband radio signal called 'sferics'. Although the peak in electromagnetic frequency of a sferic is around 10 kHz (in the very low frequency, VLF, band), the emission is still very strong at the VHF band. Thus, every time there is a lightning discharge in the vicinity of the radar, the noise floor rises dramatically at all range gates. Furthermore, because of its high reflectivity at VHF, lightning echoes can enter through the antenna sidelobes.

Emissions of broadcast telecommunication systems that operate into the VHF range are also a contaminant. These emissions are called interference. They also raise the noise floor significantly at all range gates, but their duration is much longer than in the case of lightning (broadcast transmissions can last a few seconds or minutes, while lightning emissions only last a few milliseconds).

1.3. Objectives

This research focuses on the following questions: How can we use VHF radar as an operational tool for the study of precipitation physics? What are the typical backscatter signals that rain and turbulence produce at VHF band during precipitation events? The key to answer these questions lays in the unique potential that VHF radars have for simultaneously measuring air vertical velocity and precipitation intensity.

There are four basic requirements in order to typify precipitation and turbulence signals at VHF. First, we require a detailed review to the radar calibration process. Second, we need to develop a signal-processing algorithm that allows the automatic separation of precipitation and clear-air signals. Third, we must apply this algorithm in an efficient analysis of large radar datasets taken during rain. Fourth, we must generate statistics of Z and C_n^2 values observed in the Montreal region. Accomplishments of these basic requirements are the four specific objectives of this research.

In all cases, the McGill VHF radar [*Campos and Hocking*, 2003] is used as the main analysis tool. Additionally, other remote sensors are used, such as an X-band vertically-pointing radar, as well as ground measurements of raindrop-size distributions. (Details about these instruments are given in the forthcoming chapters.)

The following four chapters achieve the scientific objectives of the thesis, and the final chapter discusses the main findings and provides some suggestions for future research.

CHAPTER 2:

A MULTI-FACETED APPROACH TO CALIBRATE VHF RADAR ANTENNA AND RECEIVER

ABSTRACT

Many quantitative analyses of radar signal require a radar calibration. Established calibration methods for VHF radar provide only partial information about antenna or receiver parameters. We propose that a more complete approach to calibrate VHF radar can be obtained by combining multiple calibration methods. To test this, we developed a calibration technique by combining a first calibration method that compares the recorded VHF signal to power coming from a noise generator and a second calibration method that compares recorded VHF signal to cosmic radiation. We derive four equations that allow us to retrieve antenna and receiver parameters (such as noises, efficiency, and gain), and four other equations for the corresponding errors. In addition, we develop an equation for calibrating Doppler spectra. To test our calibration technique, we collected an extensive dataset from the McGill VHF radar. For validation, we performed a third calibration using measurements of voltage and impedance to compute power losses in the antenna transmission lines. Based on our equations, we have found the values for the antenna and receiver parameters in the McGill VHF radar, and their corresponding uncertainties, and we have compared these to the energy losses obtained by the third calibration method. The antenna efficiencies derived by our technique and by the third calibration method agreed within 0.5 dB. Furthermore, analyses of our calibrated Doppler spectra in rain demonstrate the potential of this calibration technique for absolute measurement of precipitation by wind-profiler radar.

2.1. Introduction

Numerous meteorological applications have been made possible through VHF radar techniques [see for example the reviews by *Rottger and Larsen*, 1990; *Gage*, 1990; and *Gage and Gossard*, 2003]. Measurements of absolute backscatter power by VHF (Very High Frequency) radars are one important aspect of atmospheric studies of clear-air turbulence [e.g., *Hocking*, 1985] and precipitation [e.g., *Wakasugi et al.*, 1986]. There is, however, a central issue that must be dealt with before attempting any quantitative study of precipitating weather systems with VHF radars: the radar calibration.

In a typical setting for VHF radars (Figure 2.1), a pulse of known power P_{Tx} is sent from the transmitter hardware towards the antennas. Actual antennas also have power losses, in particular due to impedance mismatches and thermal-energy dissipation in the antenna structure and cables. Therefore, the power radiated to space P_t is actually smaller than the power available at the antenna input P_{Tx}. The ratio of these quantities is the antenna transmission efficiency (or radiation loss factor, $e_T = P_t / P_{Tx}$). Further power losses are also experienced during the antenna reception, i.e., between the point at which the backscattered power is input into the antenna (P_r) and the point at which the power is output from the antenna towards the receiver hardware (P_{Rx}). The reception efficiency is then given by $e_R = P_{Rx} / P_r$. In addition, the transmitter can leak small amounts of power into the receiver, cables, and antenna structure, generating electromagnetic noise at the radar VHF frequency. These leaked powers (expressed here as antenna noise N_a

and Receiver Noise N_{Rx}) can be particularly significant during the radar reception period. We then can write:

$$P_{Rx} = P_r \, e_R + N_a \, . \tag{2.1}$$

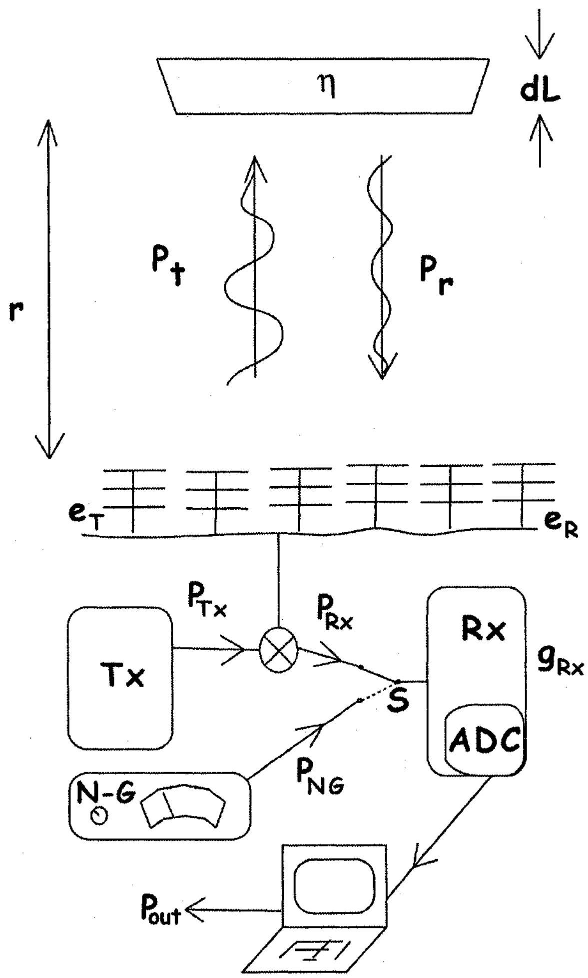

Figure 2.1. Simplified schematic diagram of a typical VHF radar. *Tx* is the transmitter, *Rx* the receiver, and *ADC* the analog-to-digital converter. Others symbols are referred to in the text. The *N-G* corresponds to a Noise-Generator hardware, which can be switched in at point *S* (as input for the receiver in order to perform a calibration).

Of further relevance, however, is the fact that the power output after signal processing (P_{out}) has been usually converted, by an analog-to-digital-converter (ADC), into numbers with arbitrary units (au). In the linear region of a receiver with linear amplifiers, the conversion from W to au is mathematically expressed by the receiver gain, g_{Rx}, such that

$$P_{out} = P_{Rx}\ g_{Rx} + N_{Rx}\ . \tag{2.2}$$

Notice that g_{Rx} is not an efficiency, because efficiency denotes some loss (of power). Variable g_{Rx} combines two factors: amplification in the receiver and the conversion factor from Watts into arbitrary units (made by the ADC).

Measurement or retrieval of several meteorological variables (such as turbulence and precipitation intensity) requires that P_{out} must be given in Watts (W) instead of arbitrary units (au). A calibration procedure is thus required. The standard calibration procedure involves a noise-generator hardware that is connected directly to the receiver. However, this calibration does not take into account the antenna parameters (antenna noise and efficiencies), nor transmitter characteristics (P_{Tx}).

On the other hand, using known sources of cosmic radiation is a common method for calibrating radio telescopes [e.g., *Léna et al.*, 1998, section 3.5]. We can also apply this method to calibrate VHF radars, given the fact that at VHF band the power from cosmic sources is large, and that this cosmic power can in principle be computed from the Rayleigh-Jeans approximation to the Plank's Law [e.g., *Ulaby et al.*, 1981, section 4-3.3]. Unfortunately, attempts at VHF radar-calibration using cosmic radiation have been reported in the literature only a few times [e.g., *Hocking et al.*, 1983; *Green et al.*, 1983; *Campistron et al.*, 2001]. A calibration from known sources of cosmic radiation is more complex than the calibration from a noise generator. There is also the inconvenience that, when computing the receiver power from the radar equation, we need to know the antenna parameters (e.g., N_a and e_R) independently from the receiver parameters (e.g., N_{Rx} and g_{Rx}); and this cannot be calculated from cosmic-noise calibrations only.

In this chapter, we overcome these radar calibration difficulties by both improving the model for cosmic radio sources and also by combining this method with the known noise-generator method. We present here our new VHF calibration approach that provides estimates of both the antenna parameters and the receiver parameters. We also perform an independent check through a third calibration method, which uses measurements of voltage and impedance to compute power losses at different points along the antenna transmission lines.

2.2. Methods

Any radar power calibration involves a comparison between a known power source and the radar power measurement. In the first part of our calibration technique, the known power source corresponds to the input (in Watts) from a noise-generator. In the second part, the known power source is the cosmic radio emissions (in Watts). We then combine both calibrations results to retrieve particular antenna and receiver parameters. We will now explain each part in more detail.

2.2.1. Noise-generator calibration

For the first part of the calibration, the noise-generator calibration, the radar hardware was configured as in Figure 2.1. In this case, the power P_{NG} from the noise-generator hardware (*N-G*) was input into the receiver hardware *Rx*. This power was digitized by the Analog-to-Digital Converter (*ADC*) and then sent to a computer, where the signal processing took place. This gave as a result the output power P_{out} (in arbitrary units, au). The objective here was to obtain a linear relation between the power input by the noise-generator (P_{NG}, in Watts) and the radar power output after all signal processing (P_{out}, in au); i.e.,

$$P_{NG} = P_{out} B_{NG} + A_{NG} \; ; \tag{2.3}$$

where A_{NG} is the power (noise) generated within the receiver hardware, measured in Watts. B_{NG} corresponds to the conversion factor between the input and output powers, measured in W/au. It should be noted that this calibration cannot be used to obtain any antenna parameters (e.g., efficiency and noise).

2.2.2. Sky-noise calibration

Figure 2.2 illustrates the second part of our method, the sky-noise calibration. This figure presents a radar hardware configuration where the power received by the antennas comes exclusively from cosmic sources. Under these conditions, a linear relation can be obtained between the VHF cosmic radio emissions (sky power: $P_{sky} = P_r$, in Watts) and the radar output power (P_{out}, in au); i.e.,

$$P_{sky} = P_{out} B_{sky} + A_{sky} \; ; \tag{2.4}$$

where A_{sky} corresponds to the power (noise) generated within the radar hardware, measured in Watts, and B_{sky} (measured in W/au) is the conversion factor between the power received by the antennas and the power output after the signal processing.

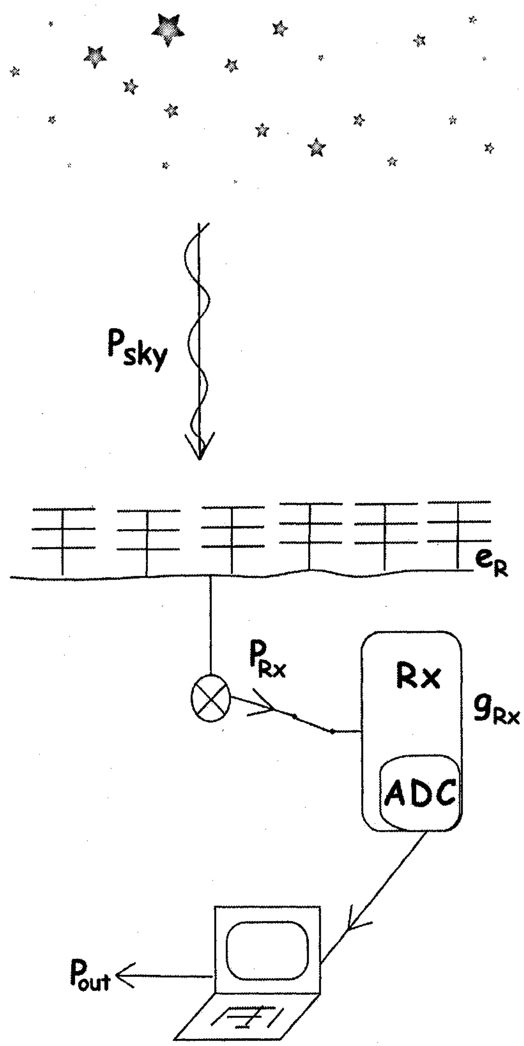

Figure 2.2. Hardware configuration during sky-noise calibration.

The values of P_{sky} were obtained from sky surveys of cosmic radio emissions at VHF [e.g., *Campistron et al.*, 2001; *Milogradov-Turin and Smith*, 1973; *Roger et al.*, 1999]. These sky surveys are usually given as brightness temperatures (T_1) valid for a given electromagnetic frequency (f_1). This survey frequency is hardly ever equal to the electromagnetic operation frequency of our radar (f_2). Therefore, we had to correct these brightness temperatures before applying them in our calibration. The sky brightness temperature corresponding to our radar frequency (T_2) is then given by [e.g., *Roger et al.*, 1999, page 14; or *Campistron et al.*, 2001, equation 3]

$$T_2 = T_1 \left(\frac{f_2}{f_1} \right)^{-\beta} \quad ; \qquad (2.5)$$

where the brightness temperatures are both given in Kelvins, and β is the so-called spectral index. Although β varies according to the position in the sky as well as the ratio f_2/f_1 [e.g., *Roger et al.*, 1999, present a sky survey for f_1 = 22 MHz and f_2 = 408 MHz, with β in the range 2.40 to 2.55, and its average is 2.5], it is generally assumed that $\beta \approx 2.5$. This assumption leads to a relative error smaller than 3% in the retrieved temperature at VHF band [*Campistron et al.*, 2001].

Then, the cosmic power (in Watts) at 52 MHz is given by [e.g., *Ulaby et al.*, 1981, section 4.4]

$$P_{sky} = k_{Boltzmann} \; T_2 \; BPF_{width} \quad ; \qquad (2.6)$$

where $k_{Boltzmann}$ = 1.381x10^{-23} J/K is the Boltzmann constant [e.g., *Mohr and Taylor*, 2003; recall also that J/K = W / (Hz K)], and BPF_{width} is the band-pass filter width of the radar receiver, in Hertz. The derivation of equation (2.6) takes into account the facts that the cosmic radiation is unpolarized, and that our linearly-polarized antenna will then collect half of the incident (unpolarized) cosmic power [*Ulaby et al.*, 1981].

This sky-noise calibration only provided information about the antenna and receiver parameters in a general sense. Particular values such as antenna efficiency or receiver noise could not be retrieved in this manner. However, we were able to retrieve these antenna and receiver parameters by combining both the sky-noise calibration and noise-generator calibration methods. The next section explains the procedure.

2.2.3. Combining both calibration methods

Particular expressions for antenna and receiver parameters were derived by combining equations (2.1), (2.2), (2.3), and (2.4). Starting from equations (2.2) and (2.3), with $P_{Rx} = P_{NG}$:

$$\frac{-N_{Rx}}{g_{Rx}} + \frac{P_{out}}{g_{Rx}} = A_{NG} + B_{NG}\, P_{out} \Rightarrow$$

$$g_{Rx} = \frac{1}{B_{NG}} \tag{2.7}$$

and

$$N_{Rx} = -A_{NG}\, g_{Rx} = \frac{-A_{NG}}{B_{NG}} \; . \tag{2.8}$$

As well, from equations (2.1) and (2.2):

$$P_r\, e_R\, g_{Rx} + N_a\, g_{Rx} + N_{Rx} = P_{out} \quad \Rightarrow$$

$$P_r = \frac{-(N_a\, g_{Rx} + N_{Rx})}{e_R\, g_{Rx}} + \frac{1}{e_R\, g_{Rx}} P_{out} \; . \tag{2.9}$$

From equations (2.4) and (2.9), with $P_r = P_{sky}$:

$$B_{sky} = \frac{1}{e_R\, g_{Rx}} \; .$$

Then, from equation (2.7):

$$e_R = \frac{B_{NG}}{B_{sky}} \ . \tag{2.10}$$

Also from equations (2.4) and (2.9):

$$A_{sky} = \frac{-\left(N_a \, g_{Rx} + N_{Rx}\right)}{e_R \, g_{Rx}} \quad \Rightarrow \quad N_a = -A_{sky} \, e_R + \frac{N_{Rx}}{g_{Rx}} \ .$$

Then from equations (2.7), (2.8), and (2.10):

$$N_a = -A_{sky} \frac{B_{NG}}{B_{sky}} - A_{NG} \ . \tag{2.11}$$

In addition, expressions for the uncertainties in the antenna and receiver estimates (e_R, N_a, g_{Rx}, and N_{Rx}) were derived from the following expression [e.g., *Press et al.*, 1986, page 505]:

$$\sigma^2(f) = \sum_{i=1}^{n} \sigma^2(x_i) \left(\frac{\partial f}{\partial x_i} \right)^2 \ ; \tag{2.12}$$

where $\sigma^2(f)$ is the variance uncertainty of the function f, which is a function that depends on variables x_1 , x_2 ,..., x_{n-1} , x_n . As well, $\sigma^2(x_i)$ is the variance uncertainty for the i-th variable. Equation (2.12) was then applied to equations (2.7), (2.8), (2.10), and (2.11) in order to obtain the following one-standard-deviation uncertainties:

$$\sigma(g_{Rx}) = \frac{\sigma(B_{NG})}{B_{NG}^2} \ ; \tag{2.13}$$

$$\sigma(N_{Rx}) = \sqrt{\frac{\sigma^2(A_{NG})}{B_{NG}^2} + \sigma^2(B_{NG}) \frac{A_{NG}^2}{B_{NG}^4}} \ ; \tag{2.14}$$

$$\sigma(e_R) = \sqrt{\frac{\sigma^2(B_{NG})}{B_{sky}^2} + \sigma^2(B_{sky}) \frac{B_{NG}^2}{B_{sky}^4}} \ ; \tag{2.15}$$

$$\sigma(N_a)=\sqrt{\sigma^2(A_{sky})\frac{B_{NG}^2}{B_{sky}^2}+\sigma^2(B_{NG})\frac{A_{sky}^2}{B_{sky}^2}+\sigma^2(B_{sky})\frac{A_{sky}^2\ B_{NG}^2}{B_{sky}^4}+\sigma^2(A_{NG})}\ ; \quad (2.16)$$

where the values for $\sigma^2(A_{sky})$, $\sigma^2(B_{sky})$, $\sigma^2(A_{NG})$, and $\sigma^2(B_{NG})$ were obtained from the square of uncertainties in the coefficients of equations (2.3) and (2.4).

Therefore, the antenna and receiver parameters were found from equations (2.7), (2.8), (2.10), and (2.11); and the corresponding uncertainties were computed from equations (2.13), (2.14), (2.15), and (2.16).

2.2.4. Computing calibrated power spectra

Once we have the calibration of the radar measured power (P_{out}), we proceed with a calibration of the power densities. To do this we produce Doppler spectra from a recorded time series and then proceed as follows. We assume that the spectra are recorded at steps Δf. Then, from equation (2.4) we know that

$$\Delta f\ \left[\, S_{sky}(f_1)+S_{sky}(f_2)+\ldots+S_{sky}(f_n)\,\right] = $$
$$A_{sky}+B_{sky}\ \Delta f\ \left[\, S_{out}(f_1)+S_{out}(f_2)+\ldots+S_{out}(f_n)\,\right]\ ;$$

where Δf is the spectral bin resolution (in Hz). The variables $S_{out}(f_i)$ and $S_{sky}(f_i)$ correspond to the Doppler power densities at the i-th spectral bin (a total of n spectral bins), given in au/Hz for the variables with the subscript *out* and in W/Hz for the variables with the subscript *sky*. The previous equation can also be expressed as

$$\sum_{i=1}^{n} S_{sky}(f_i)=\sum_{i=1}^{n}\left[\frac{1}{n}\frac{A_{sky}}{\Delta f}+B_{sky}\ S_{out}(f_i)\right].$$

Therefore, the power-densities calibration equation for the i-th spectral bin is given by

$$S_{sky}(f_i) = \frac{1}{\mathrm{n}} \frac{A_{sky}}{\Delta f} + B_{sky}\, S_{out}(f_i)\,. \tag{2.17}$$

Note that, for the derivation of equation (2.17), the linear relation in equation (2.4) must be applied for the powers in linear units.

It is not rare to have radar signal processing performing coherent averaging (e.g., in the McGill VHF radar). Under these conditions, the full spectral range is defined by the radar sampling rate as follows:

$$f_{sampling} = \frac{PRF}{N_{coh}}\ ; \tag{2.18}$$

where PRF is the radar pulse repetition frequency and N_{coh} is the number of samples used for the coherent averages (given in Table 2.1).

Table 2.1. McGill VHF Radar parameters

Parameter	Value
Beam direction	vertical
Transmitted wavelength (frequency)	5.77 m (52.0 MHz)
Peak transmitted power	40 kW
One-way half-power half-beamwidth	2.3 degrees
Pulse duration	3.5 µs
Pulse repetition frequency (PRF)	6.0 kHz
Band pass Rx filter width (BPF_{width})	400 kHz
Number of coherent averages (N_{coh})	16
Doppler spectral range (DSR, after signal processing)	20 Hz
Time resolution	Approx. 35 s / profile
Location (Lat., Long.)	45.409° N, 73.937° W

Another common signal processing practice (also performed by the McGill VHF radar) is to store only Doppler power spectra within a range of interesting frequencies [i.e., $S'_{out}(f_i)$]. If the full spectral range [i.e., $S_{out}(f_i)$] corresponds to Doppler frequencies within $\pm$ 0.5 $f_{sampling}$, then the quantity P_{out}, corresponding to the full spectral range, is given by

$$P_{out} = P'_{out} \frac{f_{sampling}}{DSR} = \frac{P'_{out}\ PRF}{DSR\ N_{coh}} \ ; \qquad (2.19)$$

where

$$P_{out} = \sum_{f=-fsampling/2}^{+fsampling/2} S_{out}(f) \ ;$$

$$P'_{out} = \sum_{f=-DSR/2}^{+DSR/2} S'_{out}(f) \ ;$$

and P'_{out} is the total power integrated within the stored Doppler spectral range (DSR).

Equation (2.17) has then to be modified according to equations (2.18) and (2.19). For this, we use the fact that the power density is conserved for a white-noise spectrum. As well, we recognize that the application of coherent averaging (of in-phase and quadrature time series, as it is done in our signal processing) reduces the full spectral range [reduction already included in the definition of $f_{sampling}$; i.e., equation (2.18)] and the measured P_{sky} (since the spectral density magnitude is preserved at all frequency bins; e.g., *Lyons*, 1997, p.321). Therefore, the calibrated power-density spectra, S_{cal}, at the frequency bin f_i, must be such that

$$\frac{\frac{1}{N_{coh}} P_{sky}}{f_{sampling}} = \frac{\sum_{i=1}^{n} [\Delta f\ S_{cal}(f_i)]}{DSR} \ ; \qquad (2.20)$$

where N_{coh} is the number of samples used for the coherent averages, Δf is the spectral bin resolution, and P_{sky} is given in Watts. In addition, equation (2.4) provides us with a conversion between Watts and arbitrary units. Therefore, from equations (2.4), and (2.20) we obtain that

$$\frac{A_{sky} + B_{sky}\, P_{out}}{N_{coh}\, f_{sampling}} = \frac{\Delta f}{DSR} \sum_{i=1}^{n} S_{cal}(f_i)\ . \tag{2.21}$$

However, from Equation (2.19) we know that

$$\frac{P_{out}}{f_{sampling}} = \frac{\sum_{i=1}^{n} \left[\Delta f\ S'_{out}(f_i)\right]}{DSR}\ ; \tag{2.22}$$

where $S'_{out}(f_i)$ is the measured spectral density (in au/Hz) at the Doppler frequency bin f_i. Then, by combining (2.21) and (2.22), we have that

$$\frac{A_{sky}}{N_{coh}\, f_{sampling}} + \frac{B_{sky}}{N_{coh}} \frac{\sum_{i=1}^{n} \left[\Delta f\ S'_{out}(f_i)\right]}{DSR} = \frac{\Delta f}{DSR} \sum_{i=1}^{n} S_{cal}(f_i)\ ; \tag{2.23}$$

$$\Rightarrow \quad \frac{DSR\ A_{sky}}{\Delta f\ N_{coh}\, f_{sampling}} + \frac{B_{sky}}{N_{coh}} \sum_{i=1}^{n} S'_{out}(f_i) = \sum_{i=1}^{n} S_{cal}(f_i)\ ;$$

$$\Rightarrow \quad \sum_{i=1}^{n} \left[\frac{1}{n} \frac{DSR\ A_{sky}}{\Delta f\ N_{coh}\, f_{sampling}}\right] + \sum_{i=1}^{n} \left[\frac{B_{sky}}{N_{coh}} S'_{out}(f_i)\right] = \sum_{i=1}^{n} S_{cal}(f_i)\ .$$

Since $\Delta f = DSR/\mathrm{n}$, we thus get,

$$S_{cal}(f_i) = \left[\frac{A_{sky}}{f_{sampling}} + B_{sky}\ S'_{out}(f_i)\right] \frac{1}{N_{coh}}\ . \tag{2.24}$$

2.2.5. Operational background

To show the application of our method we used data from the McGill VHF radar [described by *Campos and Hocking*, 2003] working under the configuration described in Table 2.1. The signal processing used here was the same as in

Hocking [1997, section 4]. Every 35 seconds, a profile of 45 Doppler power spectra (300-point discrete-spectrum within a spectral range of ± 10.0 Hz, for 45 range gates between 0.5 and 23.0 km) was produced. We integrated each of these spectra in order to obtain corresponding P'_{out} values; i.e., the integrated powers (in au) within the Doppler spectral range (*DSR*, see Table 2.1).

As described in section 2.2.1, during the noise-generator calibration, a small modification was made in the reception hardware. The noise-generator output was connected to the receiver, instead of the line from the transmitter-receiver switch. Then, different noise sources were obtained by changing the factor F_{NG} in the noise-generator hardware. One unit increment in F_{NG} was equivalent to a 290 Kelvins increase in brightness temperature. At $F_{NG} = 0$, the noise generator still introduces a small amount of power into the receiver. This amount depends on the noise generator temperature (approximately 290 K) in a manner similar to equation (2.6). Therefore, power input by the noise generator into the radar receiver was given by:

$$P_{NG} = (F_{NG} + 1)(290K)\, k_{Boltzmann}\, BPF_{width} \; ; \qquad (2.25)$$

where P_{NG} is the noise-generator power (in Watts, measured in the radar receiver just after the band-pass filter). As before, $k_{Boltzmann}$ is the Boltzmann constant and BPF_{width} is the band-pass filter width of the radar receiver (given in Table 2.1), in Hertz.

For the second part of our calibration, there was no need to disconnect the transmitter, or to alter the normal operation of the radar in any way. We kept the radar hardware and software working as usual (i.e., Figure 2.1 with line from transmitter-receiver switch connected to receiver). The known power sources from cosmic radio emissions (in Watts) were then compared with the corresponding radar integrated power (in au) measured only at very high range gates (between 17.5 and 22.5 km). At these ranges, backscattering of the transmitted power and other terrestrial VHF radio sources is negligible. Thus, the radar received powers—at these high ranges only—were considered as coming exclusively from cosmic sources.

2.3. Results

2.3.1. Noise-generator calibration

The noise-generator calibration was performed using observations made on 21 October 2004, a day without precipitation. The results are presented in Figure 2.3. For a given P_{NG} value, there are 45 P'_{out} values plotted in the X-axis. These P'_{out} values correspond to the 45 radar range gates (between 0.5 and 23.0 km) available at each profile. We then computed the P_{out} values plotted in the abscissa (X-axis) of Figure 2.3 by using equation (2.19). The range of F values, from 0 to 30 units, was sampled twice (the two datasets are represented in Figure 2.3 as small crosses). A Chi-square linear fit [*Press et al.*, 1986, section 14.2] was then used to obtain the relation

$$P_{NG} = \left(-3.420\times10^{-15} \pm 6.7\times10^{-17}\right)[W] + P_{out}\left(9.250\times10^{-21} \pm 2.3\times10^{-23}\right)[W/au] \; ; \qquad (2.26)$$

where the units are given in square brackets, and the uncertainties correspond to one standard-deviation errors in the coefficients estimates. The relationship (2.26) is presented as a line in Figure 2.3.

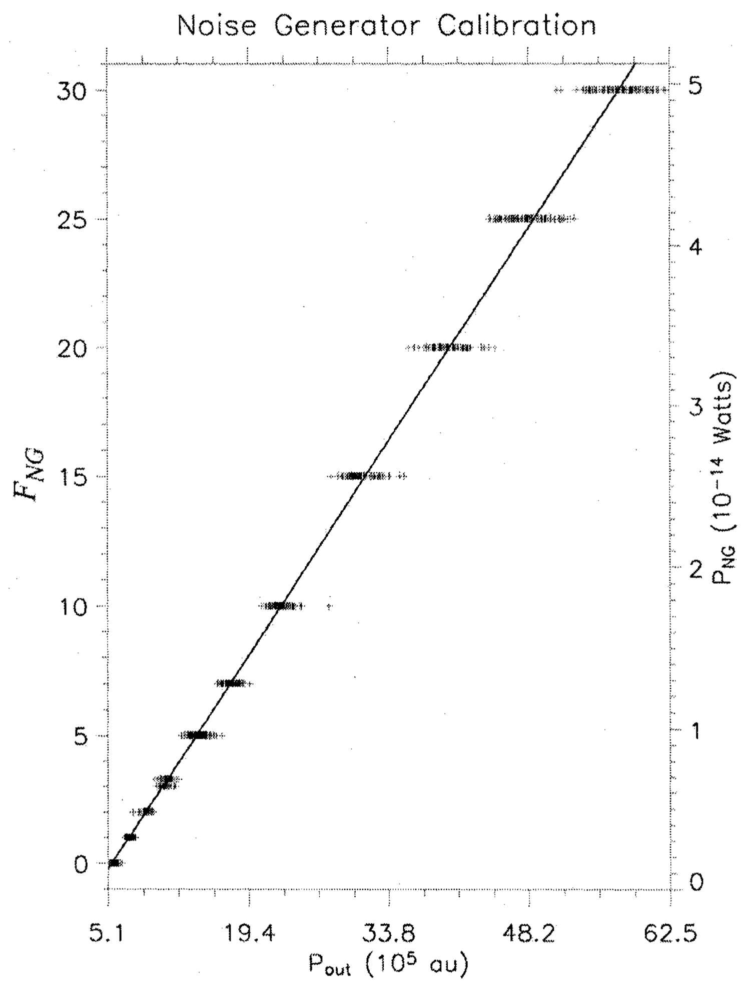

Figure 2.3. Result of the noise-generator calibration. The left-side Y-axis is the noise-generator factor F_{NG}, which is related to the right-side Y-axis, the power P_{NG} , by equation (2.25). For every P_{NG} value, there are 45 P_{out} values (corresponding to 45 radar range gates), which are computed from equation (2.19) and plotted in the X-axis. The linear relation in equation (2.26) is given by the line, and it is obtained from two calibration experiments (990 observations in total).

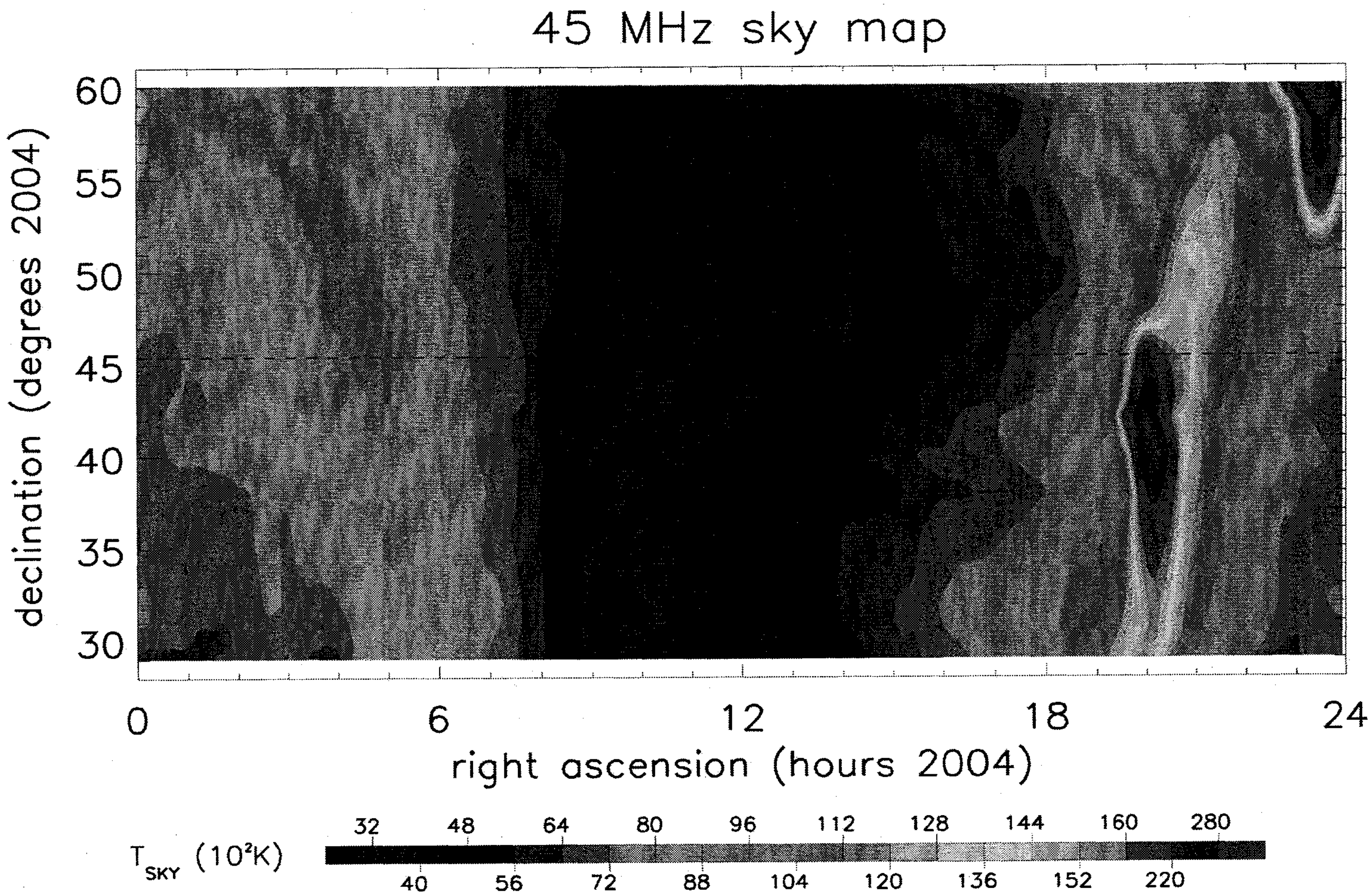

Figure 2.4. Epoch-corrected sky survey at 45 MHz.

2.3.2. Cosmic-Noise calibration

2.3.2.1. Sky map

The cosmic noise power P_{sky} at the radar operating frequency (52 MHz) was obtained from a sky brightness temperatures map at 45 MHz (the closest available frequency). We used data published by *Campistron et al.* [2001], which corresponds to epoch-J1999 equatorial-coordinates. These coordinates, right ascension and declination, are continuously changing in time, primarily as a result of the precession of the equinoxes. We then had to convert the figure coordinates from the epoch J1999 to the epoch J2004 (the epoch of the radar observations). For this, we used the standard procedure given in section B42 of The Astronomical Almanac [*Nautical Almanac Offices*, 2003]. The resulting sky map is presented in Figure 2.4, which has a resolution of 1.5 minutes in right-ascension hour and 1 degree in declination angle.

To test the reliability of this 45 MHz map, we compared its brightness temperatures at a particular declination angle (matching our VHF radar observations) with the corresponding values from the maps by *Milogradov-Turin and Smith* [1973] and by *Roger et al.* [1999]. The first map corresponds to a 38 MHz frequency and epoch J1967, and the second map corresponds to 22 MHz frequency and epoch B1950. For this comparison, we then had to convert the 45, 38, and 22 MHz temperatures to 52 MHz by using equation (2.5) with β=2.5. As well, we had to precess the coordinates to a common astronomical epoch, in this case J2004 (the epoch of our VHF radar observations). Finally, we use linear interpolation in order to obtain the temperature value at the declination of 45.409°

and with a right ascension resolution of 0.25 hours. Figure 2.5 presents the comparison of sky brightness temperatures for the three maps. The only significant disagreement is with the 22 MHz map, at right ascension between 19 and 22 hours, probably due to contamination by the strong signal from Cygnus A. However, there is general agreement between the three sky maps, which indicates the reliability of the 45 MHz map.

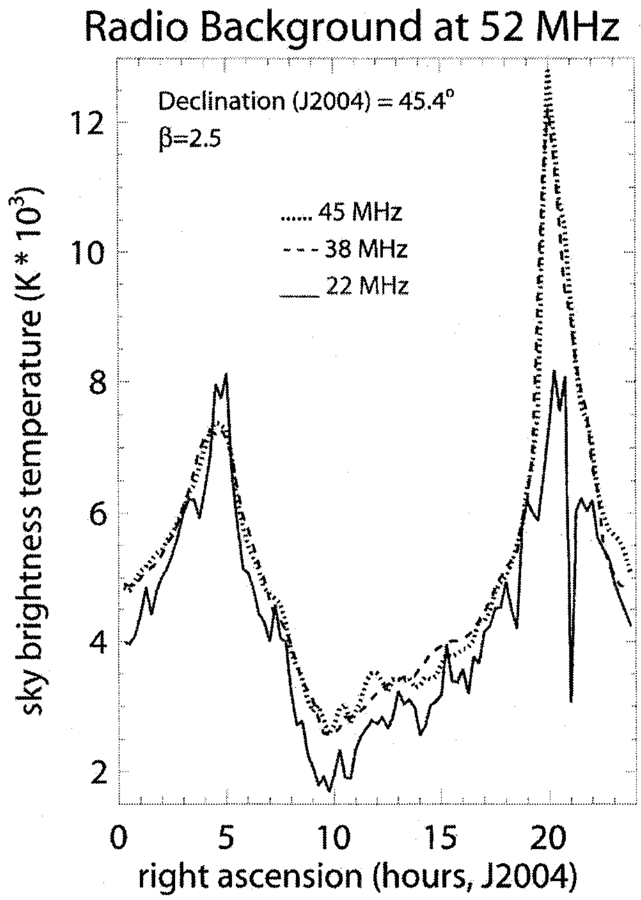

Figure 2.5. Comparison of 52 MHz sky brightness temperatures at 45.409° declination. It is obtained by applying equation (2.5), with β=2.5, to the data in sky surveys at 45 MHz (in dotted line), 38 MHz (in dashed line), and 22 MHz (in continuous line).

Considering our radar antenna pattern and time resolution, the radar observations and the sky map did not match in resolution (the datasets representativeness are not the same). Therefore, the sky brightness temperatures—at the radar declination—were smoothed in order to resemble our VHF radar resolution. We did this by convolving the 45 MHz map (Figure 2.4) with a direct numerical simulation of the one-way antenna pattern (i.e., the antenna one-way polar-diagram). This antenna pattern was provided by the radar manufacturer (Mardoc Inc., of London, Ontario, Canada) and it is presented in Figure 2.6. Notice that, as the kernel of the convolution operation, we used only a section of the full antenna pattern (zenith angles smaller than 13°, having the same resolution as the sky map, i.e., 1.5 minutes per 1 degree). Zenith angles greater than 13° were not used since they imply a kernel outside the sky map. In any case, the sidelobes of the antenna pattern located outside 12° zenith angles are not significant (their magnitudes are generally smaller than -15 dB). For all right ascension hours (at a resolution of 1.5 minutes), the convolution was performed with the kernel centered at the declination of our radar observations (i.e., 45.409° declination angle, at the dashed line in Figure 2.4). The result for this convolution, between the sky brightness temperatures and the antenna pattern, was used as input for equation (2.5). The resulting 52-MHz brightness-temperatures are plotted in Figure 2.8 as the red line.

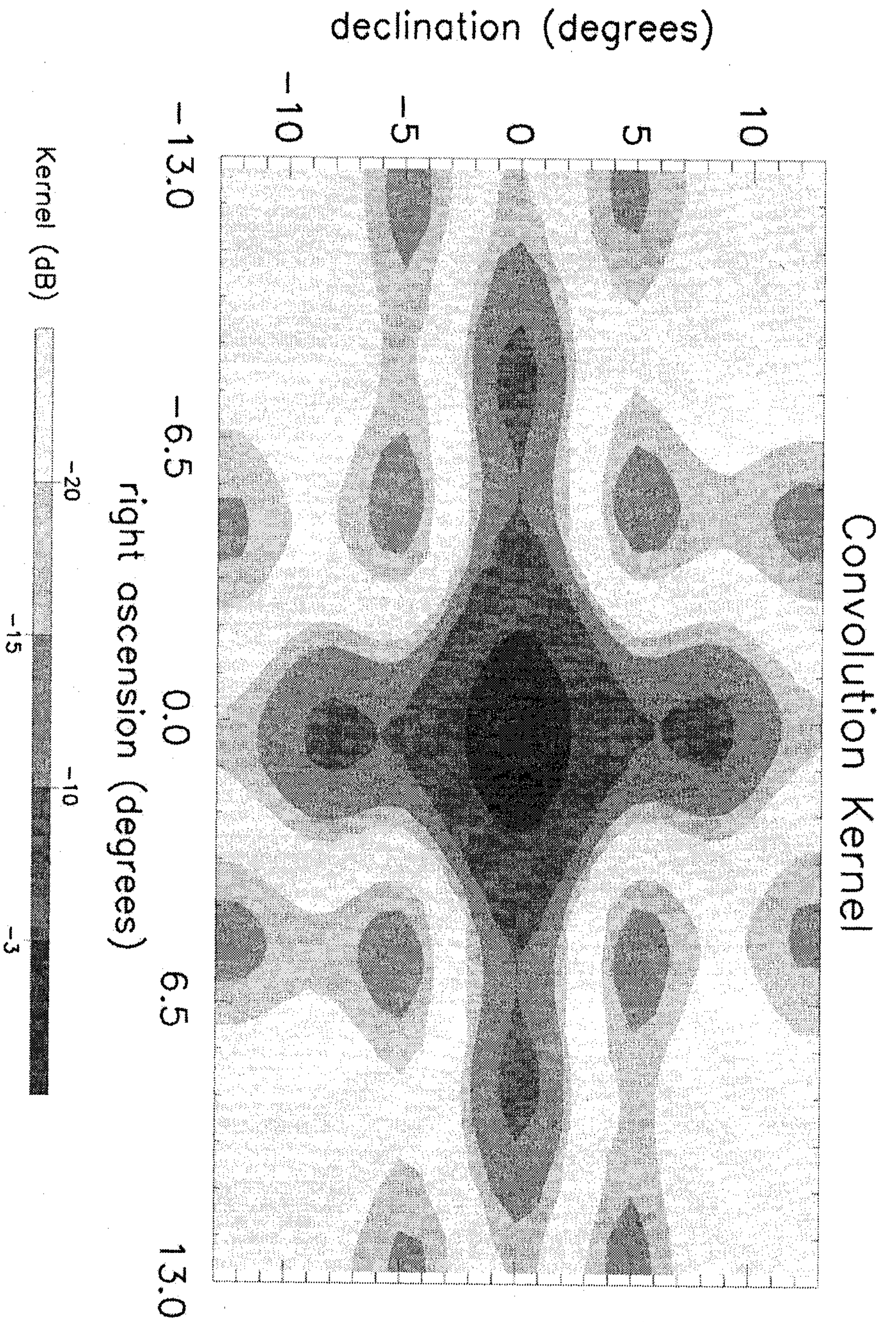

Figure 2.6. Kernel of convolution between the sky map and the radar antenna pattern.

2.3.2.2. Sky noise

Between 14 and 17 October 2004, the McGill VHF radar was operated according to the specifications given in Table 2.1. We selected the period in Figure 2.7, where the sky noise could be assumed to be due only to cosmic sources. From the measured Doppler power spectra, we computed the total integrated power (for spectral Doppler frequencies between -10.0 Hz and +10.0 Hz) at ranges between 17.5 and 22.5 km. At these high ranges, the Doppler power spectra received by VHF radars are basically formed by white noise, and when we integrate these spectra we obtain the so-called sky noise. We then used equation (2.19) to correct the total integrated power for not storing the full Doppler spectra. Notice that the temporal evolution of the sky noise power has a 23-hours-56-minutes cycle (i.e., a sidereal day). This confirms the dominant cosmic origin of the noise observed by our VHF radar.

In some cases, a few extreme, spurious power observations can be measured by VHF radars, and these observations correspond to signals from non-cosmic sources (e.g., human interference or broadcasting). These signals must be eliminated before proceeding with our calibration. In Figure 2.7, we have already filtered out these spurious data by eliminating sky-noise values that were six or more median-absolute-deviations away from the median sky noise (the median for the whole observation period).

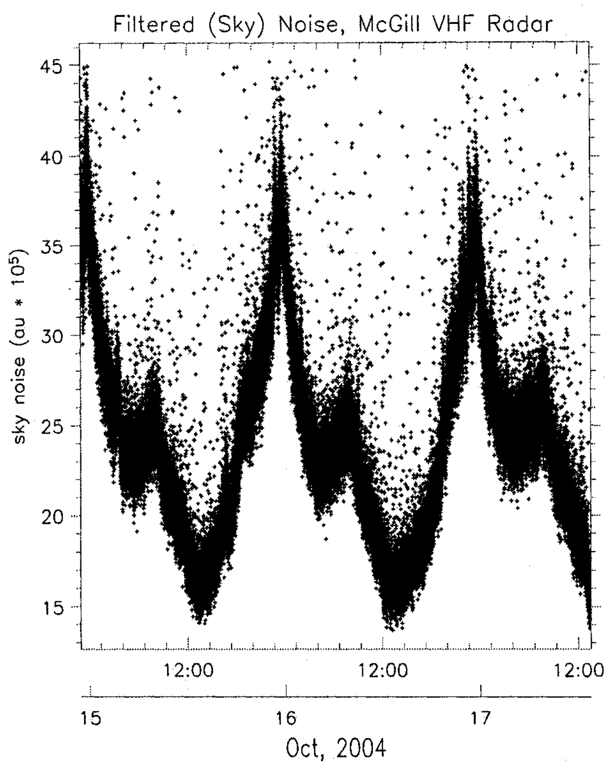

Figure 2.7. Example of a time series (in UTC) for sky-noise power [spectral integral within the Doppler spectral range and corrected by equation (2.19)], measured by the McGill VHF radar, with the beam at vertical direction, at ranges between 17.5 and 22.5 km, from 14 (starting at 22:50 UTC) to 17 (ending at 13:30 UTC) October, 2004.

By knowing the direction in the sky at which our radar is pointing at a given time, we can compute the equatorial coordinates (right ascension and declination) of this direction. We computed the radar pointing directions (for the cosmic sky-noise periods in Figure 2.7) by using standard astronomical procedures valid for the epoch J2004 [e.g., *Lang*, 1999]. Since our radar was located at a fixed longitude and elevation angle (vertical direction), our cosmic sky noises correspond to a fixed declination with varying right ascension. This is shown in Figure 2.8, where the VHF cosmic sky-noises (black and blue points, in 10^5 au) are plotted as a function of right ascension. Since our radar measurements correspond to a declination of 45.409°, we can compare our integrated powers with the corresponding 52 MHz sky brightness temperatures computed in section 2.3.2.1. These temperatures are over-plotted in Figure 2.8 as the red line (in kiloKelvins).

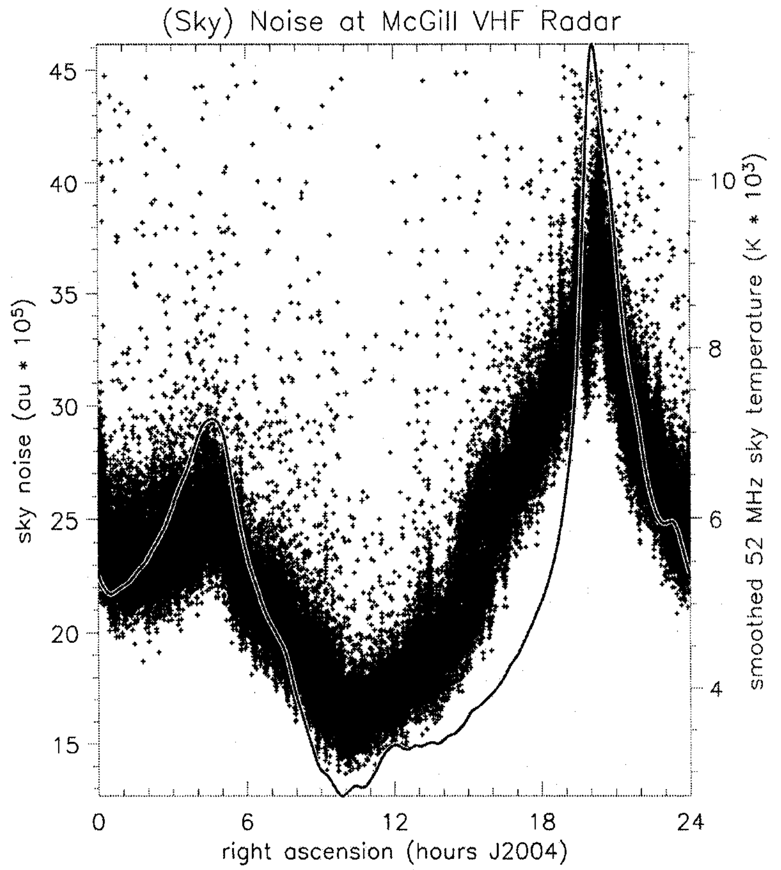

Figure 2.8. Cosmic sky noise measured by the McGill VHF radar. These correspond to nearly 63 hours of observations during conditions of negligible non-cosmic VHF radio-sources (between 14 and 17 October, 2004). The left-side Y-axis and the points correspond to radar measurements at ranges between 17.5 and 22.5 km. (The black points were measured during night time, between 23.1 UTC and 11.1 UTC. The blue points correspond to observations taken during the remaining day-time periods, between 11.1 and 23.1 UTC.) The red line and right-side Y-axis are obtained from the temperature values at the dashed line in Figure 2.4 (i.e., a declination of 45.409°), the radar antenna pattern in Figure 2.6 (i.e., the convolution kernel), and equation (2.5) with β=2.5.

The black observations in Figure 2.8, which correspond to night-time radar-measurements taken between 23.1 UTC (7:06 pm local time) and 11.1 UTC (7:06 am local time), match well with the corresponding sky temperatures (red points). However, the observations in blue, which corresponds to day-time measurements taken between 11.1 UTC and 23.1 UTC, tend to be above the corresponding sky brightness temperatures. For radio waves, day-time sky-noise is very challenging to analyze. On one hand, we have the power contribution from the Sun, which for our VHF band corresponds to a brightness temperature in the order of 10^5 K [*Subramanian*, 2004]. This temperature corresponds to about 10^{-13} Watts [from equations (2.5) and (2.6)]. On the other hand, there is the ionospheric absorption of radio waves, which affects all cosmic radiation when passing through the D and E ionospheric layers (at 60 to 100 km altitude). Ionospheric absorption is a well-known phenomenon, which is controlled in part by solar activity (i.e., sun spot number). Observations taken during the night are practically free from these inconveniences. We therefore filtered out all the measurements taken between 7:06 am and 7:06 pm (i.e., approximately between sunrise and sunset).

2.3.2.3. From arbitrary units to Watts

In order to obtain the sky-noise powers, the brightness temperatures (red points) in Figure 2.8 were multiplied by the Boltzman constant and the radar Band-Pass-Filter width [i.e., equation (2.6)]. However, the radar measurements (black points) in Figure 2.8 still had a large amount of scatter, which could complicate the empirical derivation of the coefficients in equation (2.4). We reduced this scatter in the following manner: for each P_{sky} observation (in Watts), we selected all radar observations (black points in Figure 2.8, in arbitrary units) that were within ± 45 seconds around the P_{sky} hour angle. (Recall that the resolution of the P_{sky} observations is 1.5 minutes.) The median of these radar observations was then the radar output power, P_{out}, to be matched to the P_{sky} observation. The matched pairs are shown in Figure 2.9 as right ascension time series, where the line corresponds to the sky-noise powers (P_{sky} , in Watts), and the points correspond to the P_{out} values (in arbitrary units).

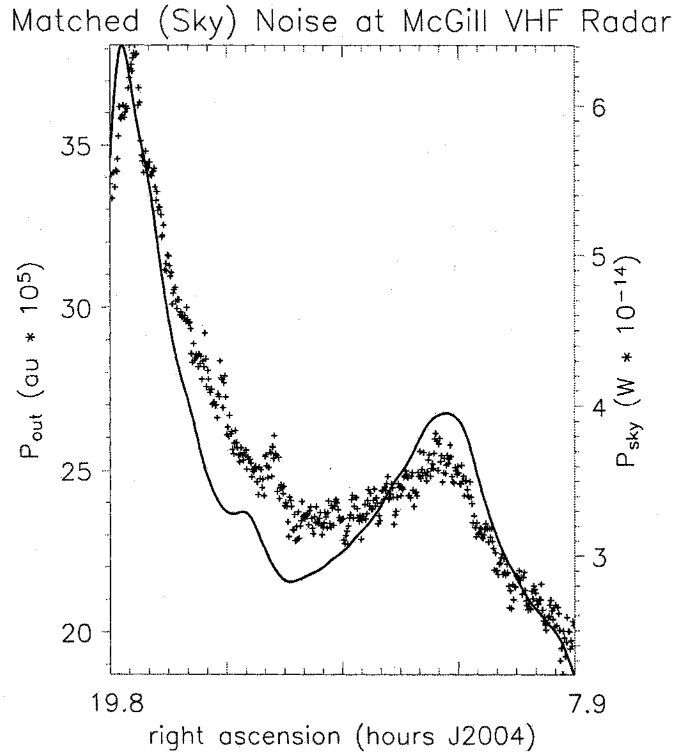

Figure 2.9. Expected and measured cosmic powers. The points and the left-side Y-axis (P_{out}, in 10^5 au) are obtained from median values of the radar measurements (black points in Figure 2.8). The line and the right-side Y-axis (P_{sky}, in 10^{-14} Watts) are obtained from equation (2.6) and the brightness temperatures in Figure 2.8.

To eliminate the unlikely possibility of having a lag between the two time series in Figure 2.9, we computed the cross correlation between the two series.

The maximum cross correlation was found at lag time equal zero (not shown). This means that no time lag can be found between the two time series, and if there is one, it will be less than the interval between two consecutive observations (i.e., 1.5 minutes). Thus, no lag- time correction was applied.

We can also visualize the data in Figure 2.9 by plotting P_{sky} as a function of P_{out}. This leads to the scatter plot in Figure 2.10 and the linear relation for power in Watts as a function of power in arbitrary units (the line in Figure 2.10). As described in section 2.2.2, we expect a linear relation, but the uncertainties about the variation of β in space [see equation (2.5)] could deviate the expected linear relation slightly. Fortunately, Figure 2.10 indicates that this small effect can be neglected in our case.

The data in Figure 2.10 might be described as two separate populations, each with a larger slope than the one given in the figure line. From equation (2.10), we know that a larger calibration slope in the figure dataset will imply a much smaller antenna efficiency e_R (in the order of the 35%), and this will disagree with the antenna efficiency estimations in the coming section 2.4 (i.e., e_R in the order of 50%). In addition, the data in Figure 2.9 does not support the existence of two separate populations; therefore, we discard this possibility.

A single linear relation between power in Watts and power in arbitrary units was then derived by minimizing the Chi-square error statistic, as in *Press et al.* [1986], and it is given as follows:

$$P_{sky} = \left(-1.797\times10^{-14} \pm 9.4\times10^{-16}\right)[W] + P_{out}\left(2.095\times10^{-20} \pm 3.6\times10^{-22}\right)[W/au] \ . \tag{2.27}$$

As before, the units are given in square brackets, and the uncertainties correspond to one standard-deviation errors in the coefficients estimates.

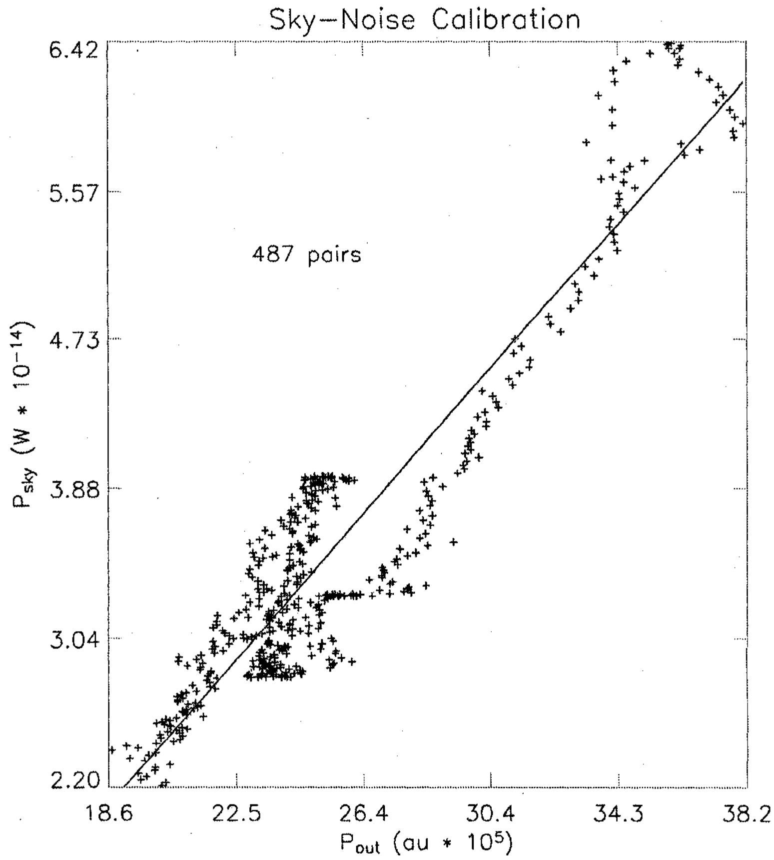

Figure 2.10. Scatter plot of expected versus measured cosmic sky-noise power. The Y-axis values (P_{sky} , in 10^{-14} Watts) correspond to the line in Figure 2.9. The X-axis values (P_{out}, in 10^5 au) are the corresponding points in Figure 2.9. The line here corresponds to equation (2.27).

2.3.3. Radar hardware coefficients

In order to calculate the values of antenna and receiver parameters, we need to compare our two sets of calibration equations [i.e., the sky-noise calibration in equation (2.27) and the noise-generator calibration in equation (2.26)]. The comparison is shown in Figure 2.11, where the sky-noise calibration is plotted as a dashed line and the noise generator calibration is given as a continuous line. Of course, the slope of the noise-generator calibration is smaller than the slope of the sky-noise calibration, and we expect this difference from equation (2.10).

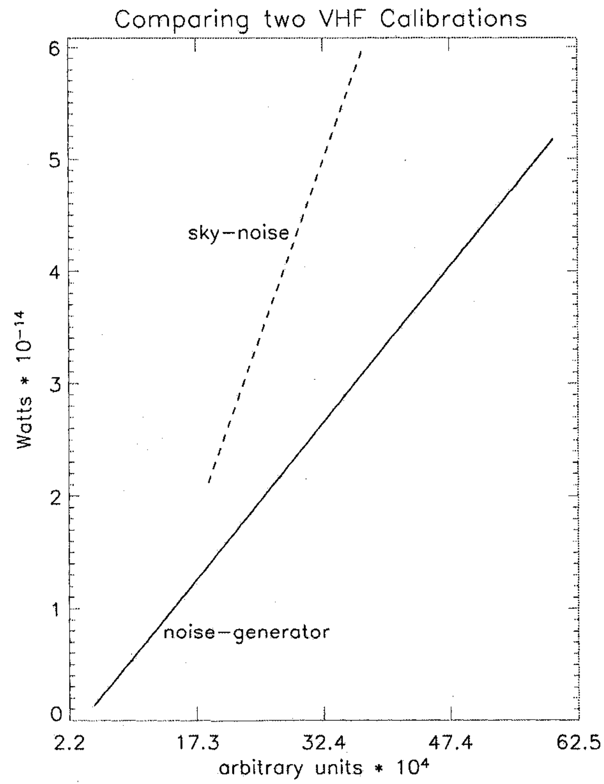

Figure 2.11. Comparison of noise-generator and sky-noise calibrations. The sky-noise calibration [equation (2.27)] is plotted as a dashed line, and the solid line represents the noise-generator calibration [equation (2.26)].

The hardware parameters can now be computed from equations (2.7), (2.8), (2.10), and (2.11) simply by noticing the correspondence between equations (2.4) and (2.27), and between (2.3) and (2.26). As well, their corresponding uncertainties are estimated from equations (2.13) to (2.16). These values are given in Table 2.2. Notice that the antenna efficiency in Table 2.2, $e_R = 44\%$, refers only to reception. The antenna system was originally designed to maximize transmitted power, and the overall power losses on transmission are estimated to be less than 2 dB [*Mardoc Inc.*, 2006, personal communication]; i.e., $e_T = 63\%$.

Table 2.2. Hardware parameters obtained from calibration

Parameter	Value	Uncertainty
e_R	0.442	0.008
N_a	$1.14x10^{-14}$ W	$4x10^{-16}$ W
g_{Rx}	$1.081x10^{20}$ au/W	$3x10^{17}$ au/W
N_{Rx}	$3.70x10^{5}$ au	$7x10^{3}$ au
T_{Rx}	619 K	12 K

To compute the receiver noise temperature, T_{Rx}, we use an equation similar to equation (2.6); i.e., $N_{Rx}(W) = k_{Boltzmann}\ T_{Rx}\ BPF_{width}$, where $N_{Rx}(W)$ is the receiver noise expressed in units of Watts. This receiver noise can be computed from the N_{Rx} value in Table 2.2 and the slope in equation (2.26), or from the offset in equation (2.26). In both cases, we obtain that the receiver noise temperature (for the McGill radar) is about 619 ± 12 K.

2.4. Antenna matching unit

To validate our results, we will now study the various subcomponents of the radar antenna that are most likely leading to power losses. This analysis leads to a third calibration method, which will provide an independent estimation of the antenna efficiency.

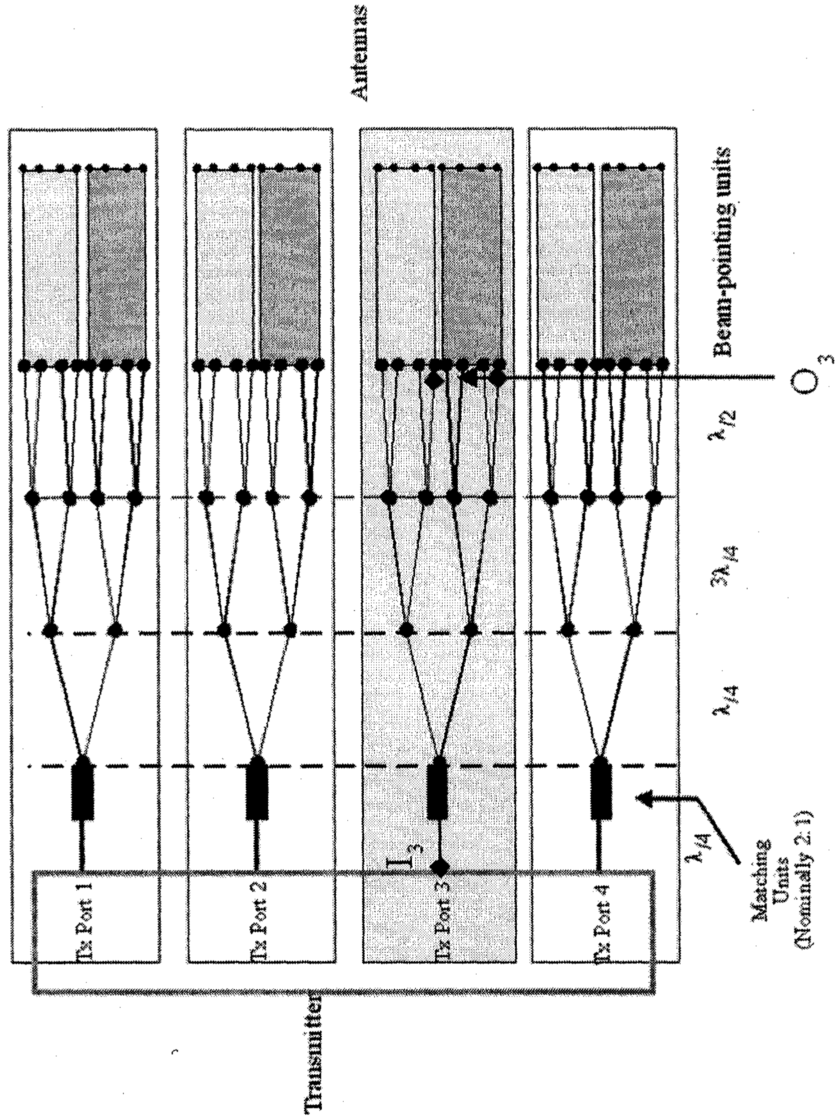

Figure 2.12. Matching between transmitter and antenna aerials (Antennas) for the McGill VHF radar. Each cable has a length as specified at the bottom of the diagram, expressed in form of wavelength λ, where λ is the electromagnetic wavelength within the coaxial cable. Cables are joined using T-shaped connectors. The matching boxes are combinations of capacitors and conductors that permit matching of 25 Ω to 50 Ω. There are four transmitter ports, each feeding eight antenna aerials. The shaded portion (output port 3, O_3) was used separately for further tests, as discussed in the text.

In this regard the antenna transmission lines are the most important. In order to minimize energy losses, the impedance in the antenna aerials is matched to the transmitter impedance through an arrangement of coaxial cables. These assemblies of cables are then called the antenna matching units. For the McGill VHF radar, we use a matching arrangement like the one shown in Figure 2.12. This includes matching cables made from RG213 coaxial cable, with lengths as indicated in the figure, and beam-pointing boxes that are used to introduce phase delays to the antennas in order to implement beam pointing. The internal details of the beam-pointing boxes are not shown on the figure, but the efficiency of these units will be considered separately in due course. The matching boxes at the Transmitter end hold inductors of approximately 75 nH and capacitors to earth of about 60pF, which are tunable in order to provide final accurate matching.

The arrangement in Figure 2.12 includes matching boxes and switching boxes. In order to assess the performance of this arrangement, we have built a slightly simpler system which contains no switching boxes, and used it for performing the third calibration method. This arrangement is shown in Figure 2.13. We will first discuss the operation of this unit, and consider theoretical efficiencies. Following this, we will report the results of a series of measurements on the system, and compare with theory. Finally, we will return to the original matching arrangement (Figure 2.12) and make further measurements, which can then be interpreted in terms of our results using Figure 2.13.

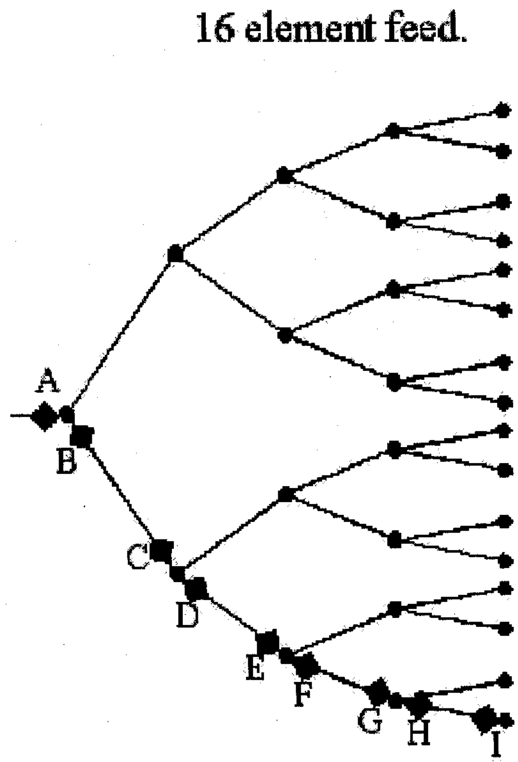

Figure 2.13. Simplified antenna-diagram during transmission. The transmitter feed is at point A, and the antenna aerials connect at the 16 output ports above point I. Cable lengths are specified in the text.

In order to properly understand the efficiency of an impedance matching system, like that shown in Figure 2.13, it is necessary to consider both its forward and backward transmission characteristics. The cable impedance is assumed to be 50 Ω. The simplified transmission lines shown in Figure 2.13 had cables lengths of one half of a wavelength between H and I, one quarter of a wavelength between G and F, one half of a wavelength between E and D, and one quarter of a wavelength between C and B. We assume that the antennas are all tuned to 50 Ω. Where two cables come together as at G/H, the point G (looking out towards the antenna aerials) sees an impedance of 25 Ω. The quarter wave section F-G transforms this to 100 Ω. The point E, looking out towards the antenna aerials, sees an effective impedance of 2 × 100 Ω impedances in parallel, or 50 Ω. The point D, looking out towards the antenna aerials, also sees 50 Ω. Point C sees 2 × 50 Ω impedances in series, and so sees 25 Ω. This maps to 100 Ω at B (looking towards the antenna aerials). Finally, point A sees 2 × 100 Ω impedances in parallel, or 50 Ω. These results are summarized in the fourth column of Table 2.3.

Table 2.3. Impedance at different points of the antenna transmission lines, for the McGill VHF radar.

Point in Figure 2.13	Looking towards transmitter (Transmitter terminated in 50 Ω)		Looking towards aerials (all aerials terminated in 50 Ω)	
	Theory	Measurement ± [0.5 Ω, 1.0°]	Theory	Measurement ± [0.5 Ω, 1.0°]
A	[50.0 Ω, 0°]	[50.0 Ω, 0°]	[50.0 Ω, 0°]	[48.0 Ω, 13.0°]
B	[33.3 Ω, 0°]		[100.0 Ω, 0°]	
C	[75.0 Ω, 0°]	[75.5 Ω, -1.4°]	[25.0 Ω, 0°]	[26.8 Ω, 5.9°]
D	[30.0 Ω, 0°]	[31.5 Ω, 5.6°]	[50.0 Ω, 0°]	
E	[83.3 Ω, 0°]	[80.9 Ω, 3.5°]	[50.0 Ω, 0°]	[49.0 Ω, 8.8°]
F	[45.45 Ω, 0°]	[44.4 Ω, 3.5°]	[100.0 Ω, 0°]	
G	[55.0 Ω, 0°]	[57.5 Ω, -4.0°]	[25.0 Ω, 0°]	[26.5 Ω, 11.8°]
H	[27.25 Ω, 0°]		[50.0 Ω, 0°]	
I	[27.25 Ω, 0°]	[29.0 Ω, 7.5°]	[50.0 Ω, 0°]	

The fifth column in Table 2.3 shows actual measurements of the impedances, expressed as magnitudes and angles, as measured by a Hewlett-Packard Vector-Impedance Meter. Agreement with theoretical expectations is good, and differences are due to the facts that (i) the characteristic impedance of the cable was actually close to 51 Ω, and (ii) slight errors in cutting the lengths of the cables to exact multiples of a quarter of a wavelength. (Optimal cable lengths were determined using a vector-impedance meter, with the cables being open circuit. The quarter-wavelength cables were cut until impedance was zero, and the half-wavelength cables were cut until impedance was maximum.)

In the previous paragraph we examined impedance transformations in the matching unit, comparing theoretical and experimental values. It is also necessary to examine power transmission, which is best done by looking at voltages at various points along the antenna transmission lines.

A continuous-wave 52.00-MHz signal, of peak-to-peak voltage equal to 1.16 V (as measured into a Cathode Ray Oscilloscope loaded with 50 Ω), was fed into the point A in Figure 2.13. In addition, all terminations except that at "I" were given 50 Ω loads. The voltage measured into a 50 Ω load at "I" was then equal to 28 mV peak to peak. It would be expected that the applied power should be equally distributed across all loads, so that if the input power is $\frac{1}{2} \times \frac{1.16^2}{50}$, then the output voltage should be 29 mV. The total cable length from input to output is 1.5 wavelengths, or 5.71m, since the velocity propagation factor for RG213 cable is 0.66. This RG213 coaxial cable has a loss factor of 1.3 dB per 30m at 52 MHz, so losses of 0.25 dB are expected. This should reduce the received signal to a peak voltage of 28.2 mV, consistent with our measured value. Hence the losses on transmission through such a matching unit are about 0.2 dB, mainly due to cable attenuation.

In considering the system efficiency of a transmit-receive system like this, it is also necessary to consider the return path of the signal. It is well known that with a well designed antenna array, the sky noise received by the radar is independent of the number of antenna aerials, provided that the sky noise is isotropic in origin. Suppose that a single antenna aerial is used, and fed directly into point A in Figure 2.13, from where it passes through a transmit-receive switch to a receiver. Let the signal power received be P. Now suppose that 16 antenna aerials are now used, and are fed by the matching arrangement in Figure 2.13. Each antenna aerial receives power P, but as the signal passes back through the stages of the matching unit, more and more is lost by reflections. Some of it ends up being re-radiated by other antenna aerials in the array. In fact the power expected at the point A due to the signal received at one antenna is only P/16. The accumulated power from all antenna aerials is 16 times this, or P. In terms of polar diagrams, this result can be determined by recognizing that the collection of 16 antenna aerials has a narrower polar diagram than a single antenna aerial, but in terms of the actual matching used, the result arises because of power losses due to reflections on the return path. The received signal strength (and therefore the sky-noise temperature) is thus independent of the number of antenna aerials used. This is a well-known result that is employed in calibrating many radio systems, and it has been used in the early sections of this chapter as well.

To see this more clearly, it is a simple matter to determine the impedances seen at various stages of the matching path looking back towards the transmitter (as opposed to the previous cases, which were determined looking out towards the antenna aerials). To begin, consider the point B (in Figure 2.13) looking back towards the transmitter. It sees a 50 Ω load in the form of the transmitter, and a

100 Ω load coming in from the other arm of the V-section closest to the transmitter. Hence point B sees 33.3 Ω. This maps to 75 Ω at point C due to the quarter-wavelength section. By working along the matching unit from A to I, the impedances seen in the second column of Table 2.3 can easily be deduced. In Table 2.3, column 3 shows experimental values of the impedances, and again agreement between theory and experiment is good.

It is now necessary to determine the power expected to be received at the point A, assuming that this point is terminated in 50 Ω, and all other cables above the point I in Figure 2.13 are also terminated in 50 Ω. This can be calculated by looking at transmission efficiencies at each point. For example, a 50 Ω input applied at point I sees an impedance of 27.25 Ω, so a voltage reflection coefficient of (50-27.25)/(50+27.25) = 0.2945 applies. Hence the reflected power is 8.7% of the original. The transmitted power is therefore 91.3% of the original. This transmitted signal progresses to the junction between G and H, where some signal passes through to G, some is reflected back, and yet more of the signal passes into the adjoining cable and is transmitted into the next termination (or, in a real radar, is transmitted into the next antenna aerial). The signal that is reflected back to I is partly retransmitted from I into the adjoining load, and partly re-reflected back to H – and so forth. The signal that passes through G suffers further reflection and splitting at E/F, and so forth. Eventually, only one sixteenth of the original signal arrives at the point A.

Experimental testing of this pathway was carried out. An input signal of 1.16 V peak-to-peak fed in at "I" produced a signal of 0.26V peak-to-peak at point A.

Inserting inputs at other locations similar in location to point "I" gave outputs at the point A in the range 0.24 to 0.27 V peak-to-peak. These results are entirely consistent with the above expectations, and indicate that even on the return path the losses of this matching unit are very modest, and certainly less than 10%, even including losses due to cable attenuation.

We now return to Figure 2.12. Having performed the above tests, a sub-unit of Figure 2.12 (shaded in the figure) was extracted for further tests. As for the circuit in Figure 2.13, forward propagation (from the transmitter out to the antenna aerials) was very efficient. For the reverse direction, Figure 2.14 shows a series of measurements. In this case the input signal was 90 mV peak-to-peak. The beam-pointing units were removed from the circuit.

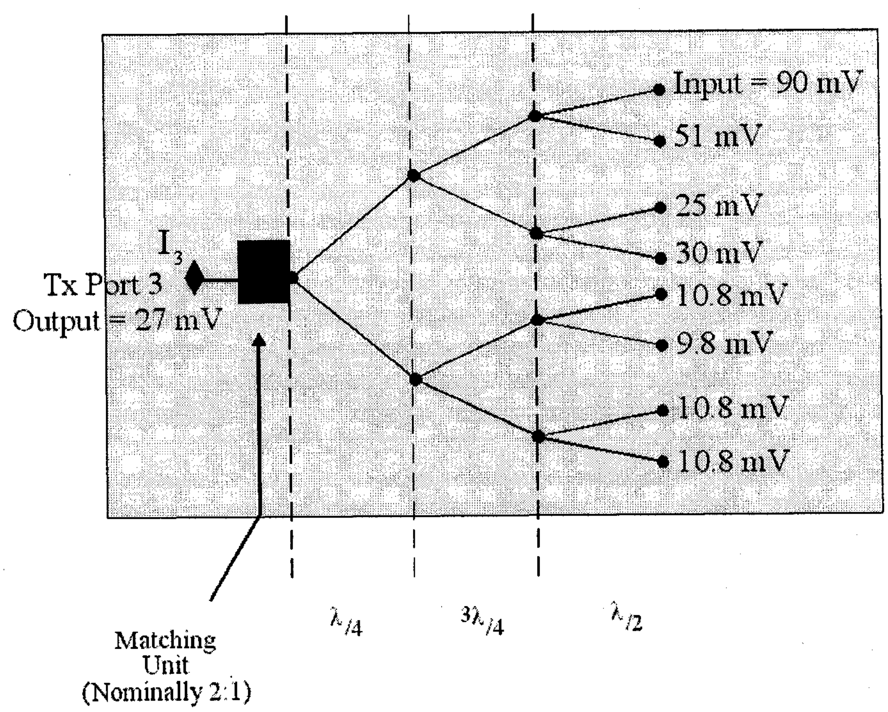

Figure 2.14. Simplified antenna-diagram during reception. (Antenna aerials connect to the right.)

Figure 2.14 shows more clearly the distribution of power around the circuit. Notice that the input power is proportional to $(90)^2$ V^2, but as before, only about 91% of the input power enters the matching unit, and the rest is reflected back into the signal generator, due to the mismatch at the input. Since all voltages were measured into 50 Ω, we will dispense with converting powers to Watts, and express them in terms of Voltage squared. The transmitted power is therefore proportional to 7200 V^2. It should be noted that if all of the power produced at all the other remaining ports are summed, $(51^2 + 25^2 + ... + 10.8^2 + 27^2)$, the result is 5300 V^2 – less than, but comparable to, the total input power. Some of the signal travels over relatively long paths, up to 3 wavelengths (e.g., signal that travels form the input, to I_3, and back to one of the antenna aerials), so losses of the order of 0.5 dB are possible due to cable losses and connector losses. If such losses are considered, the total available power is proportional to $7200 \times 10^{-0.05} = 6400$ V^2, very similar to the 5300 V^2 outputted. Of most importance is the fact the signal strength returned to the receiver at I_3 is very close to the ideal value of $90/\sqrt{8}$ = 31.8 mV, and some of this lost is due to cable losses. Thus the efficiency of this matching unit for reception is of the order of $(27/31.8)^2$, or in other words the losses are of the order of 1.4 dB. Measurements along other arms gave slightly less losses, and overall the system loss due to this matching unit for the returned signal should be less than 1 dB.

The above test was repeated, but this time we included the beam-pointing boxes. These units added a further 0.5 to 1 dB to the system losses, varying slightly from one unit to the next. In addition, the cable to the antennas is

Andrews ½" Heliax, which has a loss of 0.5 dB per 30 meters. Each output port feeds to a separate quartet of 4 antenna aerials, and distances to the inner antenna aerials are typically 35 meters, and the outer ones are 76 meters. All cables are carefully cut to integral numbers of wavelengths in length. Therefore cable losses are of the order of 0.5 to 1 dB. Some small losses can be expected at the final antenna matching unit, but they should not be large. Hence due to antenna matching issues, we anticipate that the overall system efficiency should be of the order of -2 to -3 dB, being comprised of about 1 dB in the matching unit, 0.5 to 1 dB in the beam-pointing boxes, and 0.5 to 1 dB in the cables that carries the signals to and from the antenna aerials. Checks of inter-path coupling between different paths in the beam-pointing units showed that such coupling is generally of the order of –30 dB, and this is not likely to introduce further inefficiencies.

Therefore, these antenna-matching calculations give an extreme value of -3 dB for antenna losses in the McGill VHF radar. This laborious estimation have not considered other, less significant, power losses (e.g., at the final antenna-matching unit, where the cable feeds four antenna aerials). Consequently, the estimation is in general agreement with the antenna efficiency value obtained in Section 2.3 (from Table 2.2, $e_R = 0.442 = -3.5$ dB).

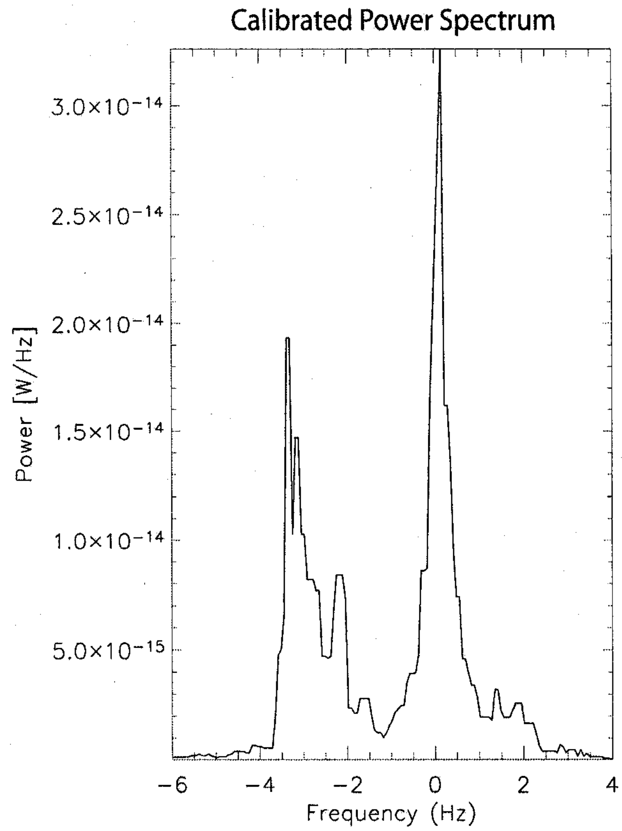

Figure 2.15. Calibrated power spectrum measured by the McGill VHF radar. Negative velocities correspond to downward motions. The calibrated Doppler spectrum was smoothed (by using a 5-point running median) in order to produce the spectrum plotted here.

2.5. Precipitation applications

When we applied equation (2.24) to the non-calibrated power spectrum output by our radar signal processing (i.e., power densities in au/Hz), we obtain the calibrated power spectrum of Figure 2.15 (i.e., power densities in W/Hz). This figure corresponds to a 2.5 km range gate, for a rain event on 9 September 2004, at 14:05:45 UTC. (The 2.5-km range is the lowest range gate that we can use for precipitation retrievals, and this is determined by the antenna far-field region and the time response of the radar transmitter-receiver switch.) The bimodality is due to the simultaneous detection of clear-air signal (peak near 0.2 Hz) and rain signal (peak near 3.5 Hz). As a reference, we measured at ground level (for the same time) a 1-minute rainrate of 13 mm/h. Similarly to our observations in Figure 2.15, *Gage* [1990, and references therein] discusses an example of Doppler spectrum showing clear-air and precipitation echoes during light rain. The advantage in our case is that we express our ordinate—calibrated by our technique—in W/Hz, while the power densities in *Gage*'s Figure 3.7 are in arbitrary units.

Furthermore, we can convert our calibrated power spectra into reflectivity spectra (expressed in units of m^{-1}/Hz) by using a proper radar equation, e.g. [see equation (3.28), Chapter 3]

$$\bar{\eta} = \frac{256\pi^2 \ln 2\,[(R)^2 - (L/4)^2]}{P_{Tx}\, e_T\, (D_{\max})^2\, \lambda^2\, L\, \theta_0^{\,2}} P_r\ ; \tag{2.28}$$

where $\bar{\eta}$ is the reflectivity averaged over the sampling volume, R is the range (in meters), L is the transmitter pulse length (in meters), D_{max} is the antenna maximum directivity, λ is the radar wavelength (in meters), and θ_0 is the one-way half-power half-beamwidth. By integrating the part of the reflectivity spectra that corresponds to clear-air signal (frequencies larger than -1.25 Hz for the observations in Figure 2.15), we could compute an estimate of air turbulence in precipitation conditions; i.e., energy dissipation rates as in the method by *Hocking* [1985, Appendix A]. We can also obtain an estimate of the precipitation intensity from the spectra in Figure 2.15.

As an example, Figure 2.16 shows reflectivity-factor spectra obtained simultaneously by the McGill VHF radar and by ground measurements of raindrop-size distributions. The abscissa (X-axis) has been changed from Doppler frequency shift, f, into Doppler velocity, v, by using the relation $f = 2\,v/\lambda$. The VHF precipitation spectra are wider and a bit shifted towards the negative velocities. This is because the beam width is larger in the VHF than in the raindrop-size sensor, because air velocities are different in the sampling volume of each sensor, and because the change of air density with height implies a 10% increase in raindrop fall velocity at 2.5 km height [e.g., *Beard*, 1985]. However, in general there is good agreement between both spectra, which demonstrates the potential of using power spectra—calibrated by our technique—for retrieving meteorological information such as precipitation bulk quantities (e.g., reflectivity factor and rain rates). These meteorological variables are typical in radar meteorology, where microwaves are most often used instead of longer-wavelength radio waves. The advantage is that, with the use of VHF radio waves, we can also retrieve information about the air motion independently and simultaneously to the precipitation. We will discuss this application more in detail in the subsequent chapter.

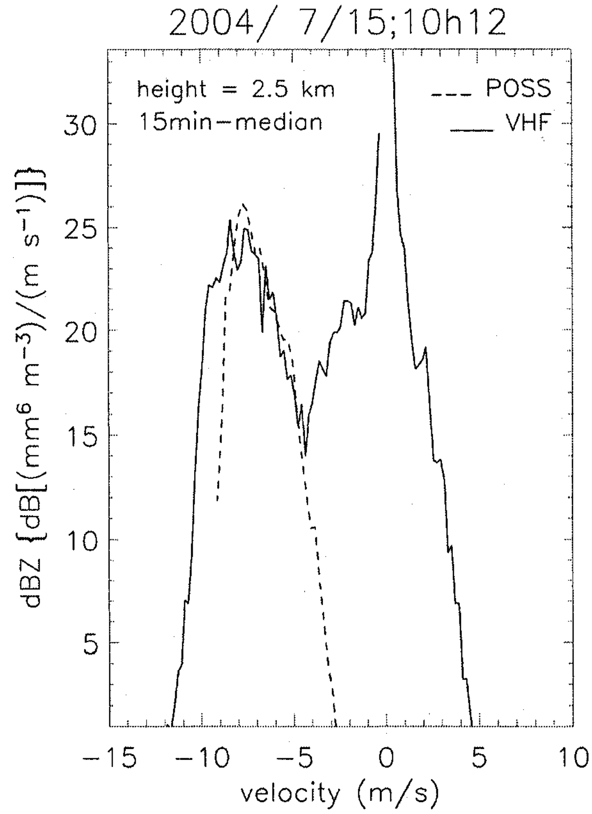

Figure 2.16. Comparison of precipitation signal simultaneously measured by a VHF wind profiler and by a drop-size distribution sensor. The figure plots Doppler spectra of reflectivity factors (in dBZ), where the continuous line corresponds to the VHF observations taken by the McGill VHF radar, at 2.5 km height. The dashed line corresponds to drop-size measurements taken at ground by a POSS sensor [instrument described by *Sheppard*, 1990]. The plotted spectra correspond to the median values over 15 minutes, taken on 15 July 2004, at around 10:12 UTC, over Montreal, Canada.

2.6. Discussion

When dealing with the power measured by VHF radars, it is often necessary to convert power units (from the arbitrary units of the analog-to-digital converter) into Watts. A radar calibration is then required. This chapter discussed an integrated, multiple-method approach for obtaining this calibration, using noise-generator calibration and sky-noise calibration methods, and intelligent integration of the methods. There are important inconveniences associated with using exclusively one or the other. The noise-generator method requires hardware (the noise generator) that is not always available at the radar site, and the normal operation of the radar has to be interrupted to connect this hardware. Furthermore, the calibration equation that results does not take into account the antenna losses, and is therefore not accurate. On the other hand, attempts to calibrate VHF radars using the sky-noise method have only been reported a few times in the literature. This is most probably related to difficulties in obtaining reference sources of cosmic radiation at VHF band. Although this limitation has now been overcome, sky-noise calibration-methods do not provide independent information on the receiver or antenna parameters. This information on radar parameters is fundamental when applying the radar equation to derive meteorological variables such as turbulence and precipitation.

We overcame these calibration difficulties by combining the sky-noise and the noise-generator methods. We present here a more complete approach to radar calibration for operations in the VHF band. In addition, our technique allows derivation of several antenna and receiver parameters and their corresponding uncertainties. We give these parameters for the McGill VHF radar in Table 2.2. The application of our calibration technique to the McGill VHF radar measurements generates calibrated power spectra like the one in Figure 2.15.

Another advantage of our calibration technique is that, once the noise-generator part has been applied, the rest of the calibration can be performed during routine observations (without the need for additional hardware or modification of the radar operation). Furthermore, a change in the radar hardware does not require a new noise-generator calibration. We simply perform a new sky-noise calibration [i.e., we obtain $A_{sky}(new)$ and $B_{sky}(new)$ for Equation (2.4)]. For a change in the radar antenna, the noise-generator coefficients in Equation (2.3) will remain the same. We will then apply our calibration technique using the old noise-generator coefficients and the new sky-noise coefficients. For a change in the radar receiver, the antenna efficiency and antenna noise would remain the same. Then, we obtain from Equation (2.10) that

$$B_{NG}(new) = \frac{B_{NG}(old) \quad B_{sky}(new)}{B_{sky}(old)} \quad . \tag{2.30}$$

As well, from Equation (2.11) we find that

$$A_{NG}(new) = A_{sky}(old)\frac{B_{NG}(old)}{B_{sky}(old)} + A_{NG}(old) - A_{sky}(new)\frac{B_{NG}(new)}{B_{sky}(new)} \quad . \tag{2.31}$$

At this point, the new coefficients for Equations (2.3) and (2.4) are available and our calibration technique can be applied.

For best implementation of our calibration technique, it is very important to select night observation periods when unknown variations of cosmic power (e.g., solar emissions and ionosphere attenuation of the cosmic power) are minimal. It is also important to minimize any non-cosmic radio sources (e.g., broadcasting signals) from the calibration data. The amount of non-cosmic radio sources depends on the radar location (an urban site will probably have much more non-cosmic radio sources than a remote site), and the removal of affected periods can be done as in Section 2.3.2.2.

Our calibration technique does not consider the power losses in the radar transmitter or between the transmitter and the transmitter-receiver switch. In general, these omissions are not very relevant, since the length of the cables between the transmitter and the transmitter-receiver switch are not very long (i.e., very high transmitter efficiencies). As well, radar manufacturers usually provide a calibrated transmitter.

In order to validate the results from our calibration technique, we applied a third calibration method. The third method corresponded to antenna-matching calculations, which provided an independent estimate of the antenna power lost. We found this estimate to agree with the antenna efficiency derived by our calibration technique.

This chapter has concentrated on the correct measurement (in units of Watts) of power by VHF radars. However, we have also demonstrated the potential of using the Doppler spectra calibrated by our technique, in combination with the values of radar hardware parameters derived by our technique, for retrieving meteorological information such as precipitation bulk quantities (e.g., reflectivity factor and rain rates). Nevertheless, the derivation of precipitation quantities requires relating the spectra and hardware parameters to a proper radar equation (i.e., the relationship between power and targets backscattering cross-sections). As well, a method for separating the precipitation mode from the air mode has to be implemented. We will elaborate more on this application in the subsequent chapter.

CHAPTER 3:

MEASURING RAINFALL AND VERTICAL AIR VELOCITIES USING ONLY OBSERVATIONS WITH A VHF RADAR

ABSTRACT

This study shows how the measurement of rainfall and vertical air velocities can be performed using only observations from a radar operating at the VHF band (i.e., meter wavelengths). We verify the assumption that the dielectric factor $|K|^2 = 0.93$ is valid for rain observations in the VHF band. We then derive—analytically and numerically—a more general version of the radar equation valid for vertically pointing radars with targets within a few kilometers range, but still within the antenna far-field region. Following this, we describe a new algorithm for extraction of rain signal out of VHF Doppler spectra. To validate our methods, we made co-located measurements of VHF Doppler spectra aloft and raindrop sizes at the ground. The analytical version of our radar equation compares well with similar equations available in current literature, and this validates the particular case of our numerically-derived radar equation. We combine our numerical version of the radar equation and our algorithm for extracting precipitation signal. This combination allows us to obtain reflectivity factors (from rain signals) and vertical velocities (from air signals), these being simultaneous observations within the same sampling volume. From the dataset collected, we found good agreement (linear correlation coefficient around 0.8) between the rain signal derived from VHF observations aloft and from drop sizes at ground level. Hence, we are able to measure rainfall amounts and vertical air velocities in a simpler and more efficient way, using only observations from a VHF wind profiler. This represents a promising step towards the analysis of precipitation from large radar datasets.

3.1. Introduction

Quantitative interpretation of precipitation measurements by radars involves the representation of the radar signal in terms of the reflectivity factor (i.e., Z expressed in units of $mm^6\ m^{-3}$). For vertically-pointing radars operating in the VHF band (i.e., meter wavelengths), we have the advantage of measuring also air vertical velocities, in addition to the precipitation signal. For this reason, meter-wavelength radars might be more desirable, for the study of precipitation physics, than traditional centimeter-wavelength radars. For this to happen, however, we must

(a) Calibrate the measured power density spectra;

(b) Extract the signal originating for precipitation, an additional step compared to centimeter-wavelength radars;

(c) Express this received power P_r in terms of the scatterers cross sections (i.e., radar reflectivity, η, expressed in units of m^{-1}); and then

(d) Express this radar reflectivity in terms of the reflectivity factor Z.

For the case of precipitation particles being the scatterers of our VHF radar pulse (i.e., Rayleigh scatter), requirement (d) can be satisfied by using the following expression [e.g., *Rinehart*, 1997, equation 5.13]:

$$\eta_{precip} = \frac{\pi^5 |K|^2}{\lambda^4} \frac{Z}{10^{18}}. \qquad (3.1)$$

where $|K|^2$ is the dielectric factor, and λ is the wavelength of the radar transmitted pulse (in meters). Z is the reflectivity factor (expressed in $mm^6\ m^{-3}$). The value of $|K|^2$ depends upon the scatterer material, the scatterer temperature, and the radar wavelength. Unfortunately, estimations for the values of $|K|^2$ at

VHF band are not readily available in the wind-profiler literature. Typically, the $|K|^2$ value for S-band ($|K|^2 \approx 0.93$ for water sampled at 10 cm wavelengths) is used instead [e.g., *Chilson et al.*, 1993].

By convention [e.g., *Smith*, 1984], if $|K|^2$ is taken equal to 0.93 (the value corresponding to liquid water at near 20°C, and wavelengths in the S band), then $Z = Z_e$, the equivalent radar reflectivity factor that is generally plotted on radar displays. This convention is adopted because when radar measurements are made, one is often not certain of the hydrometeor phase or composition. However, it is still necessary to verify if the assumption of $|K|^2 = 0.93$ is also valid in the VHF band.

The other three requirements are not attained as directly as with requirement (d), and they represent a challenge that has been met only partially in the current literature [e.g., *Lucas et al.*, 2004; *Kobayashi and Adachi*, 2005; and references therein]. For example, we can accomplish requirement (c) by using the radar equation (i.e., the relationship between η and P_r). Unfortunately, there are several versions of this radar equation that are very often valid only for particular radar configurations [e.g., *Probert-Jones*, 1962; *Gage and Balsley*,1980; *Hocking*, 1985]. Furthermore, the derivation of such equations is not always presented in detail in the literature. Requirement (b), on the other hand, is accomplished through elaborate algorithms of signal processing [e.g., *Rajopadhyaya et al.*, 1993; *Boyer et al.*, 2001] or by multi-wavelength techniques [e.g., *Maguire and Avery*, 1994; *Schafer et al.*, 2002]. Adjustment and refinement of these algorithms require long periods of numerical experimentation with the corresponding radar datasets. Concerning requirement (a), we should recognize that, very often, power density spectra recorded by VHF radars are not expressed in units of Watts per frequency bin, but only in the arbitrary units of the radar receiver hardware. Requirement (a) then involves a radar calibration, which has already been analyzed in Chapter 2.

In the present chapter, we present our efforts towards the accomplishment of requirements (b), (c), and (d). We will be focusing on the case of precipitation being rain, because it gives us a signal that is easy to separate from the clear-air signal in the power density spectrum, and also because it avoids the inconvenience of not knowing the exact $|K|^2$ value for solid precipitation (e.g., snow and graupel). Concerning requirement (d), we verify the assumption that $|K|^2 = 0.93$ for most of the rain observations at VHF band. For requirement (c), we derive a general version of the radar equation valid for vertically pointing radars, as well as a particular version of this equation valid for the McGill VHF radar. Then, a numerical algorithm for extracting the rain signal out of the VHF power spectra is presented to achieve the requirement (b). The next section describes the theoretical considerations for these three requirements. We then combine our radar equation and our algorithm for extracting rain signal in section 3.3, which allow us to retrieve reflectivity factors and air vertical velocities during several rainfall observations at Montreal. As well, we validate our method by comparing our results with the rain signal from raindrop sizes measured at the ground. A discussion of our results is presented in the last section of this chapter.

3.2. Methods

3.2.1. Computing the dielectric factor at VHF

In order to accomplish requirement (d), from the Introduction section of this chapter, we consider equation (3.1). It is clear that the knowledge of $|K|^2$ at VHF band is required in our analysis (and in any quantitative analysis of precipitation using radars). For Rayleigh scattering, the scatterer dielectric factor, $|K|^2$, is a function of the scatterer's complex refractive index, m, such that [e.g., *Marshall and Gunn*, 1952, p.322; *Battan*, 1973, p.38]

$$\mathrm{K} = \frac{m^2 - 1}{m^2 + 2} \,. \tag{3.2}$$

At the same time, m varies with scatterer temperature and radar wavelength. Unfortunately, these functional relations are not widely known for the VHF band, and generally it is simply assumed that the $|K|^2$ value is the same as in S band. We chose to try to obtain an expression for the complex refractive index for liquid water as a function of raindrop temperature and VHF wavelength.

Consider the complex refractive index given by [e.g., *Ulaby et al.*, 1986, p. 2018]

$$m = n' - i\, n'' \,; \tag{3.3}$$

$$n' = \mathrm{Re}\left\{\sqrt{\xi}\right\} ; \tag{3.4}$$

$$n'' = \left| \, \mathrm{Im}\left\{\sqrt{\xi}\right\} \right| \,; \tag{3.5}$$

where $i = \sqrt{-1}$, $\xi = \xi' - i\,\xi''$ is the relative dielectric constant (i.e., the ratio between the media dielectric-constant and the dielectric constant of empty space),

ξ' is the relative permittivity (energy storage), and ξ'' is the loss factor (energy lost as heat).

The *Debye* [1929] model describes well the frequency dependence of the dielectric constant for different temperatures. Although this model is limited to radar frequencies below 100 GHz and to scatterers consisting of pure water particles [*Liebe et al.*, 1991], it is sufficient for our purposes (measuring rainfall with 50MHz radars).

The analyses in this section neglect the fact that raindrops are not strictly formed by pure water (i.e., atmospheric aerosols dissolving in raindrops). *Pruppacker and Klett* [1997, p. 715] indicate that concentrations of atmospheric aerosols (mainly salt ions) inside raindrops are in the order of 10^{-4} mole/ liter or smaller. Considering that one mole of pure water weights 18.0 g, and that the density of water in the troposphere is about 1 kg/liter, we then have a concentration of about 56 moles/ liter of pure water. Therefore, the aerosol concentration in raindrops is negligible. Furthermore, no anomalies have been found in the dielectric properties of water in the presence of such small concentrations of salts or organic matter [*Blue*, 1980].

The Debye equations are [e.g., *Ulaby et al.*, 1986, p. 2020]:

$$\xi' = \xi_\infty + \frac{\xi_S - \xi_\infty}{1 + \left(f_R / f_0 \right)^2} ; \tag{3.6}$$

$$\xi'' = \frac{\left(\xi_S - \xi_\infty \right) \left(f_R / f_0 \right)}{1 + \left(f_R / f_0 \right)^2} ; \tag{3.7}$$

where $f_R = 3\times10^8\ m\,s^{-1}/\lambda$ is the frequency of the electromagnetic radiation, ξ_∞ is the high-frequency dielectric constant [when f_R approaches infinite], ξ_S is the static dielectric constant, and f_0 is the relaxation frequency of pure water. Then, from *Liebe et al.* [1991, p. 661, equation (1)] we have

$$\xi_S = 77.66 - 103.3\,\theta_T\ ; \tag{3.8}$$

where

$$\theta_T = 1 - \frac{300}{273.15 + T} \tag{3.9}$$

and T is the temperature in degrees Celsius. Notice that equation (3.8) is valid for a wide span of temperatures; i.e., $-20^\circ C \le T \le 60^\circ C$. [For a more general relationship of ξ_S as a function of T, see *Fernández et al.*, 1997]. From *Liebe et al.* [1991, p. 667, equation (2a)], we also have that

$$\xi_\infty = 0.066\,\xi_S; \tag{3.10}$$

$$f_0 = 20.27 + 146.5\,\theta_T + 314\,\theta_T^{\,2}; \tag{3.11}$$

where f_0 is expressed in units of GHz. Therefore, by combining equations (3.2) to (3.11), we are able to compute the variation of $|K|^2$ with rain temperature and radar frequency, and verify if the assumption of $|K|^2 = 0.93$ is adequate at VHF band.

Figure 3.1 presents the relative dielectric constants for various raindrop temperatures and radar wavelengths. As validation, the upper panel in Figure 3.1 compares the model by *Debye* [1929] and the empirical equations by *Liebe et al.* [1991] with actual measurements in liquid water by *Hippel* [1961] in Table 3.1. The lower panel in Figure 3.1 plots the relative complex permittivity for pure liquid water at temperatures from -15°C to 35°C. Similarly, the upper panel in Figure 3.2 presents the complex refractive index for liquid water at typical tropospheric temperatures. Here, the lower-panel curves in Figure 3.1 are used as input into equations (3.4) and (3.5) to obtain complex refractive indexes (plotted in upper panel of Figure 3.2).

Table 3.1. Measurements of dielectric properties for liquid water at 25°C [from *Hippel*, 1961]. Uncertainties are about ± 2 % in ξ', and about ± 5 % in ξ''/ξ' .

f_R (MHz)	ξ'	$(\xi''/\xi')\times 10^4$
$1.0\text{x}10^8$	78.0	50
$3.0\text{x}10^8$	77.5	160
$3.0\text{x}10^9$	76.7	1570
$1.0\text{x}10^{10}$	55	5400

Refractive index factors for various raindrop temperatures and radar wavelengths are plotted in the lower panel of Figure 3.2. These were computed by using the upper panel curves in Figure 3.2 as inputs into equations (3.3) and (3.2). For these cases, it is clear that $|K|^2$ varies between 0.92 and 0.94 at VHF band. Therefore, in the quantitative analysis of rain using VHF radars, it is also safe (within a 1% or 0.05 dB error) to use the standard weather radar approximation that

$$|K|^2 \cong 0.93 \ . \tag{3.12}$$

However, if the temperature profile above the VHF radar is known (e.g., from radiosonde measurements), then the model described here can provide a more precise value for $|K|^2$.

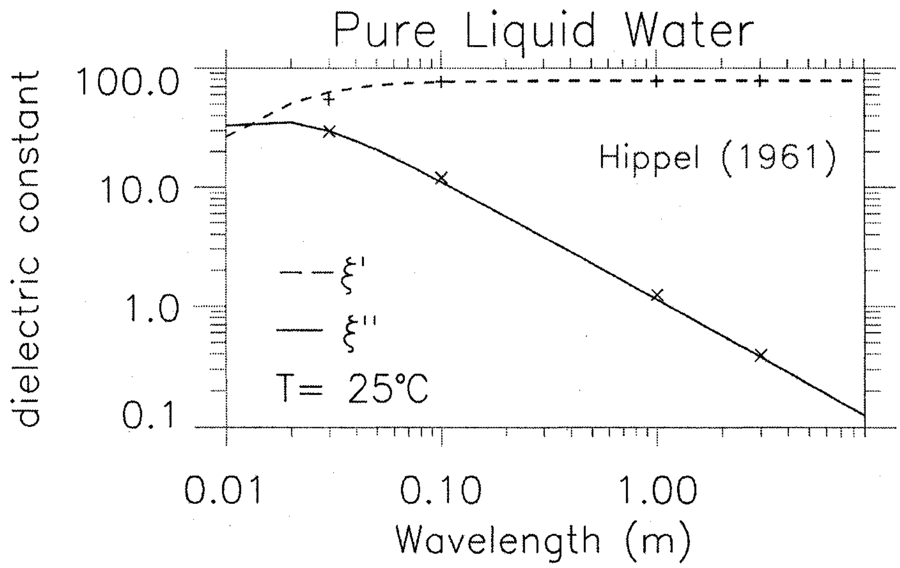

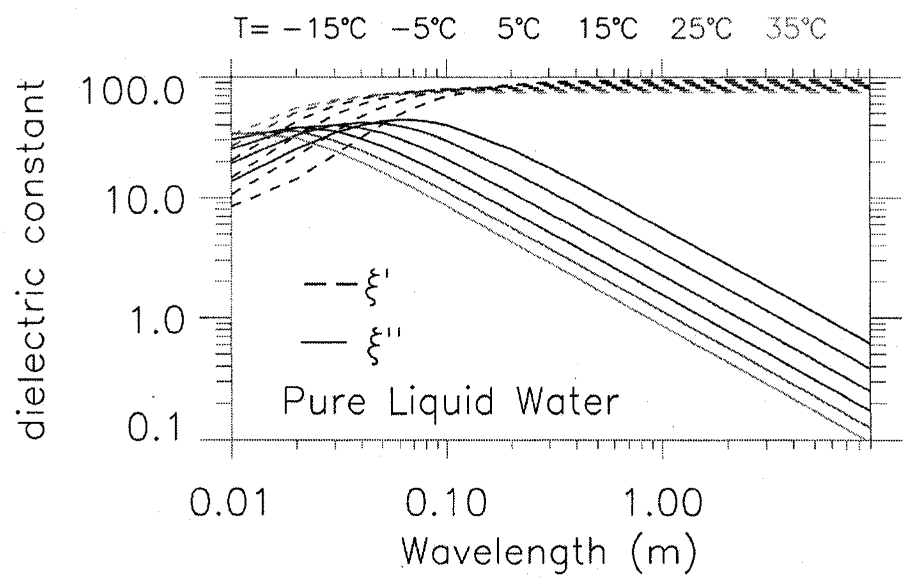

Figure 3.1. Relative dielectric constant for pure liquid water, from the analytical equations by *Debye* [1929] and the empirical equations by *Liebe et al.* [1991]; i.e., equations (3.6) to (3.11). The dashed lines represent the real component, and the solid lines correspond to the imaginary part. The upper panel corresponds to a temperature of 25°C, and the corresponding measurements from Table 3.1 are plotted in red. The lower panel corresponds to the relative complex permittivity at various temperatures.

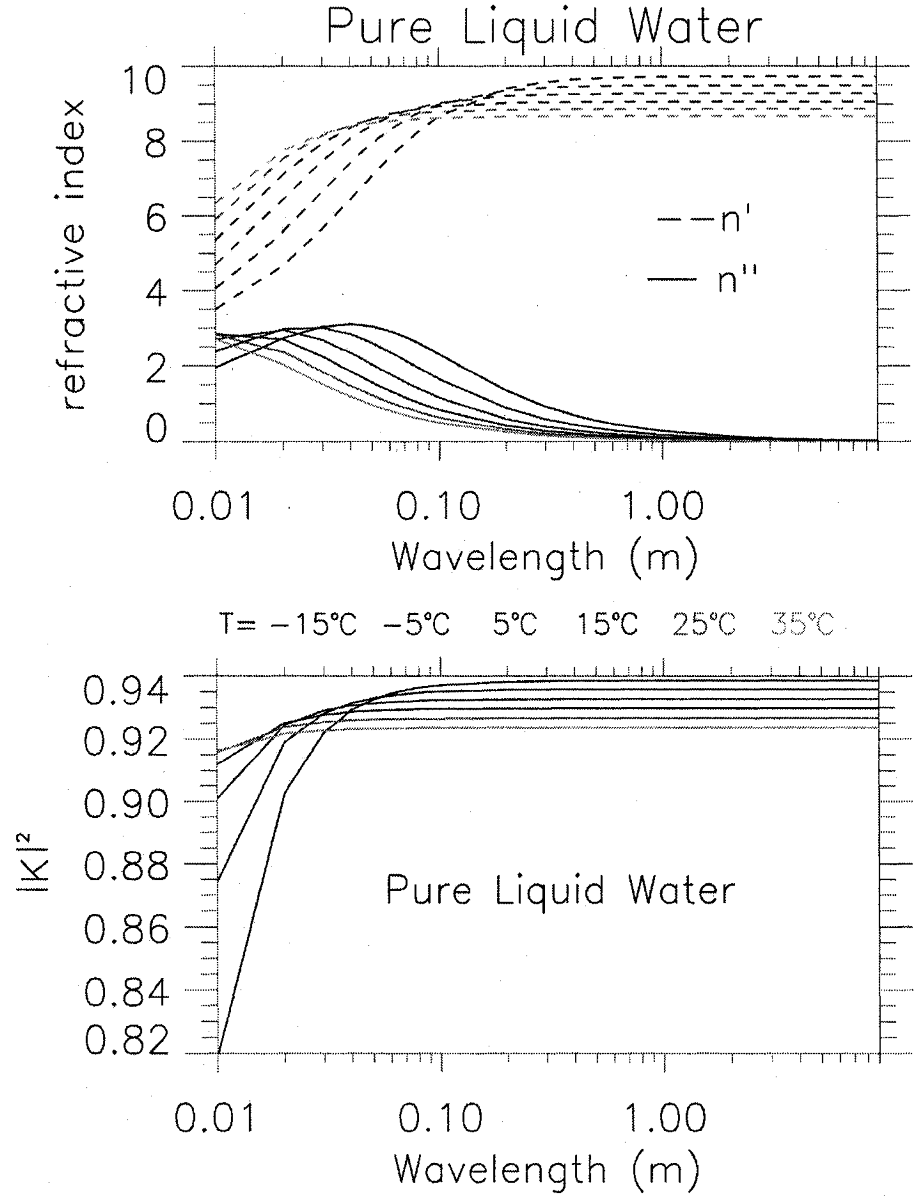

Figure 3.2. Complex refractive indexes (upper panel) and scatterer dielectric factors (lower panel) for pure liquid water at various temperatures and wavelengths. In the upper panel, the dashed lines represent the real component, and the solid lines correspond to the imaginary part. Values computed from the data in Figure 3.1 and equations (3.2) to (3.5).

3.2.2. Deriving a VHF radar equation

In order to accomplish requirement (c), from the Introduction section of this chapter, we start from a general form of the radar equation [i.e., equation (A9), derived in the Appendix]:

$$P_r = \frac{P_{Tx}\, e_T\, (D_{\max})^2\, \lambda^2}{(4\pi)^3} \int_{r=R-L/4}^{R+L/4} \int_{\phi=0}^{2\pi} \int_{\theta=0}^{\pi} \frac{\eta(r,\theta,\phi)\,[F(\theta,\phi)]^2 \sin\theta}{r^2}\, d\theta\, d\phi\, dr\, ; \tag{3.13}$$

where P_r is the backscatter power input into the radar antennas (expressed in Watts), P_{Tx} is the power output by the radar transmitter (in Watts), e_T is the antenna efficiency during transmission, D_{max} is the maximum directivity of the antenna, λ is the radar wavelength (in meters), L is the transmitted pulse length (expressed in units of meters), and $L/2$ is the range resolution. Variables θ, ϕ, and r correspond to the zenith, azimuth, and range (the spherical coordinates), respectively. The range gate is centered at R, and the values R - $L/4$ and R + $L/4$ correspond to the radial boundaries of our range gate (near-range and far-range boundaries, respectively). The radar reflectivity η is expressed in m^{-1}. F is the normalized, one-way polar-diagram of the radar antenna. We have assumed a square transmitted pulse although in reality this can be untrue (see the Appendix).

In order to solve equation (3.13), the main challenge is within the multivariate integral, since the coefficients outside this integral are simply hardware constants (that will be derived in the following sections). Therefore, let us focus on this multivariate integral. It is common practice to assume that the spatial variability of η is negligible within a one-gate sampling volume; i.e.,

$$\eta(r,\theta,\phi) = const.; \tag{3.14}$$

if θ and ϕ are in the main lobe of the polar diagram, and if $r \in \left[R - \frac{L}{4}, R + \frac{L}{4}\right]$.

Therefore, we obtain from equations (3.13) and (3.14) that

$$P_r = \frac{P_{Tx}\, e_T\, (D_{\max})^2\, \lambda^2\, \overline{\eta}}{(4\pi)^3} \int_{\phi=0}^{2\pi} \left\{ \int_{\theta=0}^{\pi} [F(\theta,\phi)]^2 \sin\theta \left[\int_{r=R-L/4}^{R+L/4} \frac{dr}{r^2} \right] d\theta \right\} d\phi. \tag{3.15}$$

The square-brackets integral in equation (3.15) is easy to obtain:

$$I_0 = \int_{r=R-L/4}^{R+L/4} \frac{dr}{r^2} = \frac{-1}{R+L/4} + \frac{1}{R-L/4} = \frac{L/2}{R^2-(L/4)^2}. \tag{3.16}$$

Therefore, we only have to deal with the expression

$$I = \int_{\phi=0}^{2\pi} \int_{\theta=0}^{\pi} F^2(\phi,\theta) \sin\theta \, d\theta \, d\phi; \tag{3.17}$$

such that

$$P_r = \frac{P_{Tx}\, e_T\, (D_{\max})^2\, \lambda^2\, \overline{\eta}}{(4\pi)^3} \left[\frac{L/2}{R^2-(L/4)^2} \right] I. \tag{3.18}$$

Let us now focus on solving integral I, and particularly on the antenna pattern F. In the following section, two approaches are presented for solving equation (3.17).

3.2.2.1. Analytical derivation (from Gaussian lobe)

Assume that F is a Gaussian lobe; i.e.:

$$F(\theta,\phi) \approx \exp\left(\frac{-\theta^2}{2\gamma^2}\right) \quad ; \quad \gamma^2 = \frac{\theta_0^{\,2}}{2 \ln 2} \quad ; \tag{3.19}$$

where θ_0 is the one-way half-power half-beamwidth. Therefore, by combining equations (3.17) and (3.19), we have that

$$I = \int_{\theta=0}^{\pi} \exp\left(\frac{-\theta^2}{\gamma^2}\right) \sin\theta \left[\int_{\phi=0}^{2\pi} d\phi\right] d\theta = 2\pi \int_{\theta=0}^{\pi} \exp\left(\frac{-\theta^2}{\gamma^2}\right) \sin\theta \, d\theta . \tag{3.20}$$

However, we know that

$$\sin\theta \cong \theta \quad ; if\ \theta \leq 10° . \tag{3.21}$$

Therefore,

$$\int_{\theta=0}^{\pi} \exp\left(\frac{-\theta^2}{\gamma^2}\right) \sin\theta \, d\theta \cong \int_{\theta=0}^{\pi} \exp\left(\frac{-\theta^2}{\gamma^2}\right) \theta \, d\theta . \tag{3.22}$$

Equation (3.22) is verified in Figure 3.3, where the numerical computation of the right and left sides of equation (3.22) confirm the agreement within 10^{-6} units. Given the shape of F in Figure 3.3 (small dynamic range in θ), it is also safe to assume that the spatial variability of η is negligible within the sampling volume. Therefore, we verify equation (3.14) as well.

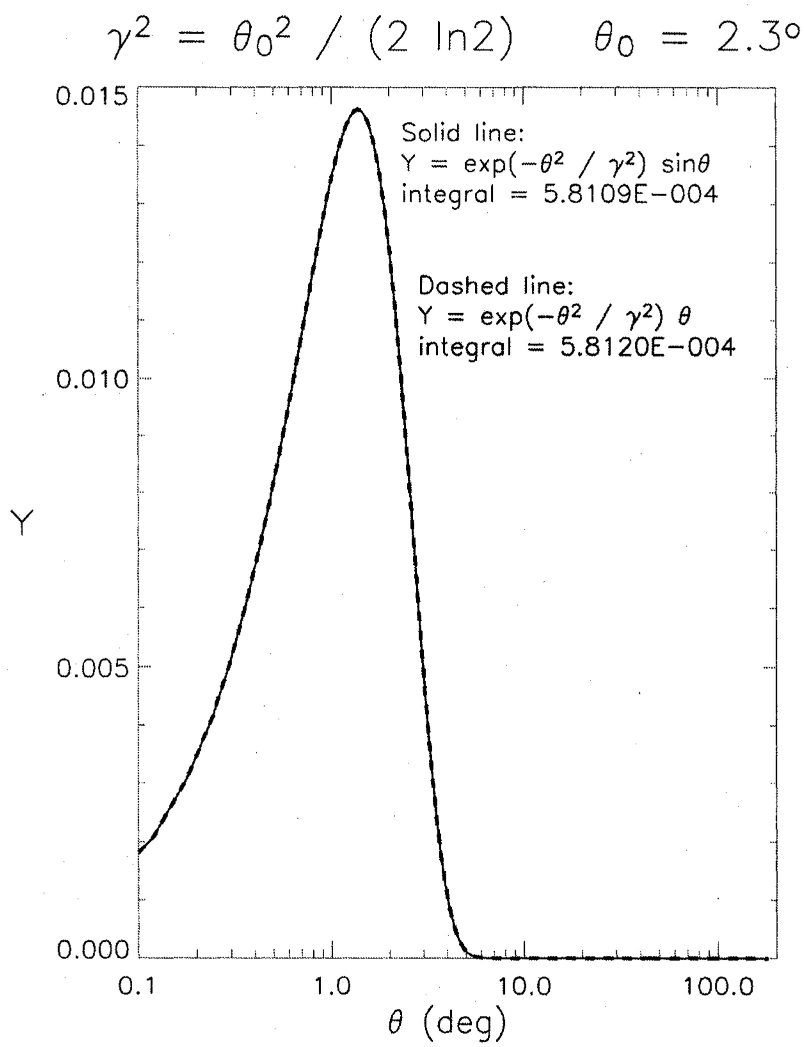

Figure 3.3. Gaussian approximation of F, for $\theta_0 = 2.3°$. The solid curve corresponds to the expression inside the right side integral in equation (3.22). The dashed line (on top of the previous curve) corresponds to the expression inside the left side integral in equation (3.22).

With these assumptions, equation (3.20) can take the following shape:

$$I = 2\pi \int_{\theta=0}^{\pi} \exp\left(\frac{-\theta^2}{\gamma^2}\right) \theta \, d\theta . \tag{3.23}$$

We can now solve the integral in equation (3.23) by substitution, with

$$u = \frac{-\theta^2}{\gamma^2} \quad \Rightarrow \quad du = \frac{-2\,\theta\, d\theta}{\gamma^2} \quad \Rightarrow$$

$$\int_{\theta=0}^{\pi} \exp\left(\frac{-\theta^2}{\gamma^2}\right) \theta\, d\theta = \int_{u_i}^{u_f} e^u \left(\frac{-\gamma^2}{2}\, du\right) = \frac{-\gamma^2}{2}\left[\exp\left(\frac{-\pi^2}{\gamma^2}\right) - \exp(0)\right]. \tag{3.24}$$

However

$$\gamma^2 = \frac{\theta_0^{\,2}}{2\ln 2} \quad \Rightarrow$$

$$\int_{\theta=0}^{\pi} \exp\left(\frac{-\theta^2}{\gamma^2}\right) \theta\, d\theta = \frac{-\theta_0^{\,2}}{4\ln 2}\left[\exp\left(\frac{-\pi^2\, 2\ln 2}{\theta_0^{\,2}}\right) - 1\right]. \tag{3.25}$$

From equations (3.18), (3.23), and (3.25) we obtain

$$P_r = \frac{P_{Tx}\, e_T\, (D_{\max})^2\, \lambda^2\, \overline{\eta}\, \theta_0^{\,2}}{256\pi^2 \ln 2}\left[\frac{L}{R^2 - (L/4)^2}\right]\left[1 - \exp\left(\frac{-\pi^2\, 2\ln 2}{\theta_0^{\,2}}\right)\right]. \tag{3.26}$$

Moreover,

$$\exp\left(\frac{-\pi^2\, 2\ln 2}{\theta_0^{\,2}}\right) << 1 \quad if \quad \frac{\pi^2\, 2\ln 2}{\theta_0^{\,2}} >> 1 \tag{3.27}$$

$\Rightarrow \pi^2\, 2\ln 2 >> \theta_0^{\,2} \Rightarrow \theta_0 << 3.70\ radians = 212°$; which is valid all the time.

Therefore, the radar equation will be given by

$$P_r = \frac{P_{Tx}\, e_T\, (D_{\max})^2\, \lambda^2\, \overline{\eta}\, L\, \theta_0^{\,2}}{256\pi^2 \ln 2\, [R^2 - (L/4)^2]}. \tag{3.28}$$

Notice that equation (3.28) is equivalent to other earlier radar equations [e.g., *Hocking*, 1985, equation 33a; *Probert-Jones*, 1962, equation 3]. In general, traditional radar equations do not deal with the power input into the antennas during reception, P_r, but with the power detected at the receiver (i.e., $e_R\, P_r$, where

e_R is the antenna efficiency during reception). For our analysis, we consider e_R during the calibration stage, which is described in Chapter 2. Taking this into account, equation (3.28) will differ from more traditional expressions only at the factor $[R^2 - (L/4)^2]$. This factor comes from integral I_0 in equation (3.16). Traditional radar equations generally assume that the radar range resolution is much smaller than the range of the sampling volume, and therefore

$$R^2 >> (L/4)^2 \quad \Rightarrow \quad I_0 \approx \frac{L}{2\,R^2}. \tag{3.29}$$

Equation (3.29) is inaccurate for VHF radars when the ranges are comparable to the transmitted pulse lengths. Equation (3.28) is therefore a more general radar equation than the ones previously published in the literature.

3.2.2.2. Numerical derivation (from antenna polar diagram)

It should be noted that the assumption in equation (3.19) is just an approximation that does not consider sidelobes in the antenna pattern nor the pulse shape. However, if somehow we know the antenna polar diagram valid for a particular radar of interest, we then can solve equation (3.17) numerically. As an example, we present the case of F that is valid for the McGill VHF radar (given in Figure 3.4). This antenna pattern was provided by *Mardoc Inc.* [2002], the company manufacturing this radar system, and it was obtained from accurate numerical computations of the antenna-array response to an input power. Notice that here

$$F(\phi,\theta) = 0 \quad at \quad \theta \geq 90^\circ. \tag{3.30}$$

The most relevant details in the structure of F can be observed from Figure 3.5, which indicates that the one-way half-power half-beamwidth for this radar is 2.3 degrees.

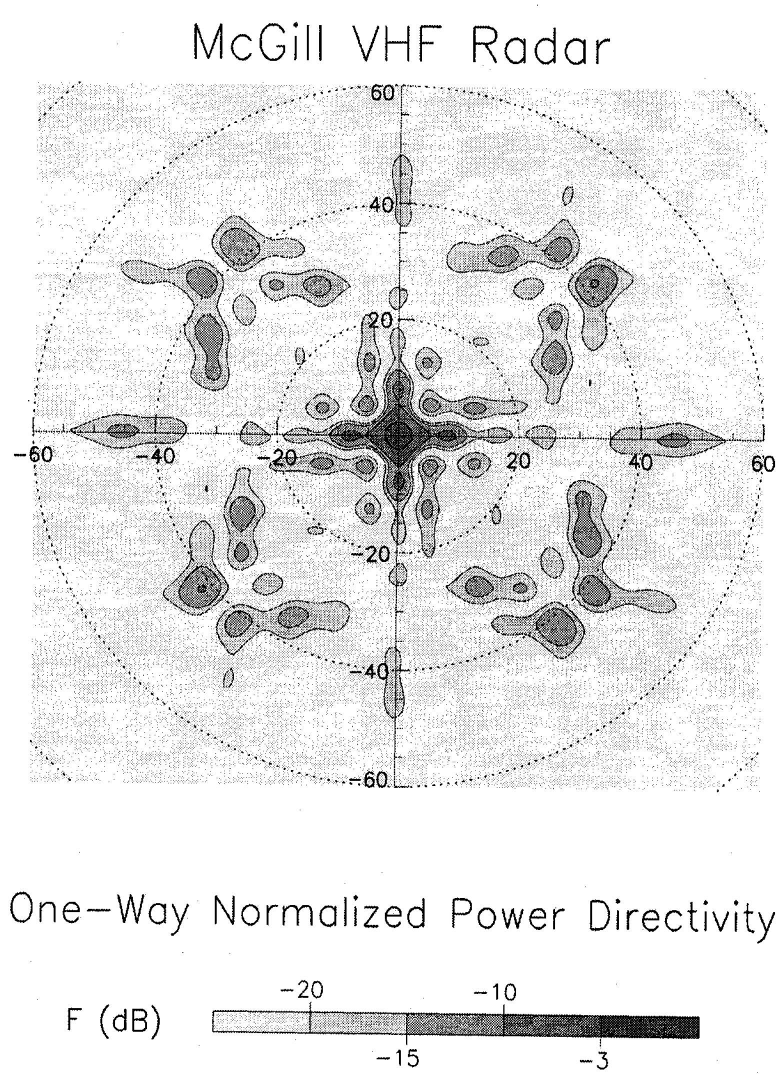

Figure 3.4. One-way antenna pattern (also known as polar diagram, *F*) for the McGill VHF radar. The concentric circles correspond to the zenith angles in the X and Y axis. The azimuth angles start clockwise from the positive Y axis. The geographic North is located at 48.7° azimuth.

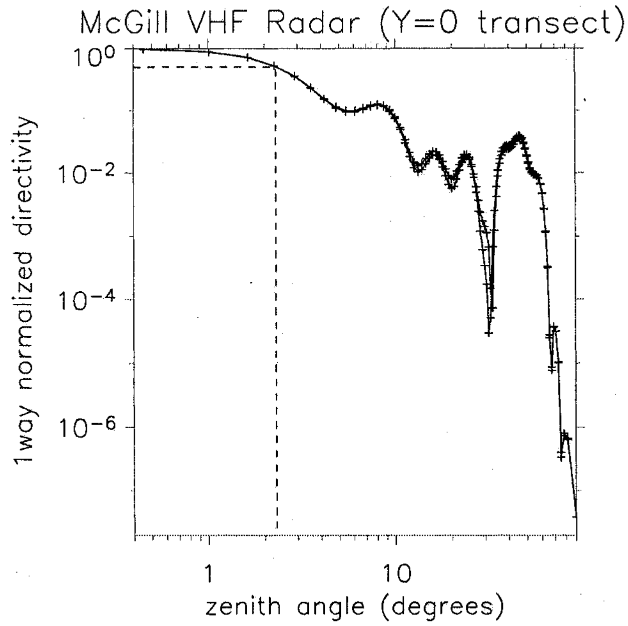

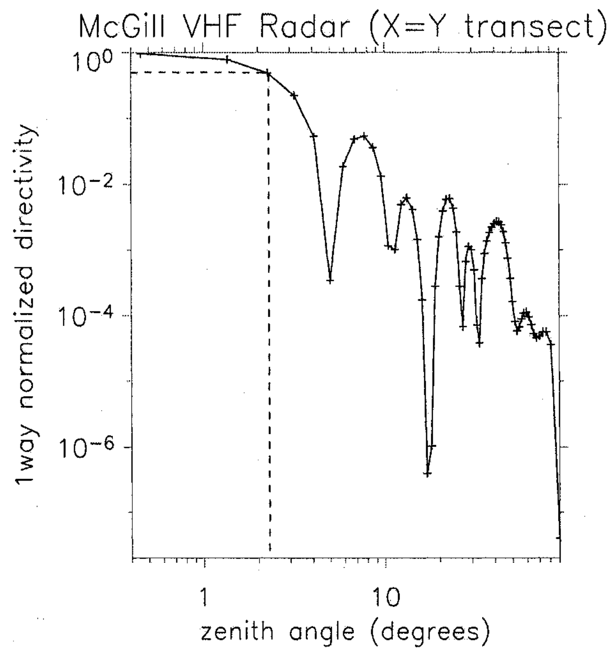

Figure 3.5. Cross section of the one-way antenna pattern. Upper: Transect in Figure 3.4 along the X-axis, at the Y-axis equal to zero. Lower: Transect in Figure 3.4 along the diagonal where the X-axis is equal to the Y-axis. The one-way half-power half-beamwidth (at 2.3° zenith angle) is indicated by dashed lines.

Solving equation (3.17) by using the antenna pattern in Figure 3.4 implies dealing with the integrand expression $[F(\phi,\theta)]^2 \sin\theta$. Figure 3.6 plots (in solid lines) cross sections for this expression, similar to the ones in Figure 3.5. For comparison, the corresponding curves for F being a Gaussian lobe (as in section 3.2.2.1) are also plotted (in dashed lines). The main lobe of ($F^2 \sin\theta$) lies at zenith angles between zero and five degrees. As well, the main differences between the Gaussian lobe approximation and the computed antenna pattern are located only within the sidelobes (i.e., θ between 5° and 90°). The numerical computation of integral I (in steradians) gives as a result

$$I = \int_{\phi=0}^{2\pi} \int_{\theta=0}^{\pi} [F(\phi,\theta)]^2 \sin\theta \, d\theta \, d\phi = \int_{\phi=0}^{2\pi} \int_{\theta=0}^{\pi/2} [F(\phi,\theta)]^2 \sin\theta \, d\theta \, d\phi = 4.32313 \times 10^{-3}, \tag{3.31}$$

with an uncertainty of 10^{-8} steradians (i.e., 10^{-8} is the only digit that will vary if the computation resolution is increased). Note that the analytical expression for I, derived from equations (3.19) to (3.25) in section 3.2.2.1, for our case in which $\theta_0 = 2.3°$, gives (also in steradians)

$$I = \int_{\phi=0}^{2\pi} \int_{\theta=0}^{\pi} [F(\phi,\theta)]^2 \sin\theta \, d\theta \, d\phi = 3.65178 \times 10^{-3}. \tag{3.32}$$

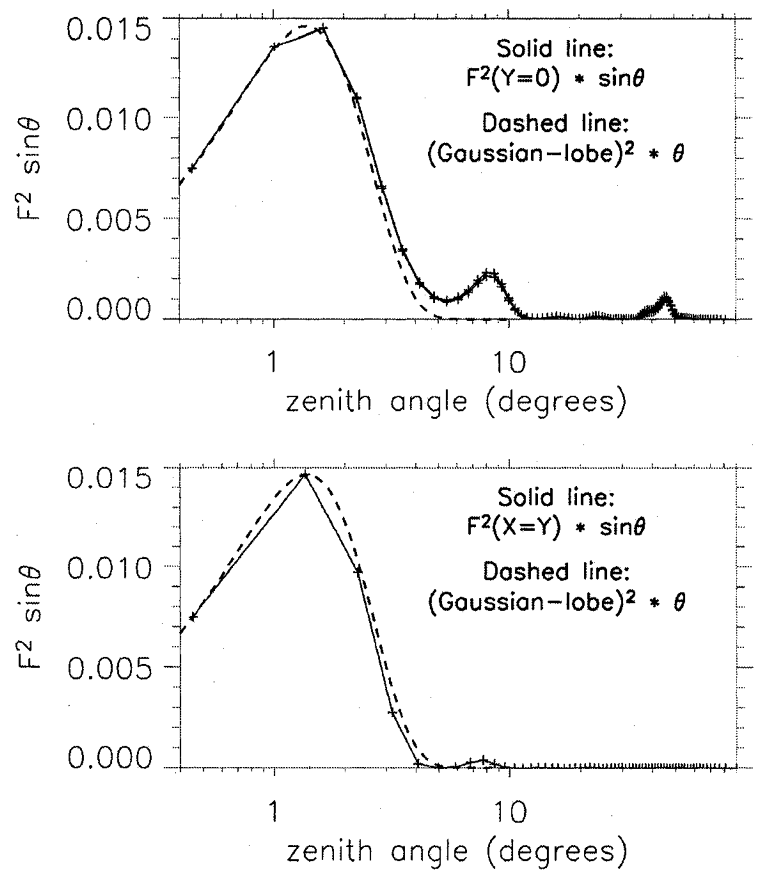

Figure 3.6. Cross section of the integrand expression $F^2 \sin\theta$. The continuous lines use the one-way antenna patterns in Figures 3.5, and the dashed lines correspond to the Gaussian antenna pattern in Figure 3.3.

Therefore, from equations (3.18) and (3.31), the radar equation for our system is given by

$$P_r = \frac{P_{Tx}\, e_T\, (D_{\max})^2\, \lambda^2\, \overline{\eta}}{(4\pi)^3} \left[\frac{L/2}{R^2 - (L/4)^2} \right] 4.3\times 10^{-3} . \tag{3.33}$$

Notice that equation (3.33) applies only to range gates within the antenna far-field region (also known as the Fraunhofer region [e.g., *Ulaby et al.*, 1981, p. 117-121]). For the McGill VHF radar, the far field would begin at around 1.7 km range. At ranges smaller than the far-field range, the antenna polar diagram in Figure 3.4 is not longer valid.

There are other hardware factors that, although they do not invalidate equation (3.33), can affect our ability to interpret P_r (i.e., the power received at the antennas) from the power output by the radar signal processing, P_{out}. The most important one is the recovery times of the radar receiver (after being hit by the transmitter pulse). In the McGill VHF radar, this effect manifests as an abrupt decrease in the power intensities as we descend in range. We have noticed this effect at the 2.0 km gate and below. For example, systematic power differences between the 2.0 km and the 2.5 km gates (the second gate not being affected by these hardware factors) are already on the order of 9 dB. We have then performed our precipitation analysis only at range gates above 2 km.

There are a few other antenna parameters that depend on F and that are worth obtaining. We compute them numerically as follows. The solid angle of the one-way main-lobe, which describes the effective width of this main lobe, is given in steradians by

$$\Omega_M = \int_{\phi=0}^{360^\circ} \int_{\theta=0}^{5^\circ} F(\phi,\theta)\sin\theta \, d\theta \, d\phi = 6.9763650 \times 10^{-3}. \tag{3.34}$$

Notice that the 5° integration limit (in the zenith angle) comes from Figure 3.6, which indicates that the main lobe can be located at θ between 0 and 5 degrees. Also note that we would obtain $\Omega_M = 6.446 \times 10^{-3}$, if we would have used the approximation that the solid angle of a single-lobe radiation-pattern is equal to the square of the half-power beamwidth [*Ulaby et al.*, 1981, p. 102]. The solid angle of the one-way full-antenna-pattern is given in steradians by

$$\Omega_p = \int_{\phi=0}^{360^\circ}\int_{\theta=0}^{180^\circ} F(\phi,\theta)\sin\theta\, d\theta\, d\phi = \int_{\phi=0}^{360^\circ}\int_{\theta=0}^{90^\circ} F(\phi,\theta)\sin\theta\, d\theta\, d\phi = 2.7503684\times 10^{-2}. \tag{3.35}$$

The maximum directivity is given by [e.g., *Ulaby et al.*, 1981, p.102, equation 3.21]

$$D_{\max} = \frac{4\pi}{\Omega_p} = 456.89773. \tag{3.36}$$

Finally, the two-way main-lobe solid-angle is given (in steradians) by

$$I_M = \int_{\phi=0}^{360^\circ}\int_{\theta=0}^{5^\circ} [F(\phi,\theta)]^2 \sin\theta\, d\theta\, d\phi = 3.6692806\times 10^{-3}; \tag{3.37}$$

which using equation (3.31) implies that about 85% of the radar signal is transmitted and received from the two-way main-lobe; i.e.,

$$\frac{I_M}{I} = 0.84875. \tag{3.38}$$

3.2.3. Extracting the rain signal from VHF power spectra

Concerning requirement (b), from the Introduction section of this chapter, we should notice that the automatic separation of the rain signal from the total VHF received power represents an interesting challenge in terms of radar signal processing. On the one hand, Doppler spectra measured by VHF radar during rain events present clearly separated modes. One mode corresponds to the clear air signal (the slowest) and the other to rain signal (the fastest). Since ground clutter has to be previously removed, we use both a signal-processing software for ground-clutter filtering [*Hocking*, 1997] and a radar antenna layout particularly designed for good ground-clutter suppression (larger than 100 dB in two-way mode). One spectrum example is presented in Figure 3.7, which corresponds to observations by the McGill VHF radar at a range gate centered at 2.5 km height (i.e., the gate between 2.25 and 2.75 km above the ground level). This spectrum has a population of scatterers peaking at -3.5 Hz (i.e., a Doppler velocity of about -10 m/s, typical magnitude for raindrop fall velocities), and a slower population peaking at – 0.05 Hz (i.e., a Doppler velocity of -0.14 m/s, a weak downdraft). We have noticed that, at rainrates of about 4 mm/h or higher, it is not rare to observe rain spectral peaks being as strong as (or even stronger than) the clear air peak. On the other hand, part of the clear air signal often overlaps within the rain spectral range.

To deal with this challenge, we developed a method for extracting the rain signal out of the total Doppler power spectra that is valid for any vertically-pointing VHF radar. This method has been developed from an empirical basis, and it is described as follows. Our method starts with the raw spectra measured by the VHF radar (i.e., non-calibrated spectra, expressed in receiver arbitrary units per spectral bin, au/Hz). For a given range gate, a spectrum is obtained every 35 seconds, for a spectral range within -10.0 and 10.0 Hz, and a spectral bin resolution of 0.067 Hz. The ground clutter signal has already been removed by a notch filter near 0 Hz [see *Hocking*, 1997, for details on the Doppler power spectra derivation].

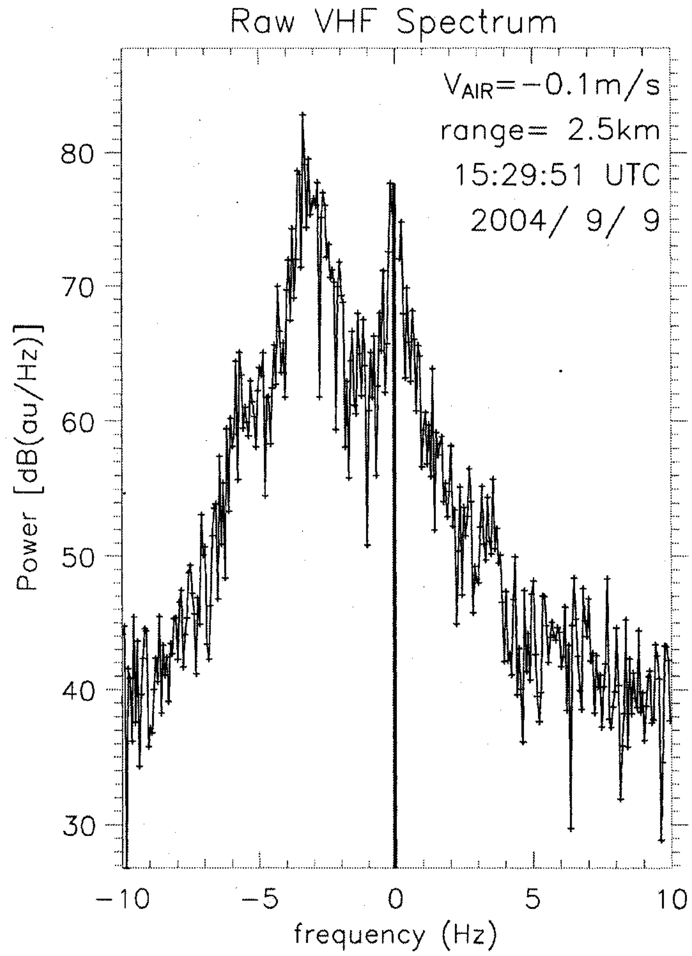

Figure 3.7. Doppler power spectrum observed in rain by the McGill VHF radar (over Montreal). For this example, on September 9, 2004, at 15:29:51 UTC, the beam points vertically and the range gate centers at 2.5 km. The vertical line (near zero Hz) represents the frequency bin where our method has found the peak in the clear-air spectral. This spectral peak corresponds to a downward vertical velocity of 0.1 m/s.

The second step consists in finding the clear-air spectral peak. To do this, we search for the four largest power density values located in the spectral range between -3 and 10 m/s. Notice that these vertical Doppler velocities correspond (in our radar) to Doppler frequencies between -1.0 and 3.45 Hz. After observing several thousands of power spectra taken by the McGill VHF radar, we have determined that the clear-air peak is generally located within these Doppler velocities. If the four largest power densities are spaced at velocity intervals larger than 1.5 m/s (for our radar, frequency intervals larger than 0.5 Hz), then we stop the procedure and conclude that no clear-air signal can be retrieved. Otherwise, we compute the average frequency for these points, and the frequency bin for the clear-air peak, f_j, will be the one closer to this average frequency. For the McGill VHF radar, approaching targets will correspond to negative frequencies (and downward, negative Doppler velocities). The vertical line in Figure 3.7 (near zero Hz) indicates the clear-air peak obtained for this particular case (i.e., -0.1 m/s).

During the third step, we subtract the clear air signal from the recorded Doppler power spectrum, and the remaining spectrum will then be the one corresponding to precipitation. We assume that the clear-air spectrum is symmetrically distributed around its peak. Therefore, the clear-air signal at n spectral bins to the right of the clear-air peak should be the same (on average) as at n spectral bins to the left of the clear-air peak. In the recorded Doppler spectrum, we will not expect to have precipitation signal to the right of the clear-air peak. Precipitation signal will be present only to the left of the clear-air peak, since (for the vertical-beam direction) precipitation Doppler velocities are always more negative than clear-air Doppler velocities. Therefore, it is safe to assume that the rain power density is given by

$$S_{precip}(f_{j-i}) = S(f_{j-i}) - S(f_{j+i}) ; \qquad (3.39)$$

where $S_{precip}(f_n)$ is the Doppler power density of precipitation at the n-th spectral bin (in Watts per Hz), $S(f_n)$ is the Doppler power density of recorded spectrum at the n-th spectral bin (in Watts per Hz), j is the spectral bin corresponding to the clear-air peak, and i is any given spectral bin.

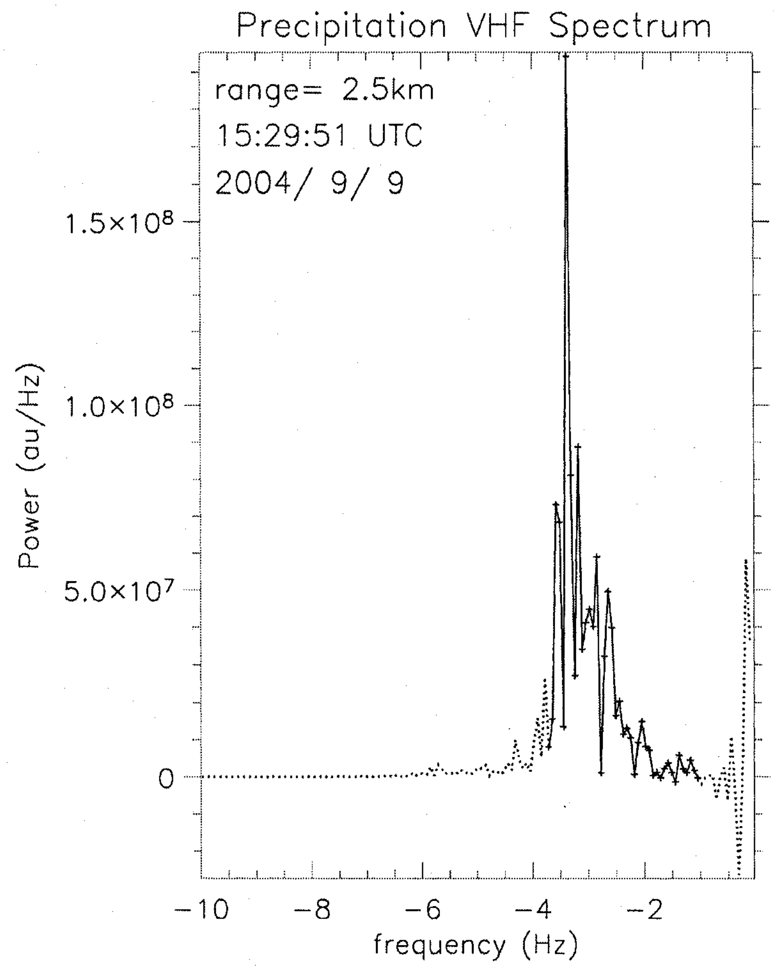

Figure 3.8. Precipitation spectrum (solid line) extracted from the Doppler power spectrum in Figure 3.7 and equation (3.39). The dotted line to the right of the solid line corresponds to the spectral region located within (f_j - 1 Hz) and f_j ; where f_j is the frequency bin for the clear-air peak. The dotted line to the left of the solid line corresponds to the spectral region where Doppler frequencies are smaller than a threshold value f_{min}. The value of f_{min} is defined by Figure 3.9.

Figure 3.8 presents the result of applying equation (3.39) to the Doppler power spectrum in Figure 3.7. From multiple observations of the performance of this method with real data, we have estimated that the largest Doppler frequency that we can retrieve in the rain spectrum is located at 1.0 Hz to the left of the clear-air peak. Therefore,

$$f_{\min} \leq f_{precip} \leq (f_j - 1.0)\,Hz\,; \tag{3.40}$$

where f_{precip} corresponds to all Doppler frequencies in the retrieved precipitation spectrum, and $f_{\min}$ is the smallest Doppler frequency of this precipitation spectrum. Notice that $f_{\min}$ corresponds to the Doppler velocity of the largest precipitation particle. We assume that this Doppler velocity (v) matches the terminal velocity of a 5.8 mm raindrop [i.e., the largest raindrop measured by *Gunn and Kinzer,* 1949, which already corresponds to a giant raindrop, and which is very unlikely to occur], falling in a standard atmosphere [*ICAO*, 1993] according to the altitude adjustment by *Beard* [1985]; i.e.,

$$v = v_T = v_0 \left(\frac{\rho_0}{\rho}\right)^m \quad ; \tag{3.41}$$

$$m(D_e) = 0.375 + 0.025\,D_e\,; \tag{3.42}$$

where v_T is the terminal fall velocity (in m/s) for a raindrop of diameter D_e (in mm) at any given height, v_0 is the terminal fall velocity (in m/s) of that drop at sea level, ρ is the air density (in kg m^{-3}) around the falling raindrop at the given height, and ρ_0 is the air density at sea level (in kg m^{-3}). For the change of air density with height, we use the values of the ICAO standard atmosphere [*ICAO*, 1993]. The terminal velocity of this hypothetical, largest raindrop is given in Figure 3.9, and the computation for this figure uses D_e = 5.8 mm, v_0 = 9.17 m/s [from Gunn and Kinzer, 1949], and ρ_0 = 1.225 kg m^{-3} [from *ICAO*, 1993]. Therefore, the smallest Doppler frequency of precipitation ($f_{\min}$) depends on the height of the radar range gate, according to the upper X-axis in Figure 3.9. For reference, the spectral regions located within $-10.0\ Hz \leq f < f_{\min}$, and within $(f_j - 1.0\ Hz) \leq f < f_j$, are plotted as dotted lines in Figure 3.8. We eliminated these regions from the precipitation spectra since they still contain some remnants of non-precipitation signal.

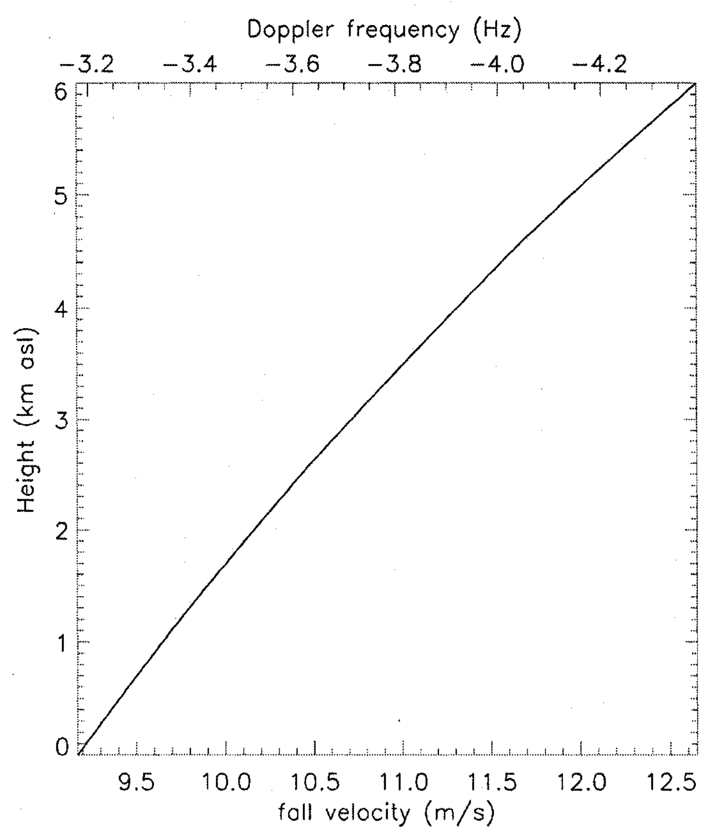

Figure 3.9. A raindrop of 5.8 mm diameter falling at terminal velocity in an ICAO Standard atmosphere. The fall velocity at zero km height corresponds to observations by *Gunn and Kinzer* [1949]. The upper X-axis defines the value of $f_{\min}$ to be used in equation (3.40). For example, the range gate at 2.5 km height corresponds to $f_{\min} = -3.61$ Hz.

In the last step, we integrate the precipitation power densities S_{precip} over the Doppler spectral range in equation (3.40). As a result, we are finally able to express the VHF integrated precipitation signal. Notice that the input VHF spectrum, $S(f_n)$, can be expressed in any signal-strength units (e.g., power in arbitrary units or Watts, reflectivity in m^{-1}, or reflectivity factor in $mm^6\ m^{-3}$) per frequency bin (i.e., Hz).

3.2.4. Calibrating the VHF spectra

To deal with the requirement (a), from the Introduction section of this chapter, we calibrated the VHF power-density spectra using the method described in Chapter 2; i.e.,

$$P_{cal} = P_{out}\ B_{sky} + A_{sky}\ ; \tag{3.43}$$

where the subscript *out* correspond to the radar raw output (expressed in the arbitrary units of the analog-to-digital converter, in the radar receiver), the subscript *cal* corresponds to the calibrated power (expressed in Watts), and the subscript *sky* corresponds to the values derived from a sky-noise calibration. Therefore, the calibration equation of power densities (S) for the i-th spectral bin is given by [Chapter 2, equation (2.24)]

$$S_{cal}(f_i) = \left[\frac{A_{sky}}{f_{sampling}} + B_{sky}\ S'_{out}(f_i) \right] \frac{1}{N_{coh}}; \tag{3.44}$$

where $S_{cal}(f_i)$ is the calibrated spectral density (in Watts) at the Doppler frequency bin f_i, $S'_{out}(f_i)$ is the measured spectral density (in arbitrary units) at f_i, and N_{coh} is the number of coherent averages. Notice that the sampling frequency, $f_{sampling}$ = $(PRF\ /\ N_{coh})$, is used here for correcting the fact that not all the Doppler spectral range has being stored during signal processing (only spectral densities within ±

10 Hz are being kept). Table 3.2 provides the values we use for the constant terms in equation (3.44).

Table 3.2. Parameters of the McGill VHF Radar.

Parameter	Value
Transmitted wavelength (λ)	5.77 m
Peak transmitted power (P_{Tx})	40 kW
Antenna efficiency (e_T)	0.631
Transmitted pulse length (L)	1 km
Pulse repetition frequency (PRF)	6 kHz
Number of coherent averages (N_{coh})	16
First calibration coefficient (A_{sky})	$-1.797x10^{-14}$ W
Second calibration coefficient (B_{sky})	$2.095x10^{-20}$ W/au

3.2.5. Validating our rain measurements

In order to measure rainfall reflectivity factors, using only observations from a VHF radar, we first extracted VHF rain signals (expressed as power P_r, in Watts) applying the method already described in section 3.2.3. Then we combined equations (3.1) and (3.33) in order to express the rain signal as reflectivity factor Z. For this procedure, the values in Table 3.2 were used. In addition, we required that the VHF radar measurements be taken during an event of widespread precipitation, having a melting level much higher than the lowest range gate of our radar. These requirements provided a sufficiently large dataset of rain measurements at least at the very first range gate. We prefer to focus on rain measurements (instead of any other precipitation particles) because this will avoid the inconvenience of not knowing the exact $|K|^2$ value for solid or melting particles. Measured equivalent reflectivity factors Z_e are then simply equal to theoretical reflectivity factors Z [from equation (3.1)]. As well, rain signals are easier to separate (from clear-air signals) than snow signals. For our radar dataset, the lowest range gate is between 2.25 and 2.75 km height. It is not often that wide-spread precipitation over Montreal presents bright bands above these heights. However, we managed to collect VHF data during several precipitation events (more than 23 hours of rainfall) that fulfill these requirements.

Co-located with the McGill VHF radar, we operated a Precipitation Occurrence Sensor System [POSS, described by *Sheppard*, 1990] for these precipitation events. POSS is a bistatic, X-band (10.5 GHz frequency, 2.85 cm wavelength), continuous-wave, Doppler radar. This sensor points upward and detects precipitation particles in its sampling volume, which is located only a few centimetres above the instrument. [See *Campos*, 1998, for details on POSS calibration, precision and validation history.] The POSS allowed us the measurement of raindrop-size distributions at the ground, and from these, the radar reflectivity factor was computed by using [e.g., *Rogers and Yau*, 1989, p.190, equation 11.7]

$$Z = \int_0^\infty D_e^{\,6} \, N(D_e) \, dD_e \; ; \tag{3.45}$$

where Z is given in mm^6 m^{-3}, $N(D_e)$ is the raindrop-size distribution (in mm^{-1}m^{-3}), and D_e is the equivalent-spherical raindrop-diameter (in mm). The Z values obtained from drop sizes at ground were corrected to consider the atmospheric conditions at 2.5 km height, and then compared to the VHF reflectivity factors obtained aloft. This comparison method resembles the calibration work by Gage et al. [2000, section 4], and its outcome is presented in section 3.3.2.

3.3. Results

3.3.1. Expressing VHF rain signal as reflectivity factor

VHF power-density spectra (expressed in arbitrary units, au), were selected for a precipitation event occurring on September 9, 2004. This day corresponded to the passage of the remnants of hurricane Frances over the radar site. We selected the range gate located between 2.25 and 2.75 km height. A new power spectrum was obtained every 35 seconds. Considering the transmitted pulse length and the two-way half-power half-beamwidth of the VHF radar (i.e., 500m and 1.6°, respectively), these observations are representative of a sampling volume (per unit time) in the order of 2.3×10^5 m^3 s^{-1}.

We first calibrated the raw VHF spectra (in au/Hz) by using equation (3.44) and Table 3.2. Then, for each particular calibrated spectrum (in W/Hz), we subtracted the noise to the total spectral densities. It is important that we subtract the noise at each calibrated power spectrum, since the next step is to combine spectra taken at different times (for smoothing), and these spectra may not share the same noise. The noise level is estimated here by computing the median spectral power densities in the outer 1Hz of the spectrum at each end (i.e., near -10 and 10 Hz) and then using the minimum value of these two estimates. Notice that this method for noise estimation is a modification of the method by *Hocking* [1997], where he uses the mean of the outer spectral densities instead of the median. We prefer to use the median because it is much less affected by extreme power-density values, which would be artifacts generated by non-meteorological targets.

At this point, the calibrated noise-subtracted VHF-spectra (now a signal expressed in W/Hz) were time smoothed by computing (for each spectral bin) the median value within a 10-minute moving window. The reason for applying this smoothing is to homogenize the volume representativeness of the VHF and POSS observations.

We then obtain average reflectivity densities (in m^{-1}/Hz) in the following stage. After calibration, noise subtraction, and smoothing of the power densities, we substituted in equation (3.33) the input values of P_r by the power density at each spectral bin. We also replaced the output values of $\overline{\eta}$ [also in equation (3.33)] with the average reflectivity density (in m^{-1}/Hz) at each spectral bin. After this, we multiplied the average reflectivity densities by $2/\lambda$ in order to express these spectra in units of reflectivity per Doppler velocity bin [i.e., m^{-1}/ (m s^{-1})].

For each spectral bin, the average reflectivity density [in m^{-1}/ (m s^{-1})] was input as a substitute for η_{precip} into equation (3.1). As a result, we obtained VHF Doppler spectra of the reflectivity factor (i.e., the clear-air plus precipitation spectra, valid for the entire spectral range). From these Doppler spectra, we then extracted the precipitation-only spectra, S_{VHF}, following the procedure in section 3.2.3. An example of these spectra is presented in Figure 3.10, where the clear-air plus precipitation spectrum is plotted as a continuous line, and the S_{VHF} spectrum is plotted as a dotted line.

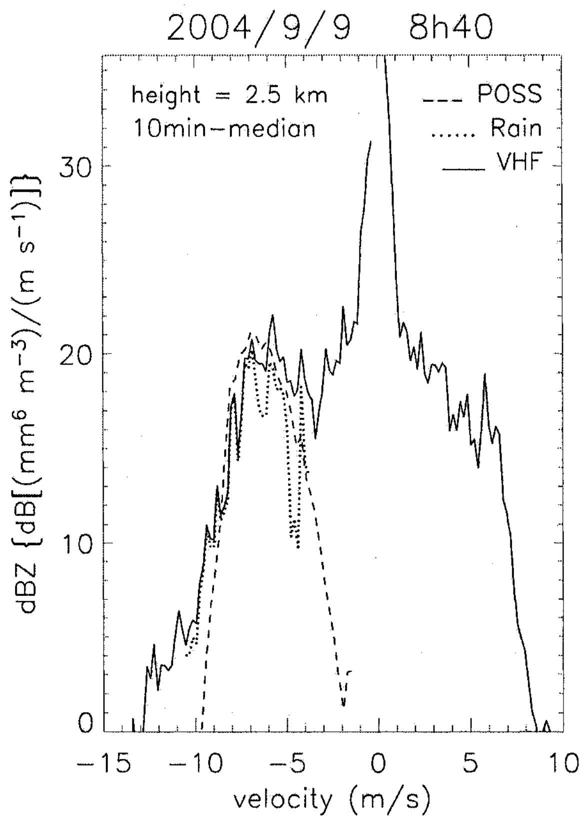

Figure 3.10. Comparison of Doppler spectra measured by the VHF radar (solid line for the full spectrum, and dotted line for the rain-only signal) and derived from POSS drop-size distributions (dashed line). The POSS spectrum has been corrected for the conditions at 2.5 km height (i.e., air vertical velocity and density). Each spectrum has been smoothed within a 10-minute window. These data were taken on September 9, 2004, at 8:40 UTC.

Finally, all S_{VHF} spectra were integrated in order to obtain a time series of VHF reflectivity-factors, Z_{VHF}. We eliminate those spurious or very weak observations where Z_{VHF} was less than 10 dBZ. Notice that, from a climatological reflectivity-rainrate relation valid for Montreal [e.g., $Z = 210\ \mathbf{R}^{1.47}$, by *Lee and Zawadzki*, 2005], Z = 10 dBZ corresponds to a rainrate of **R** = 0.13 mm/h. The resulting VHF time series is plotted in Figure 3.11 as a continuous line, for a precipitation event lasting about 10 hours, on 9 September 2004.

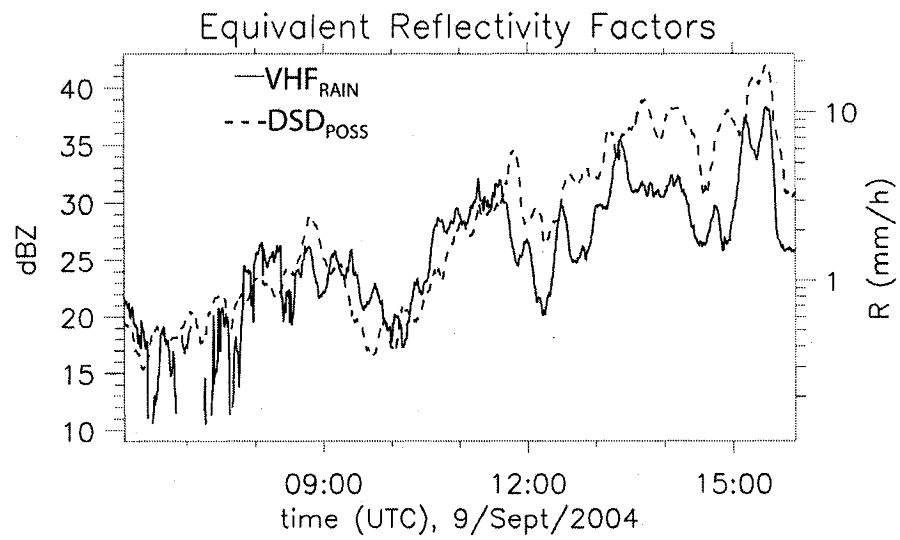

Figure 3.11. Time series of reflectivity factors measured by the VHF radar (in solid line, at 2.5 km) and derived from the POSS raindrop sizes (in dashed line, corrected for air density and vertical velocity at 2.5 km height). Reflectivity factors (in the left-side Y-axis) have been converted into rain rates (in the right-side Y-axis) by using a climatological relationship [*Lee and Zawadzki*, 2005].

3.3.2. Comparing VHF and POSS

In order to validate our VHF measurements of rain reflectivity factor, measurements of raindrop-size distributions where taken at ground level by the POSS instrument. The POSS is perhaps the drop-size sensor with the largest sampling volume currently available. Its drop-size distributions are representative of a sampling volume (per unit time) sized between 0.32 and 190 m^3 s^{-1} [depending on the drop diameters, D_e; *Campos and Zawadzki*, 2000], located at a height of about 2 meters above ground, and measured at one-minute resolution.

From the drop-size measurements, we computed the reflectivity factors as a function of drop-diameters, $Z(D_e) = N(D_e)\ D_e^6$. The POSS diameter channels were converted into Doppler velocity channels by first using the following polynomial fit to the observations by *Gunn and Kinzer* [1949]:

$$v_0 = -0.19274 + 4.96255\, D_e - 0.90441\, D_e^{\,2} + 0.05658\, D_e^{\,3} \; ; \qquad (3.46)$$

where v_0 is the terminal fall velocity (in m/s) at sea level for a raindrop of diameter D_e (in mm). Each terminal velocity at sea level, v_0, where then converted into a terminal velocity at 2.5 km height (the center of our VHF range gate), v_T, by using equations (3.41) and (3.42) in an ICAO standard atmosphere [*ICAO*, 1993]. Finally, the air vertical velocity (obtained from the clear-air peak in the VHF spectrum, as in section 3.2.3) was added to the 2.5-km raindrop velocities to obtain the Doppler velocity channels. At this point, we computed the Doppler spectra of reflectivity factors, S_{POSS}, from the ratio between the reflectivity factor at each diameter channel and the Doppler-velocity width of the corresponding spectral bin. These S_{POSS} spectra were then smoothed by computing the median value within a 10-minute moving window, for each spectral bin. An example of the results is presented in Figure 3.10, where the smoothed S_{POSS} spectrum is plotted as a dashed line. The general features in this Figure 3.10 are typical of those we have observed at other times, and they indicate good agreement between the VHF and POSS spectra. We can now proceed, in the following paragraphs, with a more quantitative comparison.

For each particular time of observation, we integrated the smoothed S_{POSS} spectra over the diameter range in order to obtain a POSS reflectivity factor, Z_{POSS}. We also eliminate observations where Z_{POSS} was less than 10 dBZ, as we did with Z_{VHF}. Figure 3.11 compares a 10-hour time series of Z_{POSS} (plotted in dashed line) and Z_{VHF} (in solid line). The systematic bias of Z_{POSS} with respect to Z_{VHF} is not always the same, and this is due to changes in the vertical gradient of reflectivity, which indicates the presence of different precipitation regimes between 2.5 km height and near the ground. The VHF systematic underestimation is clear during the second half of the period. However, before we quantified this bias, we corrected a small time lag found between the two time series. The magnitude of this time lag was obtained from the cross correlation between Z_{POSS} and Z_{VHF}. We found that the time when the cross correlation reaches its maximum is 1.8 minutes for this dataset, which corresponds to the time lag between the two time series. This time lag relates to a mismatch between the instruments clocks, as well as the time the raindrops took to fall from 2.5 km (where the VHF radar measured them) to 2 m above the ground (where the POSS measured them). We also found a maximum cross-correlation of 0.83 units for this dataset, which corresponds to the linear correlation coefficient when the time lag is corrected. This high correlation coefficient is indicative of the good efficiency in our method for extracting the precipitation signal out of the VHF Doppler spectra (i.e., our section 3.2.3).

We compared simultaneous measurements of Z_{POSS} and Z_{VHF} during several precipitation events (widespread, stratiform rain) occurring on 24 May and 9 September, 2004. In some cases we detected rain only in one of the two instruments. This is expected due to the different volumes that the POSS and the VHF radar represent, for example in cases when the raindrops directly above our VHF radar never fall over our POSS. However, we were able to collect more than

23 hours of rainfall simultaneously measured by our POSS and VHF sensors (a total of 2308 pairs).

Figure 3.12 presents a scatter plot for these Z_{POSS} and Z_{VHF} observations, obtained after applying the time-lag correction explained in the previous paragraph. From this dataset, the average bias of Z_{VHF} (with respect to Z_{POSS}) was obtained from the ratio between the total Z_{POSS} and the total Z_{VHF} (totals integrated over the whole observation period). This ratio has a value of 2.55, which indicates that VHF reflectivity-factors are about 4 dB lower than the reference POSS values. This is not a large difference considering the fact that the measurements from these instruments do not represent exactly the same volume in space (i.e., measurements with different representativeness, and raindrop populations that can evolve significantly during its descent). Using an X-band vertically-pointing radar, we verified that the differences between Z_{VHF} and $Z_{X\text{-}band}$ —when using similar sampling volumes—are in the order of 1 dB (see Figure 5.11, in Chapter 5). For reference, Figure 3.12 also plots (as a continuous line) the linear relation corresponding to this 4 dB bias. The correlation coefficient between Z_{POSS} and Z_{VHF} time series was also computed, which has a value of 0.82 (0.76 for the reflectivity factors expressed in dBZ). This high correlation coefficient, obtained in such complex conditions (dBZ fields are not completely homogeneous), validates our analysis methods.

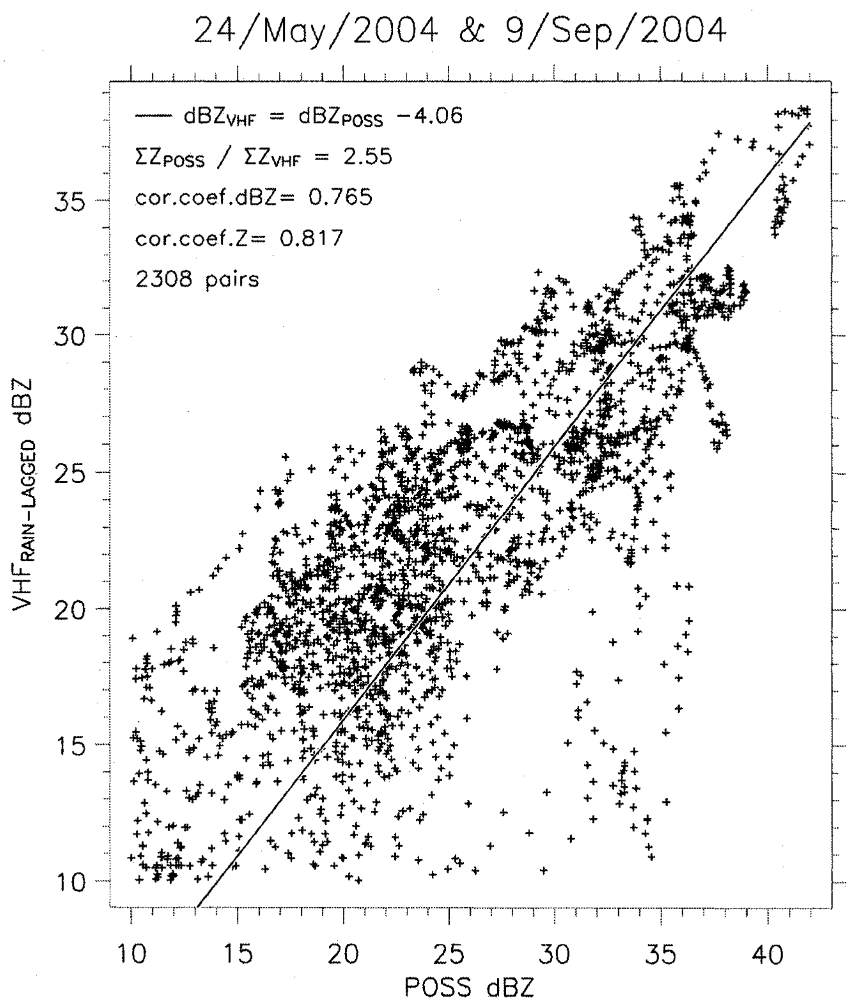

Figure 3.12. Scatter plot of reflectivity factors measured by the VHF radar and derived from POSS drop sizes. These observations correspond to more than 23 hours of rain simultaneously observed by our POSS and VHF radar, during 24 May and 9 September 2004 (2308 pairs in total). The observations have been corrected for any time lag between the two sensors. The line corresponds to the average bias of 4 dB. The correlation coefficients, in Z and dBZ, are presented as well.

3.4. Discussion

This chapter extends the operational capabilities of the VHF radar to measure precipitation intensity (in units of mm^6 m^{-3}) in addition to air velocity. To accomplish this, we presented the mathematical derivation of the VHF radar equation. We have also validated the assumption that $|K|^2$ is 0.93 ± 0.01 for rainfall measured by VHF radars. In addition, we provided an efficient method for extracting the precipitation signal out of VHF Doppler spectra. These aspects have been tested using rain observations taken by the McGill VHF radar and by a POSS distrometer. In particular, we compared VHF reflectivity factors [using equation (3.33)] with the corresponding reflectivity factors from reference raindrop sizes.

We acknowledge the fact that the POSS and VHF measurements correspond to different spatial volumes. On one hand, they correspond to different ranges. The VHF measurements correspond to the range at 2.5 km, while the POSS observations correspond to 2 meters height (above the ground). On the other hand, the magnitude of the VHF and POSS sampling volumes are very different. As well, the precipitation being measured aloft may not fall directly below, but it can be horizontally advected by the wind. We diminished the problem of representativeness by applying a time smoothing for both the VHF and POSS observations. We also corrected the POSS raindrop velocities for the changes of air density with height. As well, we selected typical cases of widespread precipitation, with bright-band above the 2.8 km height, where the vertical and horizontal gradients of reflectivity are generally small. In spite of these complex sources of uncertainty, we found a 4-dB bias between drop-size measurements and VHF time series, which is mainly due to representativeness errors. Even better, the linear correlation coefficients between Z_{POSS} and Z_{VHF} observations were in the order of 0.8. These results validate our entire analysis, which includes not only the derived VHF radar equation, but also the method for extracting precipitation signals out of VHF power spectra, and the VHF radar calibration (as in the method presented in Chapter 2).

Our retrieval of rain reflectivity factor (from observations of a single VHF radar) has not yet considered the effects of the space-variable reflectivity and antenna sidelobes. We then recognize that our radar equation in (3.15) is appropriate when dealing with radars that have a narrow transmitted beam and high range resolution. Relationship (3.15) may not be valid for radars with antenna pattern having significant side lobes (e.g., the McGill VHF radar). The reason is that the radar will receive additional power from scatterers located at the same distance but in a different direction than the range gate of the main beam. Therefore, the radar equation (3.13) is the one to be solved. For the particular case of the McGill VHF radar, we have obtained equation (3.33) from equation (3.15), which applies for scatterers in the far-field region and assumes a constant reflectivity within one-gate sampling volume. Future work will include the solution of equation (3.13) in a space-variable field of reflectivity, as well as the application of our methods in the analysis of precipitation formation.

CHAPTER 4:

EVALUATING THE EFFECTS OF A SPACE-VARIABLE REFLECTIVITY AND ANTENNA SIDELOBES INTO THE RADAR EQUATION

ABSTRACT

Using radar observations to quantify precipitation intensity requires the intervention of the radar equation, which converts the precipitation signal into reflectivity units. This equation generally assumes that the reflectivity is uniform within each sampling gate and that the sidelobes of the antenna pattern are negligible. Our purpose is to provide a more realistic approach that eliminates these assumptions when computing profiles of precipitation intensity (by using a space-variable reflectivity and antenna pattern of significant sidelobes to compute profiles of radar reflectivity factor). To achieve this, we obtained simultaneous observations of co-located vertically pointing radars, operating in the VHF and X bands, as well as raindrop-size measurements at the ground. We used the raindrop measurements to correct for attenuation in the precipitation signal at X band. Then, we simulated the precipitation signal in the VHF radar by combining this X-band signal and the VHF antenna pattern into a general version of the radar equation. The simulated precipitation signal at VHF compares well with actual measurements by the VHF radar, and this validates our analysis methods. In conclusion, our analysis indicates that VHF reflectivity at gates above the melting layer is artificially enhanced by the precipitation signal collected in the side-lobe direction.

4.1. Introduction

Quantitative measurements of meteorological variables by radar imply the use of the Radar Equation. This is a relationship that links the radar received power to the scatterers cross-sections. Standard forms for this equation assume, most of the time, an average scatterer cross-section per unit volume (or radar reflectivity) that is constant within the sampling volume of a given range gate. Under these conditions, and neglecting the effect of the convolution of the transmitted pulse with the reflectivity profile, the radar equation is given by the following expression [for details on its derivation, see Chapter 3, equation (3.18)]:

$$P_r = \frac{P_{Tx}\, e_T\, (D_{\max})^2\, \lambda^2\, \overline{\eta}}{(4\pi)^3} \left[\frac{L/2}{R^2 - (L/4)^2}\right] \int_{\phi=0}^{2\pi} \left\{ \int_{\theta=0}^{\pi} [F(\theta,\phi)]^2 \sin\theta\, d\theta \right\} d\phi\,; \tag{4.1}$$

where P_r is the received power (in Watts), P_{Tx} is the transmitter power (in Watts), e_T is the antenna efficiency during pulse transmission, D_{max} is the maximum directivity of the antenna pattern, λ is the radar transmitted wavelength (in meters), $\overline{\eta}$ is the radar reflectivity (in m^{-1}) averaged over the sampling volume, F is the one-way normalized polar-diagram (or antenna pattern), ϕ is the azimuth angle, θ is the zenith angle, R is the range at the center of a given radar gate (in meters), L is the transmitted pulse length (in meters).

Equation (4.1) is appropriate when dealing with radars that have a narrow transmitted beam and high range resolution. However, this relation may not be valid for radars with antenna pattern having non-negligible side lobes. The reason is that the radar will receive some of its power from scatterers located at the same distance but at a different angle to the direction of the main beam. (The McGill VHF radar, for example, has been designed to have the narrowest main-beam possible, to facilitate determinations of turbulent energy dissipation rate from spectral widths [i.e., the method described by *Hocking*, 1985, section 7]; however, this narrowest main beam results in larger sidelobes.) Therefore, it is the following radar equation that needs to be solved [for details on its derivation, see Chapter 3, equation (3.13)]:

$$P_r = \frac{P_{Tx}\, e_T\, (D_{\max})^2\, \lambda^2}{(4\pi)^3} \int_{r=R-L/4}^{R+L/4} \int_{\phi=0}^{2\pi} \int_{\theta=0}^{\pi} \frac{\eta(r,\theta,\phi)\,[F(\theta,\phi)]^2 \sin\theta}{r^2}\, d\theta\, d\phi\, dr. \tag{4.2}$$

As mentioned in the Appendix, the term $r^{-2}\, \eta(r,\theta,\phi)$ inside the previous integral should be strictly speaking $[r^{-2}\, \eta(r,\theta,\phi)] \otimes g(r)$; where the symbol $\otimes$ represents a convolution, and *g(r)* describes the transmitted pulse as a function of range *r*. This analysis, however, will not consider the effects of the pulse shape, and will therefore assume a square pulse such that

$$\frac{\eta(r,\theta,\phi)}{r^2} \otimes g(r) \cong \frac{\eta(r,\theta,\phi)}{r^2}. \tag{4.3}$$

The effect of the space variability in the reflectivity has been discussed in the light of the radar equation [e.g., *Hocking and Rottger*, 1983; *Zawadzki*, 1982; *Rogers*, 1971]. However, for tropospheric signals, there are no published analyses of this effect in combination with the sidelobes of an antenna pattern. The objective of this chapter is then to explore the effects of this more realistic approach [i.e., using equation (4.2) in combination with a space-variable reflectivity and with an antenna pattern of non-negligible sidelobes] when computing profiles of precipitation intensity.

4.2. Methods

Recall that the radar reflectivity, for Rayleigh scatterers, can be expressed as [e.g., *Rinehart*, 1997, equation 5.13]:

$$\eta = \frac{\pi^5 |\mathrm{K}|^2}{\lambda^4} \frac{Z}{10^{18}}; \tag{4.4}$$

where $|\mathrm{K}|^2$ is the dielectric factor, and λ is the wavelength of the radar transmitted pulse (in meters). Z is the reflectivity factor (expressed in $\mathrm{mm}^6\ \mathrm{m}^{-3}$), and it provides a measure of the precipitation intensity for hydrometeor targets. By convention [e.g., *Smith*, 1984], if $|\mathrm{K}|^2$ is taken equal to 0.93 (the value corresponding to liquid water at near 20°C, and wavelengths in the S band), then $Z = Z_e$, the equivalent radar reflectivity factor. This convention is adopted because when radar measurements are made, one is often not certain of the hydrometeor phase or composition (i.e., we are uncertain of the dielectric factor values).

Hence, from an original field of Z_e we can derive a field of η using equation (4.4), and then apply either equations (4.1) or (4.2) in order to obtain the radar received power. Operationally, however, the radar measures received powers, and these have to be converted into equivalent reflectivity factors. This can be done easily from equation (4.1), using $\eta = \overline{\eta}$, but it cannot be done directly if the more realistic equation (4.2) is used (because here η is within the integral).

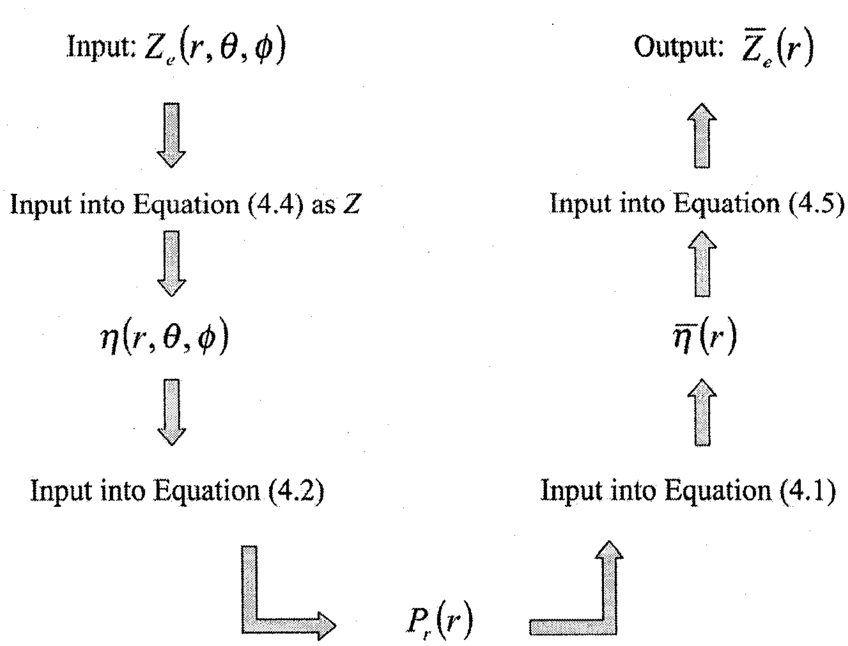

Figure 4.1. Flowchart describing the process by which we simulate profiles of equivalent reflectivity factor at VHF band. It uses equation (4.2) in combination with a space-variable reflectivity at X-band, and with a VHF antenna pattern of non-negligible sidelobes.

However, we were able to simulate VHF reflectivity factors through equation (4.2), using as input the precipitation signal at X band, and validating the simulation with corresponding measurements at VHF band. Figure 4.1 summarizes our method, which is explained as follows. First, a field of Z_e is input in equation (4.4) in order to obtain η ($|K|^2 = 0.93$ is used here). Then, we input this equivalent reflectivity factor into equation (4.2) to obtain a realistic radar received power (for a given radar range gate). Next, we input the received power from equation (4.2) into equation (4.1) in order to obtain an average (within the radar gate) reflectivity, $\overline{\eta}$. An average equivalent reflectivity factor (for the radar gate) is then obtained by rearranging equation (4.4) as follows:

$$\overline{Z}_e = \frac{\lambda^4 \, 10^{18}}{\pi^5 \, |\mathrm{K}|^2} \, \overline{\eta} \, . \tag{4.5}$$

The procedure is repeated for all radar range gates. At the end, we are able to compare the output $\bar{Z}_e$ and the original Z_e fields.

For simplicity, we used Z_e fields that were variable only with height z (i.e., one-dimensional fields). Therefore,

$$\eta = \eta(z) = \eta(r \cos\theta)\,. \tag{4.6}$$

As well, we used for $[F(\theta,\phi)]^2$ the values plotted in Figure 4.2, which come from a simulation of the McGill VHF antenna polar diagram provided by *Mardoc* [2002]. The values in Table 4.1 were also used.

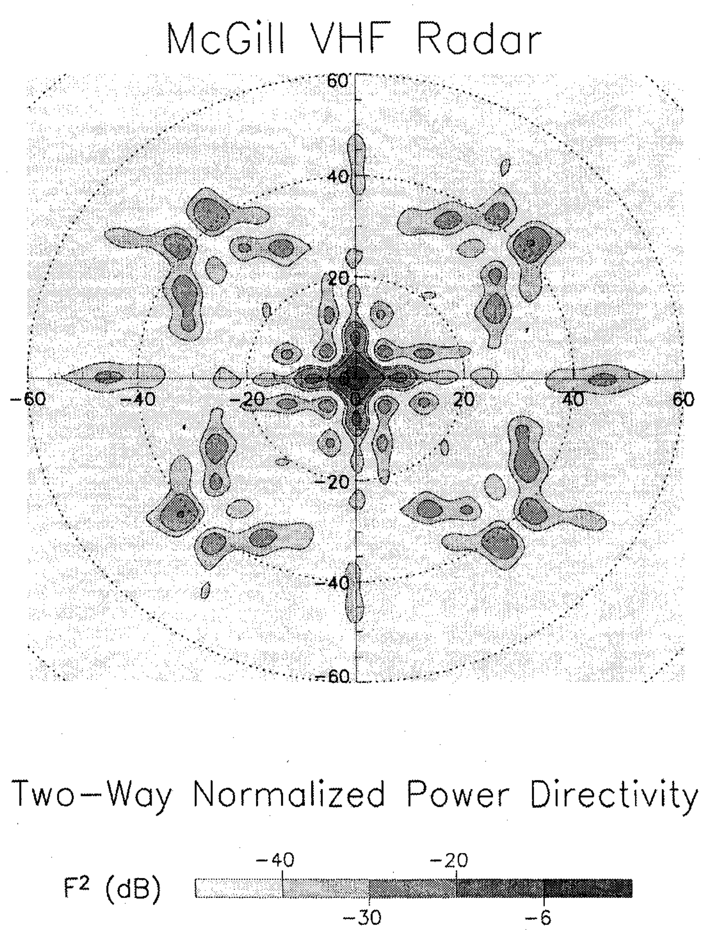

Figure 4.2. Two-way antenna pattern of the McGill VHF radar.

Table 4.1. McGill VHF Radar parameters

Parameter	Value
Transmitted wavelength (λ)	5.77 m
Peak transmitted power (P_{Tx})	40 kW
Antenna efficiency (e_T)	0.631
Maximum directivity (D_{max})	456.9
Transmitted pulse length (L)	1 km

Notice that the integrals in equations (4.1) and (4.2) were computed numerically. Therefore, the accuracy of the programs used for integration required some prior testing. (The reason is that computations were very sensitive to the antenna pattern resolution.) Consequently, we first generated a synthetic Z_e profile that was constant in height (i.e., the vertical dashed line in Figure 4.3), put this profile in equation (4.4) to obtain η, input this reflectivity into (4.2), and solved this equation numerically (i.e., the method in Figure 4.1). In principle, the reflectivity factors resulting after numerical integration ($\bar{Z}_e$) have to be the same than the input (Z_e), but this will not be true if the resolution used is too coarse for an accurate numerical integration. Therefore, we gradually increased the integration resolution until the output $\bar{Z}_e$ equalled the input Z_e. These two profiles for the optimal integration resolution are plotted in Figure 4.3, where the solid vertical line ($\bar{Z}_e$ constant) is on top of the dashed vertical line (Z_e constant).

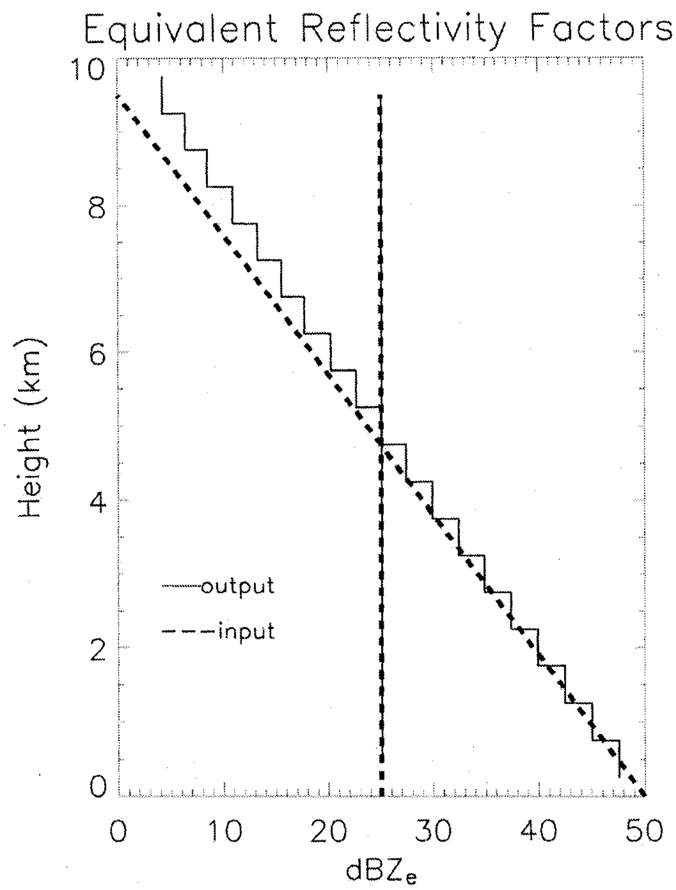

Figure 4.3. Simulation of synthetic Z_e profiles as they are detected by the full antenna pattern. Vertical lines (dashed line on top of solid line) correspond to a validation test with input of constant Z_e. Diagonal lines correspond to a linearly decreasing profile of Z_e. Dashed lines are input profiles (Z_e) and solid lines (both continuous and stepped lines) are output profiles ($\bar{Z}_e$), according to the algorithm in Figure 4.1.

After validating the integration programs, we generated other different profiles of equivalent reflectivity factor, and then considered their range variation when computing the $\bar{Z}_e$ values through equation (4.2), i.e., using the method in Figure 4.1. The profiles are made from zero to 10 km height, which is the typical range for the troposphere in mid-latitudes. The first profile is a synthetic reflectivity factor that decreases exponentially (linearly in dB) with height. The second profile is an artificial layer of 70 dBZ at 7 km height, and zero dBZ everywhere else. The third profile is a synthetic step function, which has a magnitude of 50 dBZ from ground to 4 km height, and zero dBZ aloft. The last profile corresponds to reflectivity factors measured by a high-resolution, vertically-pointing, X-band radar [i.e., the McGill VPR radar, described by *Zawadzki et al.*, 2001]. In order to correct for precipitation attenuation at X band, we collected measurements of raindrop sizes near the ground. For this, we use a Precipitation Occurrence Sensor System [POSS, described by *Sheppard*, 1990], which was collocated with the VPR and the VHF radars. The results of our analysis are presented in the next section.

4.3. Results

The first profile of reflectivity factors, where a synthetic Z_e decreases with height at 10 dBZ_e per km (a typical decrease observed in snow over Montreal), is presented in Figure 4.3 as the diagonal dashed line. The corresponding profile of output $\bar{Z}_e$ is also plotted in Figure 4.3 as the diagonal stepped line. The results indicate an increase in the $\bar{Z}_e$ slope with height. No significant difference between $\bar{Z}_e$ and Z_e is observed below the 4 km level, but the difference between input and output is greater at higher ranges (reaching about 4 dBZ_e at 9 km height).

The second profile is plotted as a thick dashed line in Figure 4.4. This is a synthetic layer of 70 dBZ magnitude, at 7 km height, and 75 m thickness (and zero dBZ everywhere else). Similar types of signals have been observed by our X-band radar when an aircraft is in its sampling volume. Of course, these aircraft signals do not last more than a minute. However, for our numerical simulation, we will assume that this second profile corresponds to a layer present in the whole sampling volume of our VHF radar. The output $\bar{Z}_e$ is plotted as the thick stepped line in Figure 4.4, and it shows a broadening on top of the input profile, which extends up to the top of the simulation domain. This result is similar to the ionospheric observations at Adelaide (35°S, 138°E) by *Hocking and Vincent* [1982, Figure 5]. In both cases, the spurious signals are due to scatter received through the antenna side lobes.

The third profile, also plotted in Figure 4.4 as a thin dashed line, corresponds to a synthetic step function, which has a magnitude of 50 dBZ from ground to 4 km height, and zero dBZ aloft. This profile is similar to the backscatter signal from a summer rain shower as observed by microwave (centimetre wavelength) radars, where rainrates of similar intensity are present from the base to the top of the cloud. The output $\bar{Z}_e$ is plotted in Figure 4.4 as the thin stepped line. The output profile resembles well the input Z_e at heights below 4km, but the sidelobes receive enough scatter at ranges between 4 and 10 km, such that the output $\bar{Z}_e$ profile is contaminated above 4 km.

A fourth, more realistic profile is presented in Figure 4.5, where the input Z_e is in dashed line and the output $\bar{Z}_e$ is in solid stepped line. For this, we considered a set of typical (for Montreal) height profiles of equivalent reflectivity factor measured by the McGill VPR radar. The VPR dataset corresponds to Z_e values at a time resolution of about 30 seconds and at a range resolution of about 75 meters. We smoothed these VPR measurements by taking, for each particular range gate, the 10-minute median value. Notice that $\bar{Z}_e$ is in fact a simulation of the VHF Z_e, which is obtained from the Z_e observations at X-band.

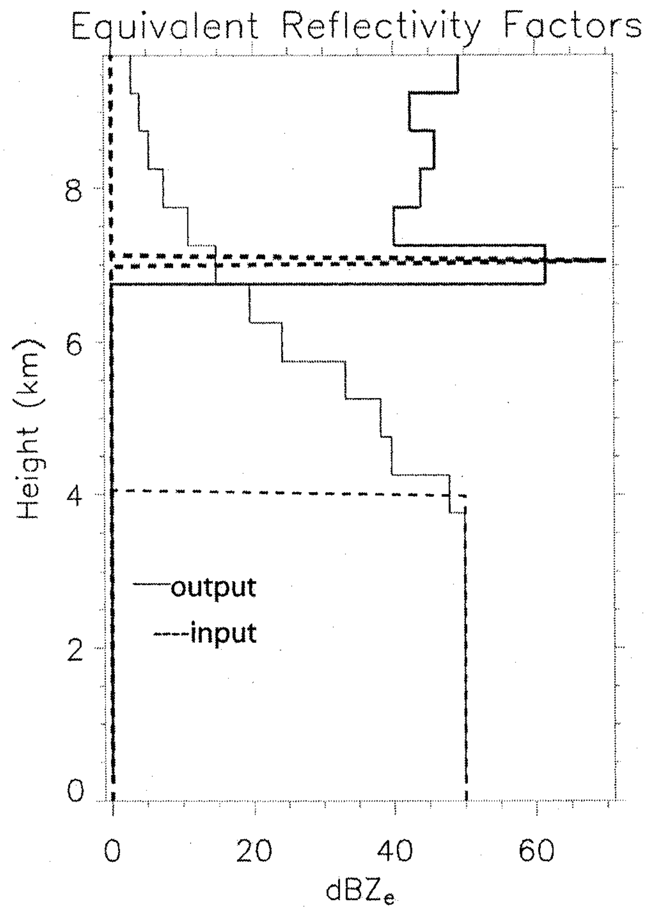

Figure 4.4. Additional simulations of synthetic Z_e profiles as they are detected by the full antenna pattern. Thick lines correspond to a stratified layer of 70 dBZ at 7 km height. Thin lines correspond to a region of 50 dBZ below 4 km height. Dashed lines are input profiles (Z_e) and stepped lines are output profiles ($\bar{Z}_e$), according to the algorithm in Figure 4.1.

Since the VPR operates at X band, precipitation attenuation has to be considered. We then calibrated the VPR measurements by comparing the equivalent reflectivity factors measured at X-band and the corresponding values derived from drop-size distributions at ground.

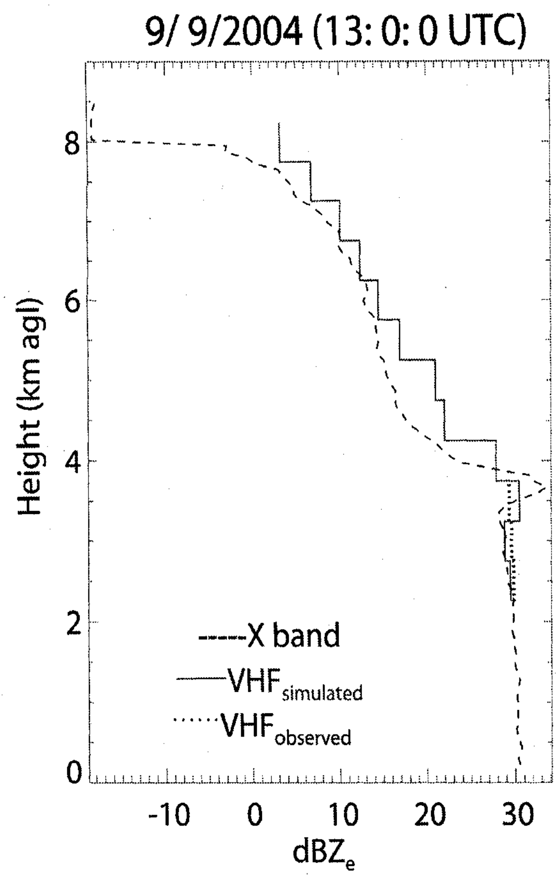

Figure 4.5. Simulated VHF $\bar{Z}_e$ profile (solid stepped line) from observed X band Z_e profile (dashed line, which already include the attenuation correction). The corresponding VHF observations are plotted as the dotted line. For this, co-located and simultaneous radar observations, at X and VHF bands, were taken on September 9, 2004, at 13:00 UTC.

To validate our simulation, the rain signal measured by the VHF radar is also plotted as a dotted line in Figure 4.5. This rain signal was obtained from the algorithm described in Chapter 3. The application of this algorithm is presented in Figure 4.6, for a profile of Doppler spectra measured by our VHF radar. In these examples, the crosses (linked by dotted curves) correspond to Doppler spectra at different heights, smoothed within a 10 minutes window. The vertical lines correspond to the air vertical velocities, as the algorithm derives them for each height. The dark areas correspond to the derived precipitation signal. Notice that this algorithm can deal mainly with the precipitation signal coming from ranges up to the bright band, where precipitation spectra are not merged with the clear-air spectra.

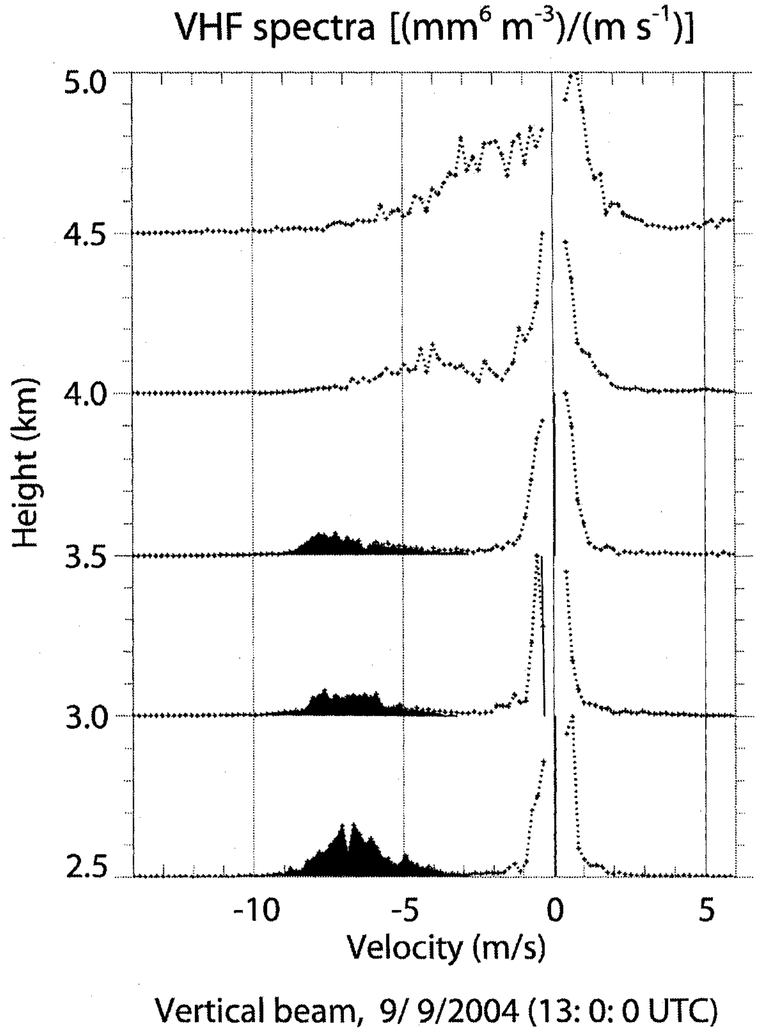

Figure 4.6. Vertical profile of reflectivity-factor densities observed by the McGill VHF radar on 9 September 2004, at 13:00 UTC. The dotted lines correspond to raw Doppler spectra, and the dark areas below each spectrum correspond to the precipitation signal, according to the algorithm described in Chapter 3. These dark areas relate to the rain Z_e values plotted as dotted line in Figure 4.5. Vertical lines are drawn at the spectral bins corresponding to the clear-air vertical velocities. Above 3.5 km height, the precipitation is in solid or melting phase, and the precipitation spectra merge with the clear-air spectra.

4.4. Discussion

From this chapter, it is found that the space-variable reflectivity has a noticeable effect on the radar equation only above the melting level. Above these heights, the side lobes of the antenna polar diagram collect enhanced power from scatterers located in the bright-band (i.e., ranges in the side-lobe direction corresponding to bright-band height).

For the single profile presented in Figure 4.5, the comparison between the simulated and measured VHF rain signals (respectively, the dotted and solid lines in Figure 4.5) presents good agreement. This agreement validates our numerical computations. Additionally, these comparisons can be used in a calibration method for VHF Stratospheric-Tropospheric radars, if the VHF radar observations are expressed in au (i.e., the units of the analog-to-digital-converter in the receiver, as already defined in Section 2.1), and if more reflectivity profiles at X-band are analyzed.

From these results, we also expect that rain-only equivalent reflectivity factors will be about the same at X band than at VHF band (when X band measurements are corrected for attenuation). Therefore, it is valid to use equation (4.1) for quantitative measurements of rain by VHF radars. However, the expression (4.2) has to be considered when dealing with snow quantitative measurements at VHF band.

In general, the differences in Z_e from observations at X and VHF bands can be assumed to be due mainly to (a) incorrect radar absolute calibration, (b) $|K|^2 \neq 0.93$, (c) effect of the space-variable reflectivity and antenna sidelobes, (d) inaccurate consideration of the antenna polar diagram *F*, (e) non-uniformity of the raindrop field observed by the VHF radar [see *Fabry*, 1996, for implications]. In this work, we have already minimized the effects of points (a), (b), (c), and (d). As a result, no significant differences were found between modeled and observed rain signals.

CHAPTER 5:

THE STRUCTURE OF AIR REFRACTIVE INDEX IN THE PRESENCE OF PRECIPITATION

ABSTRACT

The spatial distribution of the air refractive index determines the backscattering experienced by electromagnetic waves. In the troposphere, turbulence is a common mechanism that generates fluctuations or irregularities in the refractive index. Under these conditions, the strength of the refractive-index irregularities is given by C_n^2, the structure-function parameter for refractivity turbulence. We recognize that the turbulent spatial structure of air refractive index can change through dynamic (wind driven) and thermodynamic (temperature and moisture driven) processes. However, it is still unclear what effect the precipitation has on the scattering properties of the clear air.

To study the direct and indirect pathways by which precipitation can affect clear-air scattering, this work analyzed several cases of stratiform and convective rain, occurring in a continental mid-latitude environment (Montreal). For these cases, Doppler spectra taken by a VHF vertically-pointing radar were used to retrieve simultaneous co-located values of precipitation intensity (rainrates) and degree of refractive index fluctuations (C_n^2). We validated these retrievals using co-located measurements of precipitation signal at X-band. The measurements at X band were previously calibrated to compensate for rain attenuation. The analysis compares the Doppler spectra taken at different heights by the X and VHF radars. As well, the study includes rainrates between 0.3 and 78 mm/h, and C_n^2 values between 10^{-16} and 10^{-12} $m^{-2/3}$, retrieved from the VHF spectra at 2.5 km height. The research finds that C_n^2 fluctuations in rain are smoother than in precipitation-free conditions, and that its temporal changes are of turbulent nature for the most intense rainrates.

5.1. Introduction

The spatial distribution of the atmospheric refractive index determines the backscattering experienced by electromagnetic waves. This index n [already defined in equation (1.3) of the Introduction Chapter] depends on the composition and density of the medium in which the waves propagate. In common meteorology applications, the medium is considered to be either air or air mixed with precipitation particles (e.g., rain or snow). For backscatter analyses in radar applications, we are therefore interested in measuring the mean square fluctuations of the refractive index. As reviewed in Chapter 1, these fluctuations can be due to processes such as turbulence, specular reflections, and viscosity waves.

For the particular case of turbulence backscattering, *Tatarski* [1961] has developed a theory in which the spatial irregularities in the refractive index are caused only by turbulence (locally isotropic eddies in the inertial range, with dimensions of half the radar wavelength) acting on mean gradients of the refractive index. The strength of these irregularities is given by C_n^2, the structure-function parameter for refractivity turbulence [already defined in equation (1.4) of the Introduction Chapter]. The parameter C_n^2 depends on the refractive index and the turbulence intensity as in the following relation [e.g., *Hocking*, 1985, equations (4) and (43)]

$$C_n^2 = \frac{0.69\, \varepsilon^{2/3}\, M^2}{\omega_B^2} \; ; \tag{5.1}$$

where ε is the turbulent energy dissipation rate and ω_B is the Brunt-Vaisala frequency. $M = d\bar{n}/dz$ is called the vertical gradient of the potential refractive index, where the potential refractive index refers to the refractive index for an atmosphere in which potential temperature and specific humidity are constant with height [*AMS*, 2000].

Therefore, from equation (5.1), one can see that the C_n^2 parameter can be affected either thermodynamically, through the parameters M and ω_B, or dynamically, through the variable ε. Thermodynamic processes that affect C_n^2 refer mainly changes in the amounts of moisture, temperature and atmospheric stability, while the dynamic processes refer to changes in the turbulent mixing of the refractive index field.

S-band (10 cm wavelength) radar observations of non-precipitating cumulus clouds indicate an enhanced, mantle-like echo from turbulence scattering around the sides and tops of the clouds, particularly in the early growing stages of the small cumulus clouds. *Knight and Miller* [1998] have noticed that the most intense, well-defined mantle echoes occur when clouds penetrate the driest air, and they propose two explanations. The first potential reason is that variations in the index of refraction are expected from local variations in the water vapor content [up to several g m^{-3} at cloud boundaries, which will affect the term M^2 in our equation (5.1)]. These water vapor variations are due to entrainment of sub-saturated air filaments containing no liquid water, which mix with the cloudy saturated air. The mixing between filaments of entrainment air and cloud droplets will make the dry-air filaments to become as moist as the rest of the cloud.

However, new filaments of dry air are created continually in the mixing process close to the cloud edges, and so there might be strong contributions to the turbulence scattering from them. The second explanation for the observed behavior of the mantle echo intensities may be invigoration of small-scale turbulence from local buoyancy differences [i.e., the term ε in our equation (5.1)] caused by the strong evaporative cooling at cloud edge.

At this point, it is still unclear what effect precipitation has on the scattering properties of the clear air. *Rogers et al.* [1994, p. 539] suggested that the most reasonable effect of rain on the layers of enhanced clear-air reflectivity would be to increase the vapor content at the driest levels, where evaporation would be strongest, and to chill the air at these levels. The air would be cooled (towards the wet bulb temperature) and saturated, and the humidity gradient would then be smoothed. As a consequence, we should observe a reduction in C_n^2 caused by rain. The previous mechanism corresponds to what we can call the direct effect of precipitation on the clear-air scattering. With respect to this direct effect, *Chu et al.* [1994, fig. 2] claim to have shown for the first time that the turbulent refractivity echoes below the melting level may be depleted so severely, such that the precipitation echoes are enormously greater than the refractivity returns by about 15 dB. However, another possible explanation for their observations can be that the precipitation signal simply got stronger. On the other hand, *McDonald et al.* [2004] analyzed 33 days in which rainrates were larger than 6 mm/h (for a continuous period greater than or equal to 20 minutes), and they find that VHF received power (clear-air plus precipitation signals, non-calibrated) is reduced during precipitation. This proves indirectly that a reduction in C_n^2 can be associated with precipitation. There are, however, other reports of C_n^2 enhancements associated to rain [*Rogers et al.*, 1994; *Cohn et al.*,1995].

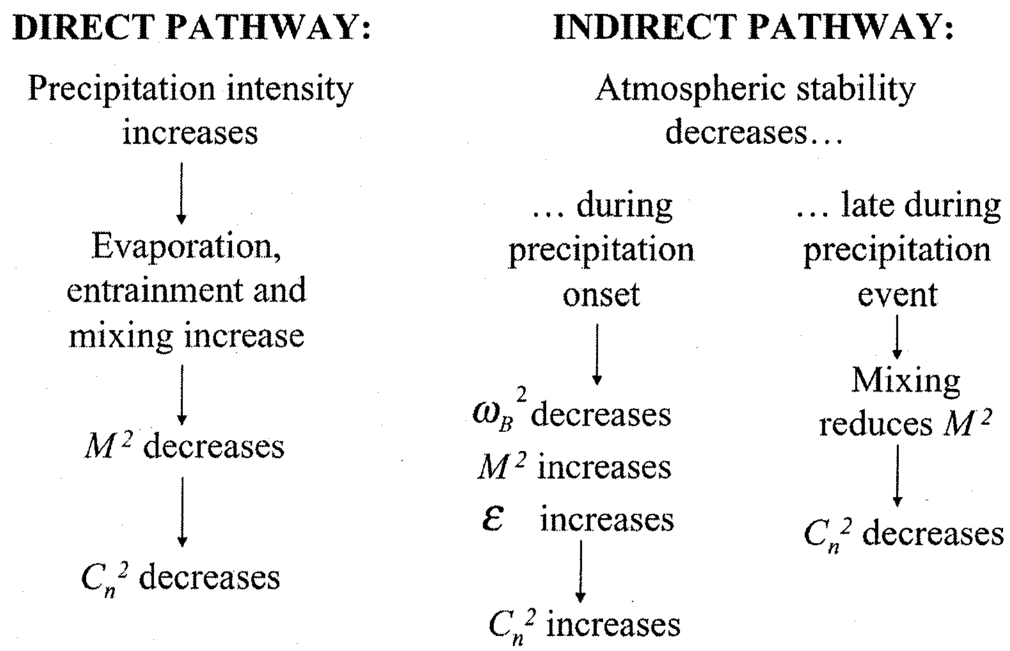

Figure 5.1. Different pathways by which precipitation can affect the scattering properties of clear air.

The problem is complex, and we also need to consider the indirect effects of precipitation on the scattering properties of the air. Figure 5.1 summarize the most probable pathways for these indirect effects, which depend mainly on atmospheric stability. During the onset of precipitation, stability is reduced with respect to a non-precipitating environment, and the term ω_B^2 in equation (5.1) becomes smaller. We can guarantee high moisture values as well as a reasonable vertical gradient of humidity for the precipitating environment (which is not always possible in the non-precipitating conditions), and this implies that the term M^2 in equation (5.1) may well become larger than during non-precipitating conditions. Recall that as an air parcel ascends, it will experience a decrease of temperature with increasing height, and its saturation vapor pressure (which is proportional to temperature) will also decrease, therefore producing a moisture vertical gradient. The term ε in equation (5.1) is free to vary during precipitation in a similar manner as in the non-precipitating conditions, but the vertical motions generated by the atmospheric instability will promote mixing during the onset of precipitation, increasing ε. Therefore, C_n^2 is allowed to increase for the precipitating atmosphere. Some time (about a few tens of minutes) after the beginning of precipitation, however, it is possible that the air vertical mixing can reduce the humidity and temperature gradients, reducing M^2 and C_n^2. An additional consideration is that low atmospheric stability and high humidity values can enhance the intensity of precipitation itself, and then reinforce the direct pathway suggested by *Rogers et al.* [1994]. In order to test the previous theoretical considerations, we require a more observational approach.

The previous chapters in this thesis provide a unique set of tools for studying—from an observational point of view—the effects of precipitation on the structure of air refractive index. See for example Figure 5.2, which corresponds to VHF Doppler spectra in the ranges from 2.5 to 5.5 km. Although the precipitation signal cannot be clearly differentiated from the turbulence air signal at 4 km (approximately the zero Celsius level) and above, we can quantify at lower gates the magnitudes of C_n^2, spectral width of air signal, and equivalent reflectivity factor (Z_e). This provides a unique dataset of simultaneous measurements of turbulence intensity, refractive index structure and precipitation intensity. In fact, this study will show that the occurrence of rain is associated to important changes in C_n^2 , which are of turbulent nature for the most intense rainfalls.

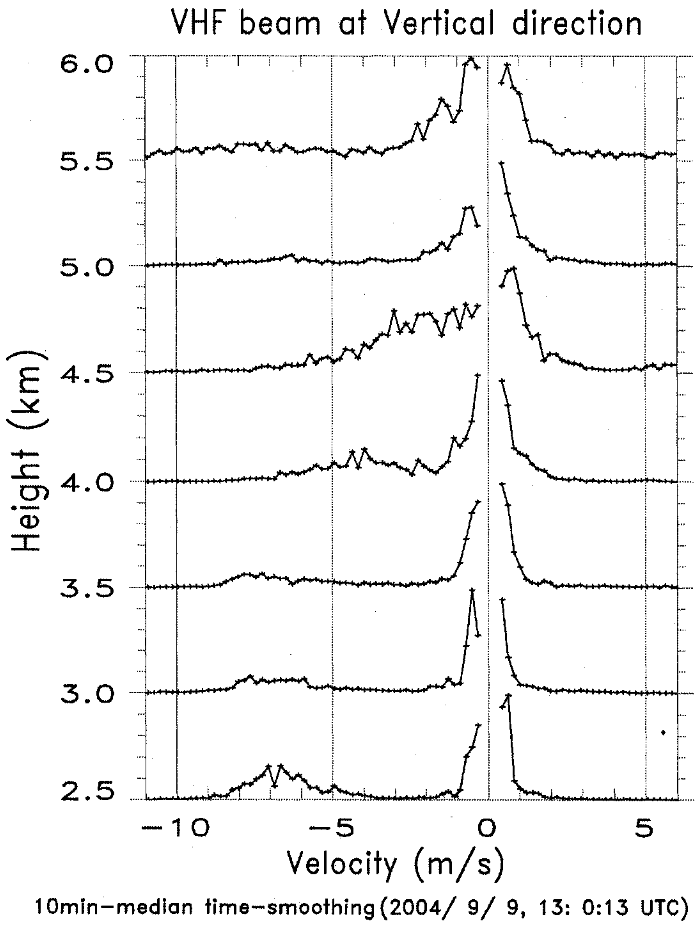

Figure 5.2. Example of VHF Doppler spectra in precipitation. These spectra have been smoothed using the median spectral densities in a 10-minute moving window. For this event, the melting level was located at about 4 km height (see Fig. 5.3).

5.2. Methods

5.2.1. Dataset

This study analyzed several cases of stratiform and convective rain, occurring in a continental mid-latitude environment (Table 5.1). For these cases, Doppler spectra taken by the McGill VHF radar (vertically-pointing) were recorded, then calibrated by the method in Chapter 2, and then input into the signal processing algorithm described in Chapter 3. This results in a dataset of rain and clear-air Doppler spectra, which were then used to retrieve simultaneous co-located values of precipitation intensity (equivalent reflectivity factors and rainrates, as in section 3.3.1 of this thesis) and intensity of refraction due to turbulence (structure-function parameter for refractivity turbulence, C_n^2, from equation 1.6), in addition to the spectral width of the clear-air spectra (as a proxy for turbulence intensity).

Table 5.1. Summary of analyzed rain events, occurring in a continental mid-latitude environment (Montreal), in which simultaneous and co-located radar measurements were taken at VHF and X bands.

Date	Recorded duration	Characteristics
24 May 2004	00 to 24 UTC	Mainly stratiform, with melting layer between 3 and 3.4 km height.
10 August 2004	21:30 to 24 UTC	Mainly convective, with melting layer near 3.3 km height.
11 August 2004	0:00 to 2:45 UTC	Mainly convective, with melting layer near 3.0 km height.
9 September 2004	04:40 to 13:40 UTC	Mainly stratiform, remnants of Hurricane Frances, with melting layer between 3.2 and 4.0 km height.

For the events in Table 5.1, Figures 5.3, 5.4, 5.5 and 5.6 provide time versus height plots of equivalent reflectivity factors and Doppler velocities. These were obtained from co-located measurements of precipitation signal at X-band by the McGill VPR radar [described by *Zawadzki et al.*, 2001]. Although these X band measurements have not been compensated for rain attenuation, they provide a general idea about the intensity and nature of the precipitation events summarized in Table 5.1. For example, notice the persistence of a bright band in the rain events on 24 May and 9 September, 2004. These bright bands occur close to the level of the zero Celsius isotherm (i.e., the melting layer given in Table 5.1), and they are indicative of stratiform precipitation.[e.g., *Fabry and Zawadzki*, 1995]. The rain events on 10 and 11 August 2004, on the other hand, show clear examples of convective rain (i.e., absence of bright band).

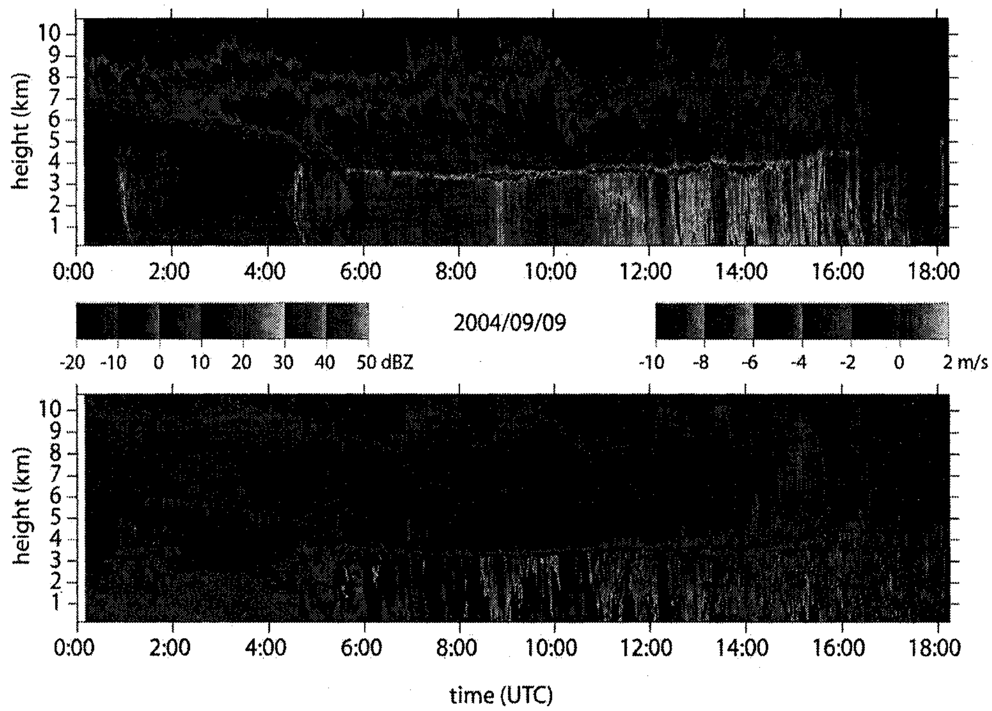

Figure 5.3. Time series for profiles of Z_e at X band, for the stratiform rain on 9 September 2004. Upper panel corresponds to equivalent reflectivity factors (including rain attenuation, according to the color scale to the left) and lower panel to the Doppler velocity (according to the color scale to the right).

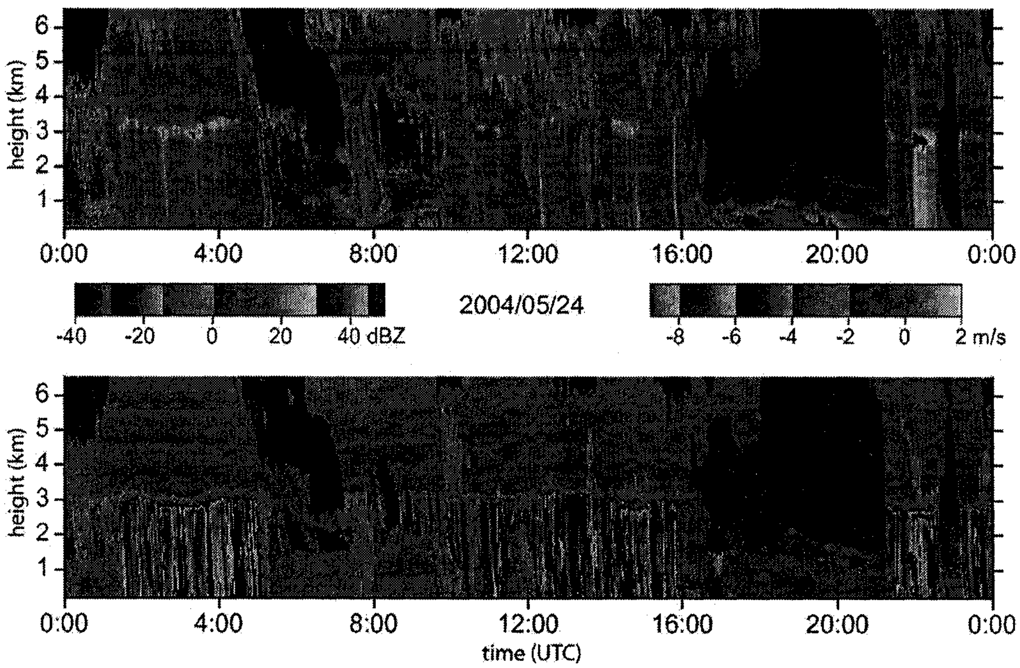

Figure 5.4. Time series for profiles of Z_e at X band, for the stratiform rain on 24 May 2004. Upper panel corresponds to equivalent reflectivity factors (including rain attenuation, according to the color scale to the left) and lower panel to the Doppler velocity (according to the color scale to the right).

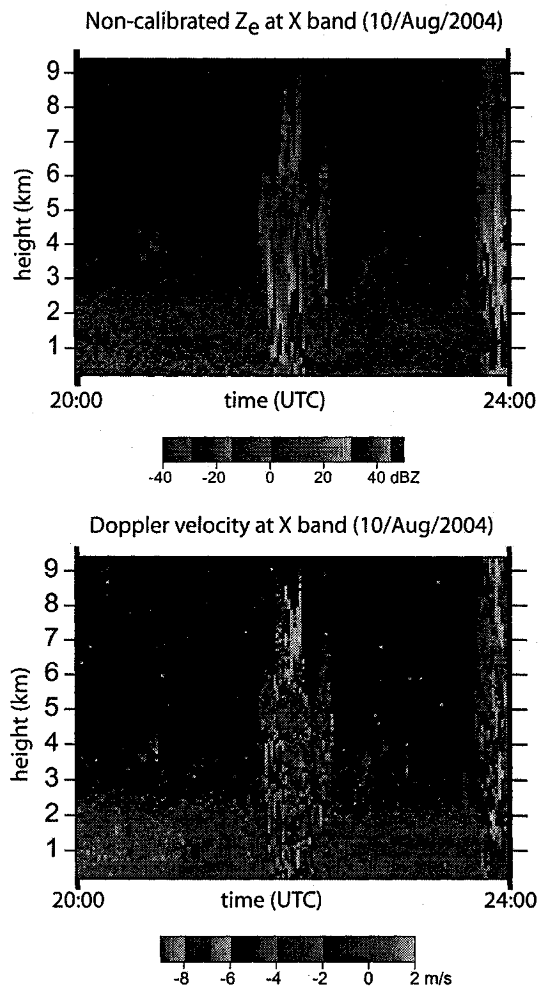

Figure 5.5. Time series for profiles of Z_e at X band, for the convective rain on 10 August 2004. Upper panel corresponds to equivalent reflectivity factors (including rain attenuation, according to the color scale below the plot) and lower panel to the Doppler velocity (according to the color scale below the plot).

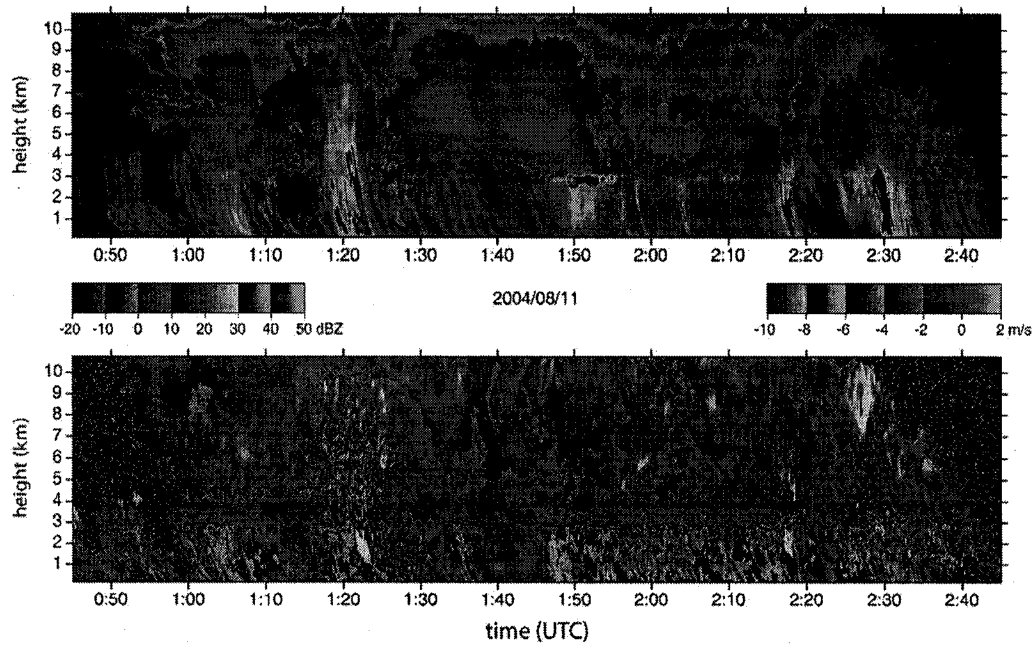

Figure 5.6. Time series for profiles of Z_e at X band, for the convective rain on 11 August 2004. Upper panel corresponds to equivalent reflectivity factors (including rain attenuation, according to the color scale to the left) and lower panel to the Doppler velocity (according to the color scale to the right).

5.2.2. Analyses

The analysis starts by comparing the Doppler spectra taken at several heights by the X and VHF radars. As before, the Doppler spectra at X band were smoothed in range by using the average spectral density within a 500-meter window (i.e., the range resolution of the VHF observations), and all spectra (at VHF and X bands) were smoothed in time by using the median spectral density within a 10-minute moving window (or a three-minute moving window for the convective cases). We also correct for any time lag that may exist between the two time series, by finding the peak of the cross-correlation between equivalent reflectivity factors at VHF and X bands, at 2.5 km range.

We also studied the most significant features observed in time series and frequency distributions of rainrates, C_n^2, vertical air velocities, and spectral width of air signal (all these variables retrieved from VHF Doppler spectra). As before, we eliminate from our analysis those VHF rainfall signals (reflectivities, equivalent reflectivity factors and rainrates) corresponding the equivalent reflectivity factors smaller than 15 dBZ (i.e., rainrates in the order of 0.2 mm/h, in any VHF or X band datasets). Independently from the calibration and signal processing methods discussed in the previous Chapters of this thesis, we also computed the air spectral widths, σ_{AIR}, as a proxy for the time variation of turbulence intensity. The algorithm CURVEFIT by *Research Systems* [2002, p.448-449] was used for this computation, with the input function being a Gaussian curve centered at the vertical air velocity, the input dataset being the air Doppler spectra (i.e., the full VHF spectra minus the rain spectra), and the output being the width (standard deviation) of the Gaussian curve that best fits the input dataset. (The half-power half-width of the fitted Gaussian is then equal to $\sigma_{AIR}\sqrt{2\ln 2}$.) Because in very few occasions this algorithm did not converged to a proper value, we considered only those spectral widths that were positive and smaller than 6 median-absolute-deviations above the median spectral width (the median of σ_{AIR} for the whole event). The results are given in the next section.

We realize that the clear-air Doppler spectra has three main broadening mechanism [e.g., Hocking, 1985]: turbulence broadening (due to turbulence intensity), beam broadening (due to the air motion in the direction parallel to the beam, mainly along the two-way half-power half-beamwidth of the radar pulse), and wind shear broadening (due to wind shear intensity). Our σ_{AIR} values include these effects. [See Hocking, 1983, for calculation examples for typical beam and shear broadening.] Although beam and shear broadening can be dominant features in the middle atmosphere (e.g., Hocking, 1985, p.1415), turbulence broadening seems to be the dominant process in thunderstorms (e.g., Doviak and Zrnic, 1993, p.415). In any case, we will assume that the time variations in our σ_{AIR} values are due mainly to changes in turbulence intensity. The analysis will also assume that the time correlations in our variables of study are equal to the corresponding space correlations; i.e., the Taylor's hypothesis [Taylor, 1938].

We then want to see if the time changes in C_n^2 can be related to corresponding changes in σ_{AIR}. If so, we will conclude that rain affects C_n^2 through dynamic processes (i.e., turbulence). Otherwise, we will conclude that rain thermodynamic processes (the only other possibility) are responsible for the observed changes in C_n^2. There is also a third possibility to consider, that the changes in C_n^2 are not related to precipitation. The analysis will compare the most significant features of C_n^2 observations during rainy and precipitation-free conditions, such that this third possibility can be evaluated.

5.2.3. Validation

We validated the main input for our analysis methods, the VHF retrievals of rain Z_e, by using co-located measurements of precipitation signal at X-band, from the McGill VPR radar. Precipitation attenuation has to be considered for any X band measurement. We then calibrated the VPR measurements by comparing the equivalent reflectivity factors derived from drop-size distributions. For this calibration, we collected measurements of raindrop sizes near the ground, using a Precipitation Occurrence Sensor System [POSS, described by *Sheppard*, 1990] that was co-located with the VPR and the VHF radars. An additional calibration challenge was that some rain accumulated in the radome structure of the VPR radar, especially for intense rainrates; this caused electromagnetic absorption and complicated the relationship between POSS precipitation intensity and VPR received signal. In spite of these complications, we were able to apply this calibration for a particular time interval, between 4:40 and 13:40 UTC on 9 September 2004, where the VPR reflectivities had a roughly exponential (linear in dB) response with POSS reflectivities.

Figure 5.7 presents the time series for simultaneous measurements of equivalent reflectivity factors by POSS (solid line) and VPR (dotted line), for the event on September 9, 2004. The POSS values (Z_{POSS}) correspond to the 10-minute median at a height of about 2 meters (above ground level, agl), while the VPR values (Z_{VPR}) correspond to the 10-minute median at 450 meters agl (the lowest range gate). The time resolution for the POSS dataset is 1 minute, while the VPR time resolution is 30 seconds. We then had to smooth the VPR dataset using the average Doppler spectra in a one-minute moving window. After that, a time lag of 1.5 minutes was subtracted from the POSS observations (already included in Figure 5.7). This time lag is related to a mismatch between the instruments clocks, and its magnitude was determined from the maximum of the cross-correlation function between the Z_{POSS} and the Z_{VPR} time series. The underestimation (due to attenuation) by the VPR is clear. Therefore, a VPR calibration factor, which compensates for the rain attenuation at X band, is obtained from

$$Cal\ .Factor \equiv Median \left[\frac{Z_{POSS}(t_i)}{Z_{VPR}(t_i)} \right] = 3.87 \ ; \tag{5.6}$$

where t_i is the time of the simultaneous observation by the POSS and VPR instruments.

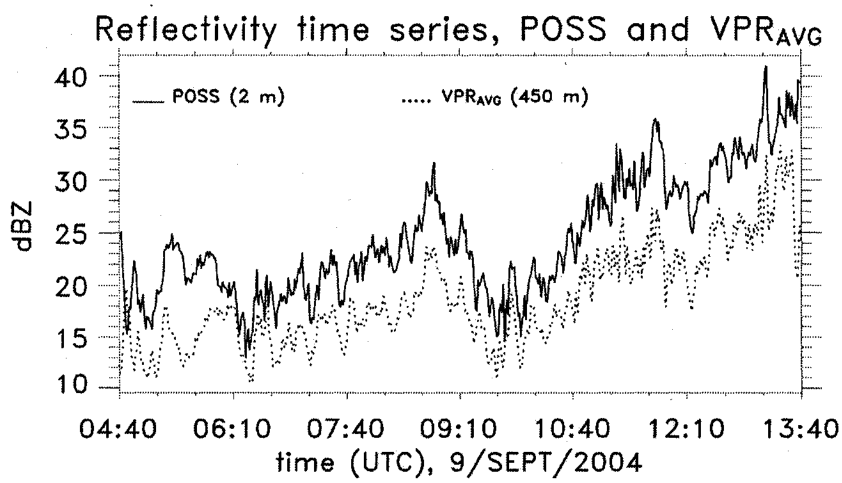

Figure 5.7. Radar reflectivity factors simultaneously measured by the McGill VPR radar (dotted) and the POSS drop size distributions (solid). VPR values correspond to averages over a one-minute moving window. In order to achieve the best match in time for the two datasets, 1.5 minutes have been subtracted from the POSS time series.

Figure 5.8 presents the data from Figure 5.7 as a scatter plot (509 pairs in total). The dashed line corresponds to the hypothetical case when Z_{POSS} and Z_{VPR} would be equal, and the solid line corresponds to the case when the calibration factor in equation (6) is multiplied to Z_{VPR}. Notice how this solid line is located in the observations cluster, which validates the use of equation (5.6) as attenuation corrector. The results of this calibration are given in the time series of Figure 5.9, where the corrected VPR dataset is plotted as the dotted line, and the reference POSS dataset is plotted as the crosses and solid lines.

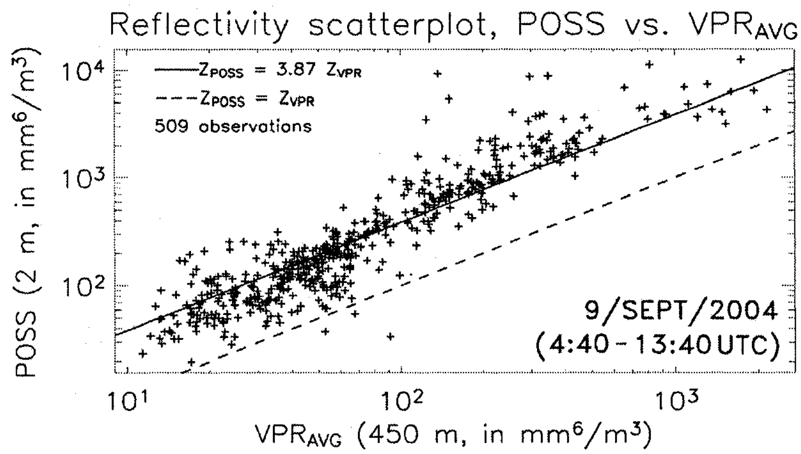

Figure 5.8. VPR calibration using as reference the equivalent reflectivity factors from POSS raindrop sizes.

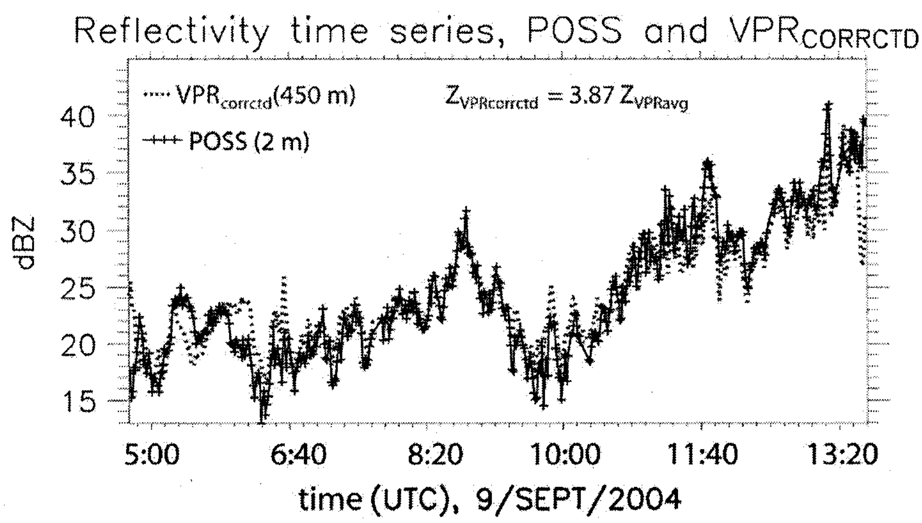

Figure 5.9. Results of VPR calibration for the event on 9 September 2004, from 4:40 to 13:40 UTC.

The comparisons between equivalent reflectivity factors simultaneously obtained at X and VHF bands are presented in Figure 5.10. The Z_e values at X band use the calibration factor in equation (5.6), and the Z_e values at VHF band are from our algorithm to retrieve VHF precipitation signal (already described in

Chapter 3). In order to obtain comparable representativeness from the observations at VHF and X bands, the Doppler spectra at X band were smoothed in range by using the average spectral density within a 500-meter window (i.e., the range resolution of the VHF observations). As well, all the spectra (at VHF and X bands) were smoothed in time by using the median spectral density within a 10-minute moving window. Equivalent reflectivity factors were then computed from these smoothed spectra. We also correct for any time lag that may exist between the two time series (1.2 minutes for this event, due to a mismatch between the instruments clocks), by finding the peak of the cross-correlation between equivalent reflectivity factors at VHF and X, at 2.5 km range. Because of the low correlation between equivalent reflectivity factors at VHF and X bands during extremely weak precipitation, we eliminate from our analysis those VHF rainfall signals corresponding to equivalent reflectivity factors smaller than 15 dBZ (i.e., rainrates in the order of 0.2 mm/h). In summary, Figure 5.11 indicates a very small bias (in the order of 1 dB) and a high correlation coefficient of 0.88 (or 0.80 when dBZ units are used). These agreements validate, once again, the signal processing method described in Chapter 3, as well as the analysis method of this Chapter.

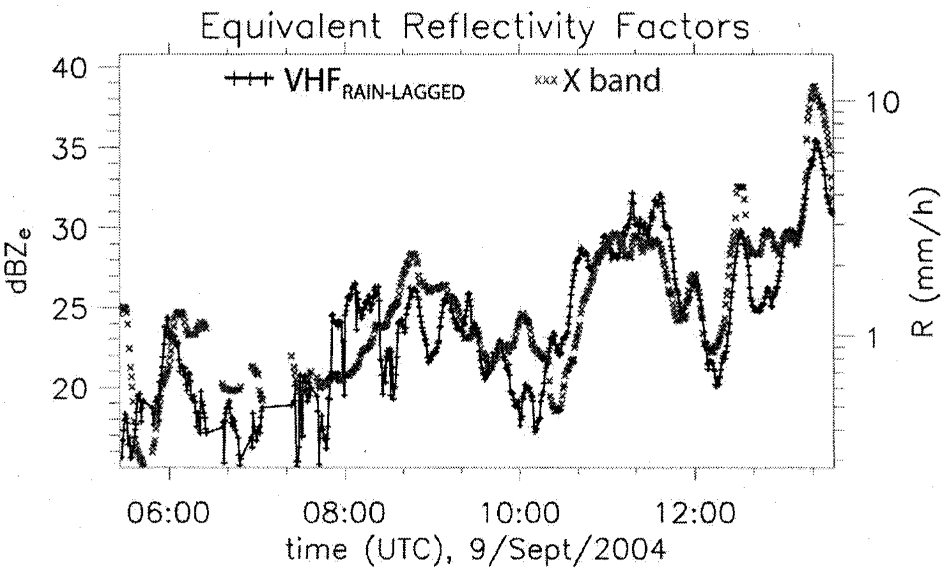

Figure 5.10. Time-series comparison of equivalent reflectivity factors simultaneously measured at VHF and X bands, for the event on 9 September 2004. These time series correspond to 500m-range-mean 10-minute-median smoothing spectra at heights from 2.25 to 2.75 km, using only equivalent reflectivity factors larger or equal than 15 dBZ, and the calibrations in equations (5.6) and (2.27). To compensate for the time lag between the two datasets, 1.2 minutes have been added to the VHF time series.

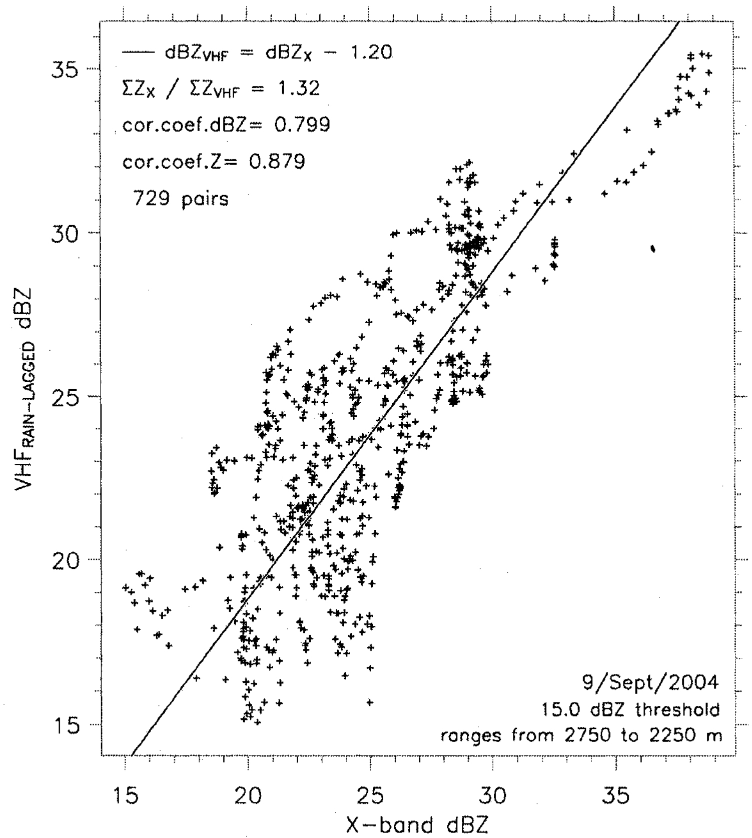

Figure 5.11. Scatter-plot comparison of equivalent reflectivity factors simultaneously measured at VHF and X bands, for the time series in Figure 5.10.

5.3. Results

5.3.1. Profiles

Figures 5.12, 5.13 and 5.14 present Doppler spectra simultaneously measured at VHF and X bands, for three different times during the case on 9 September 2004. For these profiles, the algorithm for extracting the VHF precipitation signal has been applied only for range gates between 2.5 km height (lowest range in the VHF dataset) and the gate corresponding to the melting layer. This is because the algorithm has not been optimized for analysis of solid or partially melted precipitation (e.g., ice or snow). For example notice, in these figures at the heights of the melting layer, the agreement reduction between VHF and X band spectra. Of course, the agreement is much better at the lower heights (within the rain).

We also found several cases where the snow-only spectra can be comparable to the turbulence-only spectra at VHF band. In Figures 5.13 and 5.14, for example, the X band signals at ranges above the melting layer (within the snow) are comparable to the total (air turbulence plus precipitation) VHF signal. Recall also that typical snow fall velocities are comparable to vertical air velocities typically observed in the troposphere. Therefore, some velocity estimates from VHF wind profilers can be biased if snow is present in the radar sampling volume, and if the snow signal has not been excluded from the wind retrieval. The generalization of these implications, however, will require further studies which are beyond the objectives of this Chapter.

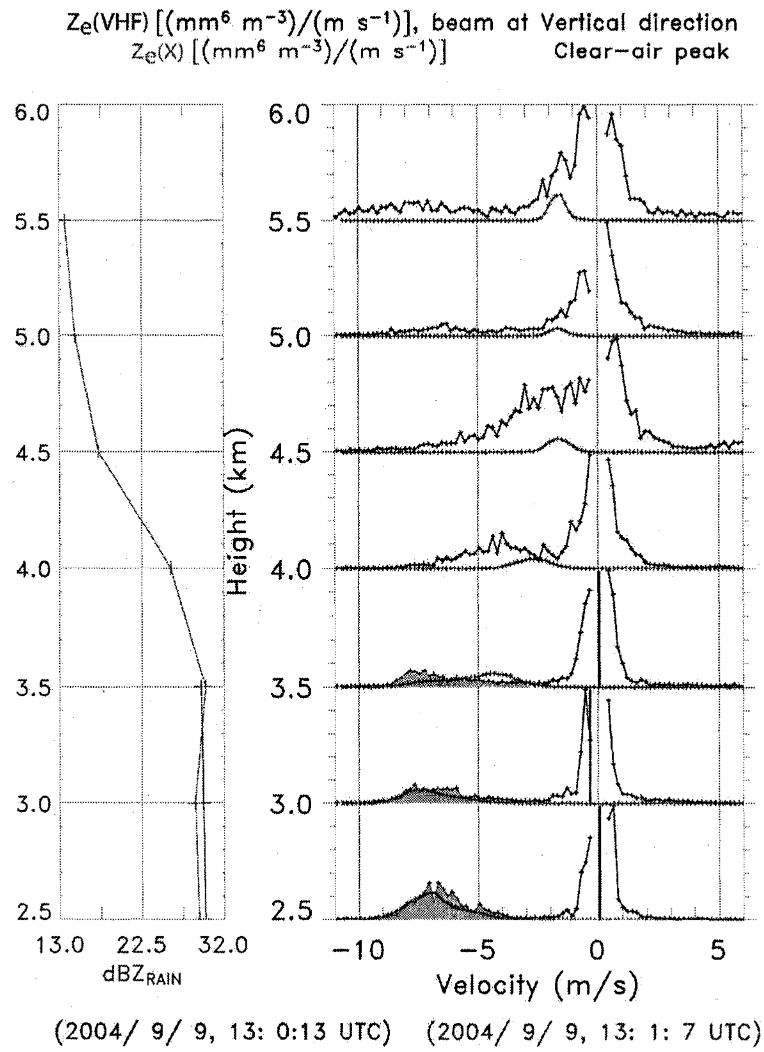

Figure 5.12. Doppler spectra, simultaneously measured at VHF and X bands, on 9 September 2004, at 13 UTC. Right panel: Doppler spectra as a function of height. The VHF dataset is plotted in black and the X band spectra in red. Orange areas correspond to the VHF rain signals. The blue vertical lines correspond to the vertical air velocities. The spectra at each range are normalized in the sense that the maximum spectral amplitude is plotted full-size. Left panel: Integrated Z_e as a function of height for the VHF (in black, from the orange areas in the right panel) and X band (in red) radars. Each spectrum has been smoothed in time using the median of a 10-minute moving window. This particular profile corresponds to the dataset plotted in Figure 5.2.

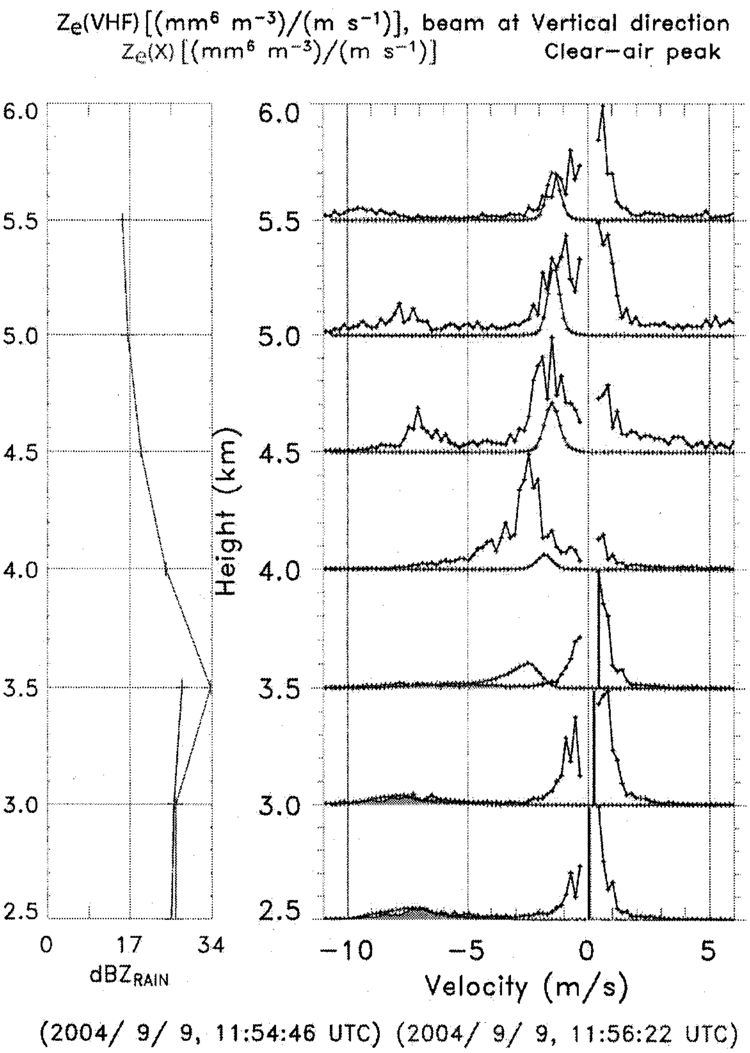

Figure 5.13. As in Figure 5.12 but for 11:55 UTC.

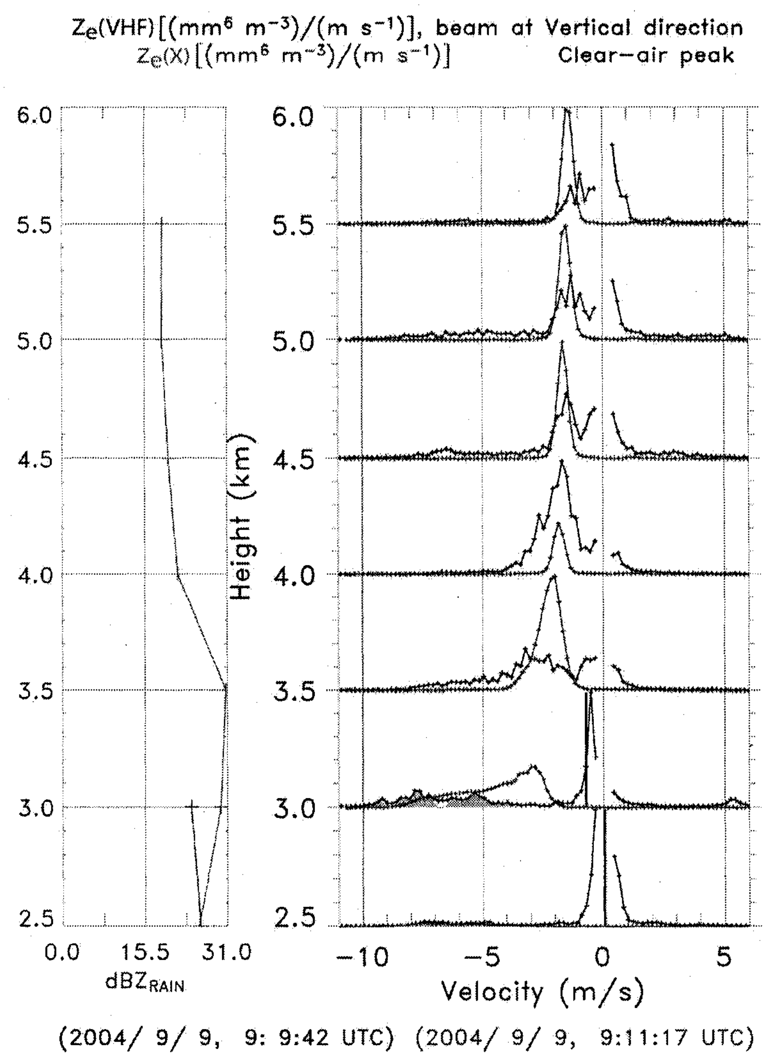

Figure 5.14. As in Figure 5.12, but at 9:10 UTC.

5.3.2. Time series

In addition to the rain event on 9 September 2004, we analyzed also the events on 24 May, 10 August, and 11 August 2004 (from Table 5.1). Figures 5.10 and 5.11 already provided some comparisons between equivalent reflectivity factors measured in the 2.5 km height at VHF (retrieved as in Chapter 3 of this thesis) and X band (as in the dataset from Figure 5.3). Figures 5.15 and 5.16 give the comparisons for the other events. The main outlier points in the scatter plots of these figures (e.g., observations from 14 to 16 UTC, in Figure 5.15) can be associated to the fact that the 2.5 km range is very close to the bright band. It is then likely that the measurements from the VHF radar (having a larger transmitted pulse) would be contaminated. There is also the issue of rain accumulated in the radome structure of the X-band radar. As already mentioned in Section 5.2.3, this produces significant attenuation of the X-band signal for observations during intense rainrates.

As already mentioned in the Methods (section 5.2), our analysis only considers those observation times when Z_e at VHF and X band were greater or equal to 15 dBZ. For the observation times when these conditions were not met, the precipitation reflectivities, equivalent reflectivity factors and rainrates were made equal to zero. As well, spurious observations were eliminated from the analysis by using only those observation times when the air vertical velocity was successfully retrieved by our signal processing method, and when the air spectral width (σ_{AIR}) was positive and smaller than 6 median-absolute-deviations above the median spectral width (the median of σ_{AIR} for the whole event).

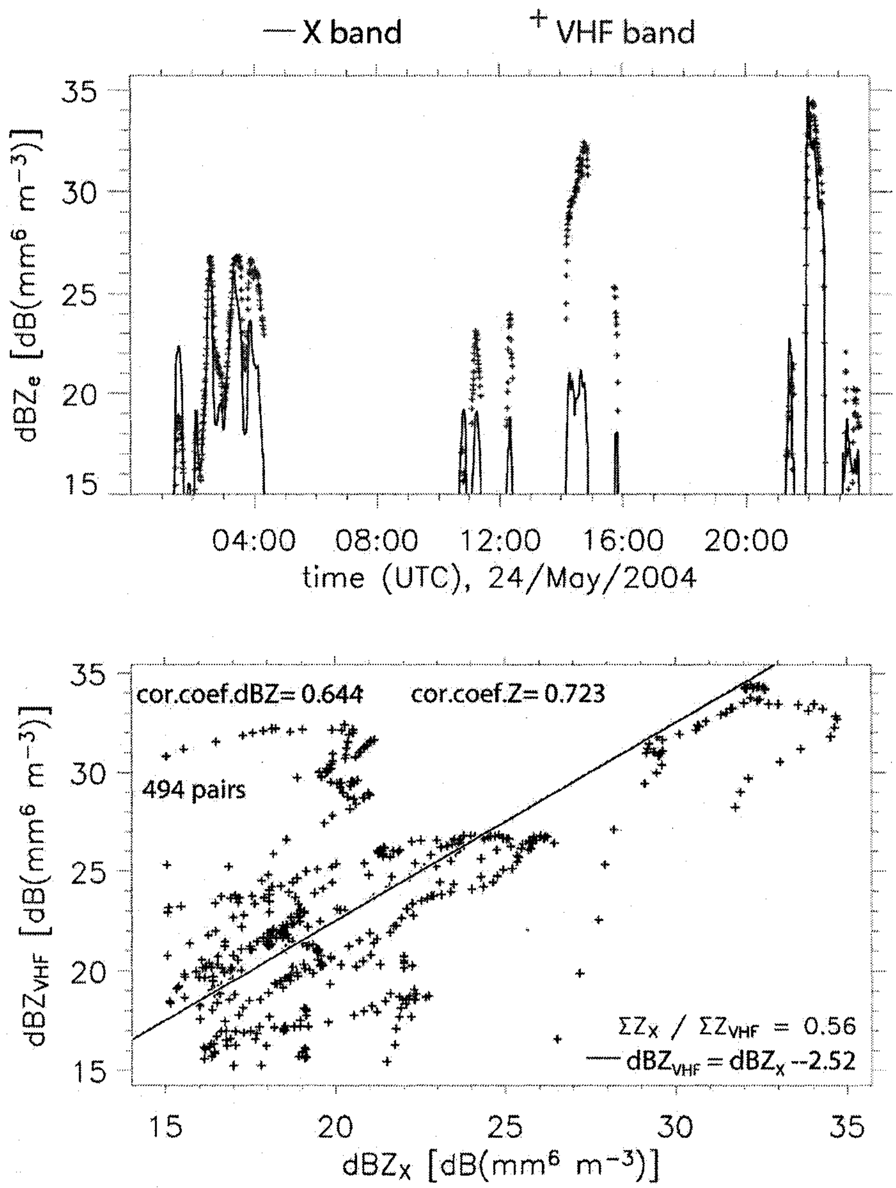

Figure 5.15. Comparison of rain signal at VHF and X band at 2.5 km height, for the events on 24 May 2004 (494 pairs). Upper panel: Time series of equivalent reflectivity factors simultaneously measured at VHF (crosses) and X (solid lines) bands. Lower panel: Scatter plot from the dataset in the upper panel. Correlation coefficients for equivalent reflectivity factors at VHF and X bands are provided. The line corresponds to the best linear fit, where the slope is the accumulated signal at X band divided by the accumulated VHF signal. The X band signal has not been corrected for rain attenuation. Each VHF spectra has been smoothed in time using the median of a 10-minute moving window.

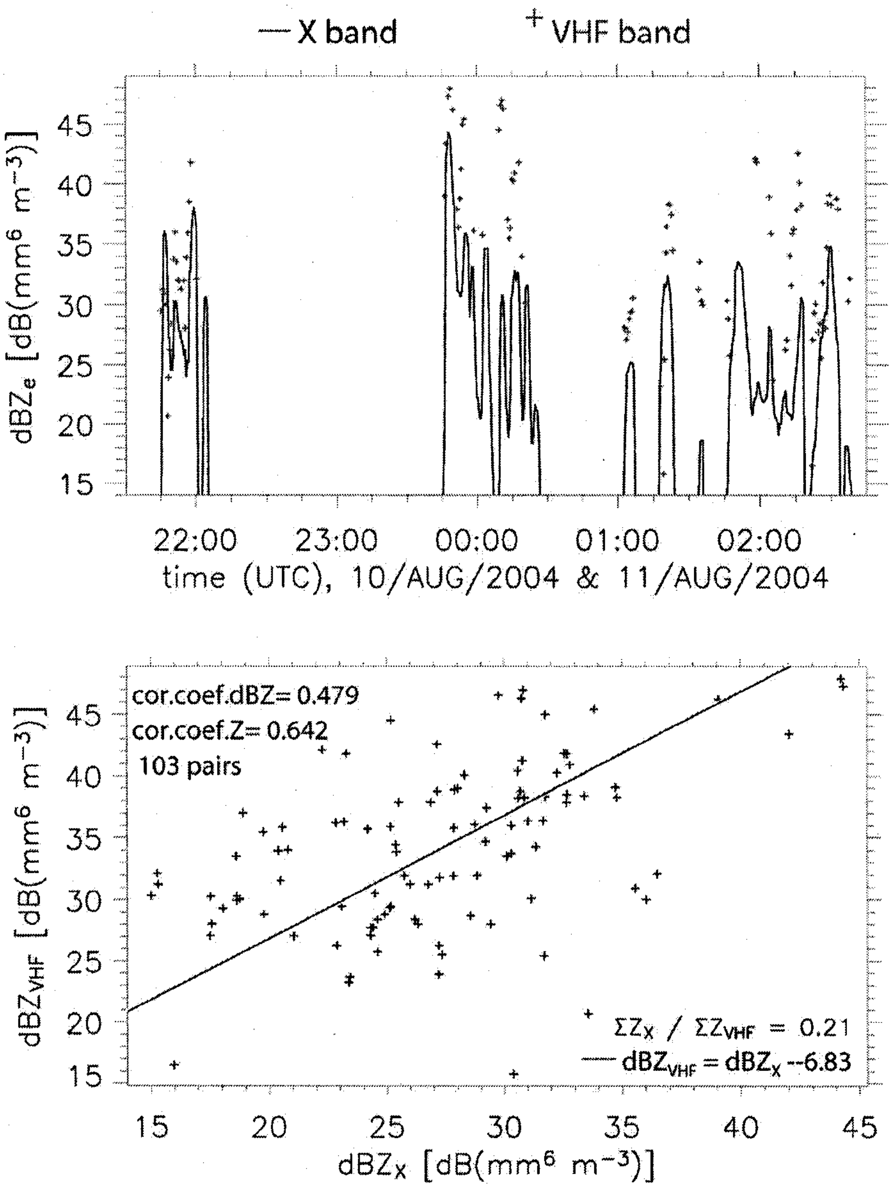

Figure 5.16. As in figure 5.15, but for the events on 10 and 11 August 2004 (103 pairs). Each VHF spectra has been smoothed in time using the median of a 3-minute moving window.

Figures 5.17 and 5.18 present time series of reflectivity η [as defined by equation (3.33)] from air turbulence and precipitation (rain) at 2.5 height, both retrieved from the VHF spectra taken during the events summarized in Table 5.1. From the precipitation reflectivities in these figures, there are 186 cases (about

14% of the 1281 rain observations) where the precipitation reflectivity is equal or larger than the turbulence reflectivity (at vertical incidence). These numbers provide a magnitude for the risk of bias in velocity estimates from VHF wind profilers, when rain is present in the sampling volume, and when the rain signal has not been excluded from the wind retrieval. Recall that the majority of velocity retrieval algorithms (in operational VHF radars) assume that the input Doppler spectra are mainly due to clear-air signals. Therefore, if the input Doppler spectra contain also strong precipitation signals, the retrieved air velocity will be bias towards the precipitation velocity.

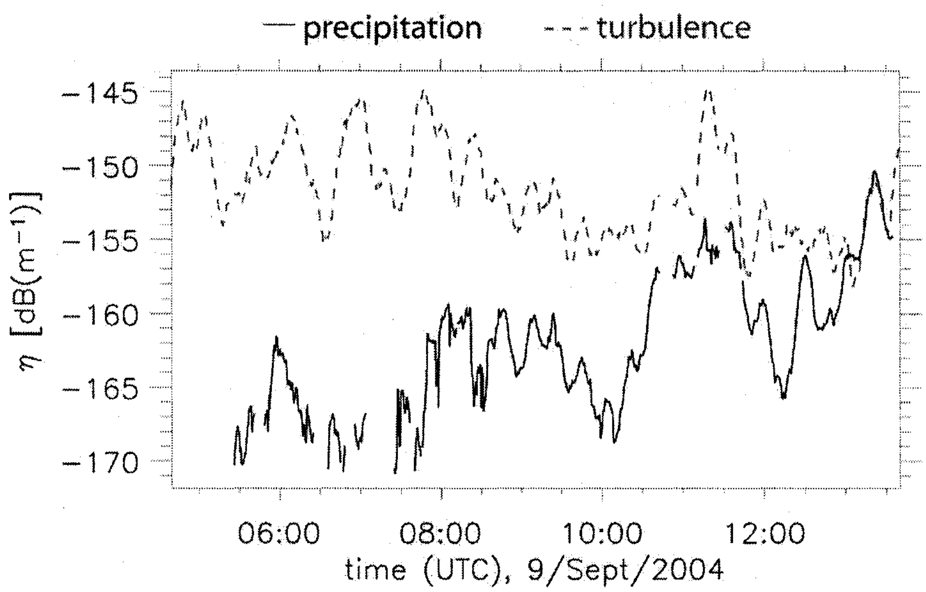

Figure 5.17. Time series of VHF reflectivity from air turbulence (dashed) and rain (solid), at 2.5 km height, for the events on 9 September 2004. For this plot, the precipitation reflectivity is equal or larger than the turbulence reflectivity in about 5.1% (35 spectra) of all the rain observations (684 spectra). Each VHF spectra has been smoothed in time using the median of a 10-minute moving window.

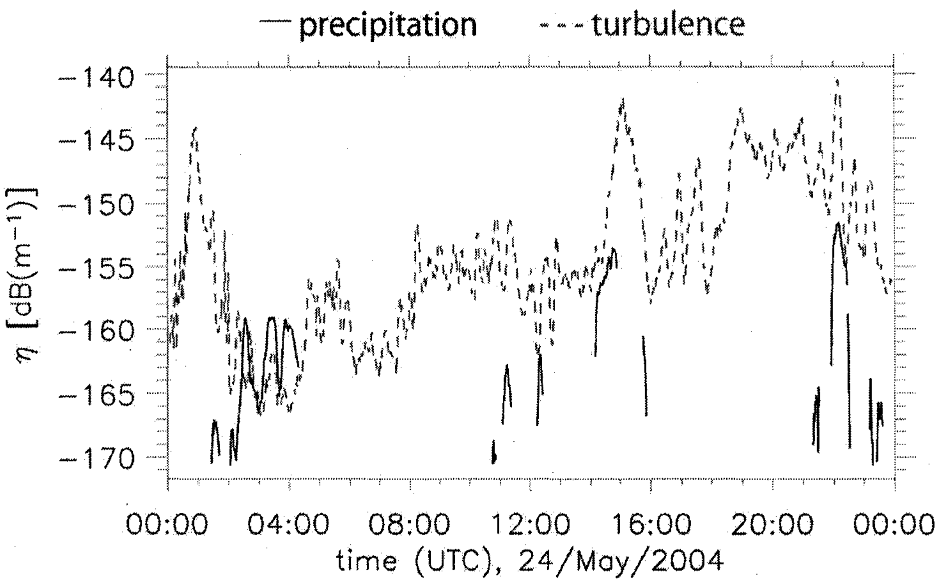

Figure 5.18. As in Figure 5.17, but for the event on 24 May 2004. For this plot, the precipitation reflectivity is equal or larger than the turbulence reflectivity in about 30% (148 spectra) of all the rain observations (494 spectra). Each VHF spectra has been smoothed in time using the median of a 10-minute moving window.

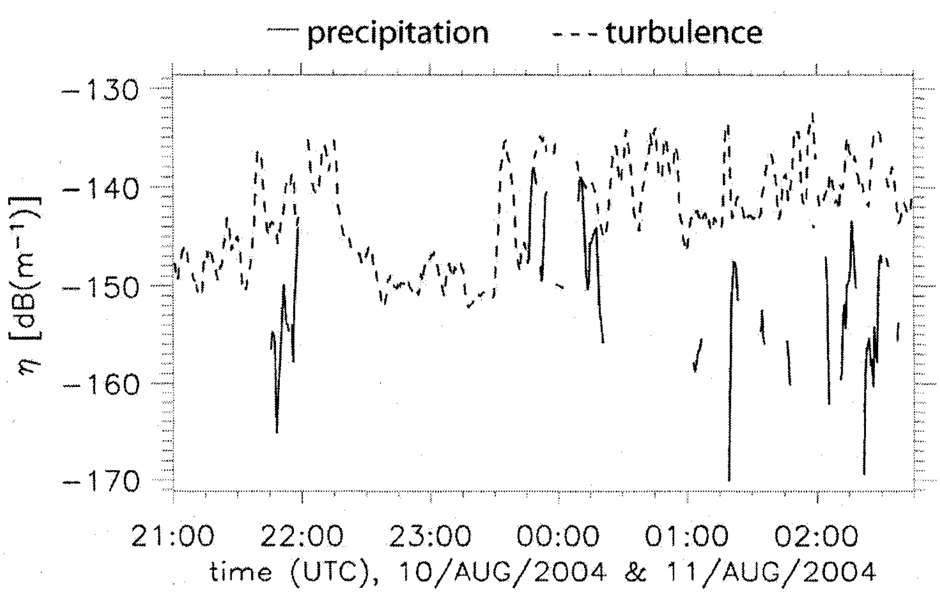

Figure 5.19. As in Figure 5.17, but for the events on 10 and 11 August 2004. For this plot, the precipitation reflectivity is equal or larger than the turbulence reflectivity in about 2.9% (3 spectra) of all the rain observations (103 spectra). Each VHF spectra has been smoothed in time using the median of a 3-minute moving window.

For the datasets summarized in Table 5.1, Figures 5.20, 5.21 and 5.22 present time series of rainrate, C_n^2, vertical air velocity, and spectral width of air signal (σ_{AIR}). Observations such as the ones on 24 May 2004, from 14 to 16 UTC (Figure 5.21), reveal cases of clear correlation between C_n^2 and rainrate. Notice also the observations on 9 September 2004 from 10:30 to 12 UTC (Figure 5.20), here the increasing values of C_n^2 are correlated with increasing values in σ_{AIR}. This implies that turbulence is associated to the time variations of C_n^2. In other cases, like during the stratiform rain from 2 to 5 UTC on 24 May 2004 (Figure 5.21), there is a large value of C_n^2 just before the occurrence of rain. In this case, C_n^2 and σ_{AIR} start to decrease as rain starts to happen. Again, this implies that turbulence is driving the time variations of C_n^2.

Table 5.2. Correlation coefficient between C_n^2 and σ_{AIR}, for the datasets plotted in Figures 5.20, 5.21, 5.22 and 5.23. Notice the small dynamic range of C_n^2 during the event on 9 September 2004, which contributes to the low correlation values for this period.

Event	Correlations during entire period	Correlations only during rainy period
24 May 2004 (stratiform rain)	0.23 (1052 pairs)	0.28 (494 pairs)
10 August 2004 (without precip.)	-0.13 (231 pairs)	
10-11 August 2004 (convective rain)	0.54 (213 pairs)	0.28 (103 pairs)
11 August 2004 (without precip.)	-0.45 (1168 pairs)	
8 September 2004 (without precip.)	-0.26 (1276 pairs)	
9 September 2004 (stratiform rain)	0.05 (1171 pairs)	0.01 (684 pairs)

Notice in Table 5.2 that the correlation coefficients between C_n^2 and σ_{AIR} (computed for periods of several hours) are low. This is because thermodynamic processes are also able to change C_n^2. See for example the rain event occurring near 22 UTC on 24 May 2004 (Figure 5.21). Here the increasing values of C_n^2 are accompanied by decreasing values of σ_{AIR}. Since the energy dissipation rate [the term ε in equation (5.1)] is a function of the spectral width σ_{AIR}, then C_n^2 should also be correlated with σ_{AIR}. Therefore, for this particular rain event, the effects of turbulence are excluded as the main driving mechanism for the C_n^2 time variation. This also leads to the other only possible explanation for the changes in C_n^2, i.e., thermodynamic processes that increase the temperature and humidity gradients. In any case, our observations show a tendency towards higher correlations between C_n^2 and σ_{AIR} for the higher rainrates (e.g., the correlation in Table 5.2 for the convective-rain environment in Figure 5.22).

Rogers et al. [1994, p. 539] suggested that the effect of rain for turbulence scattering would be simply a *reduction* in C_n^2 caused by a smoothing of the humidity gradients. We observe similar conditions in Figure 5.20, for the rain event occurring from 8 to 10 UTC, when a decrease of C_n^2 is not accompanied by any change in σ_{AIR} (this leaves the explanation for the C_n^2 changes to thermodynamic processes only). There are, however, other observations in which C_n^2 *increases* thermodynamically. See for example Figure 5.20 and the rain event occurring from 5:30 to 6:30 UTC; here C_n^2 increases but the σ_{AIR} values stay around the same magnitude.

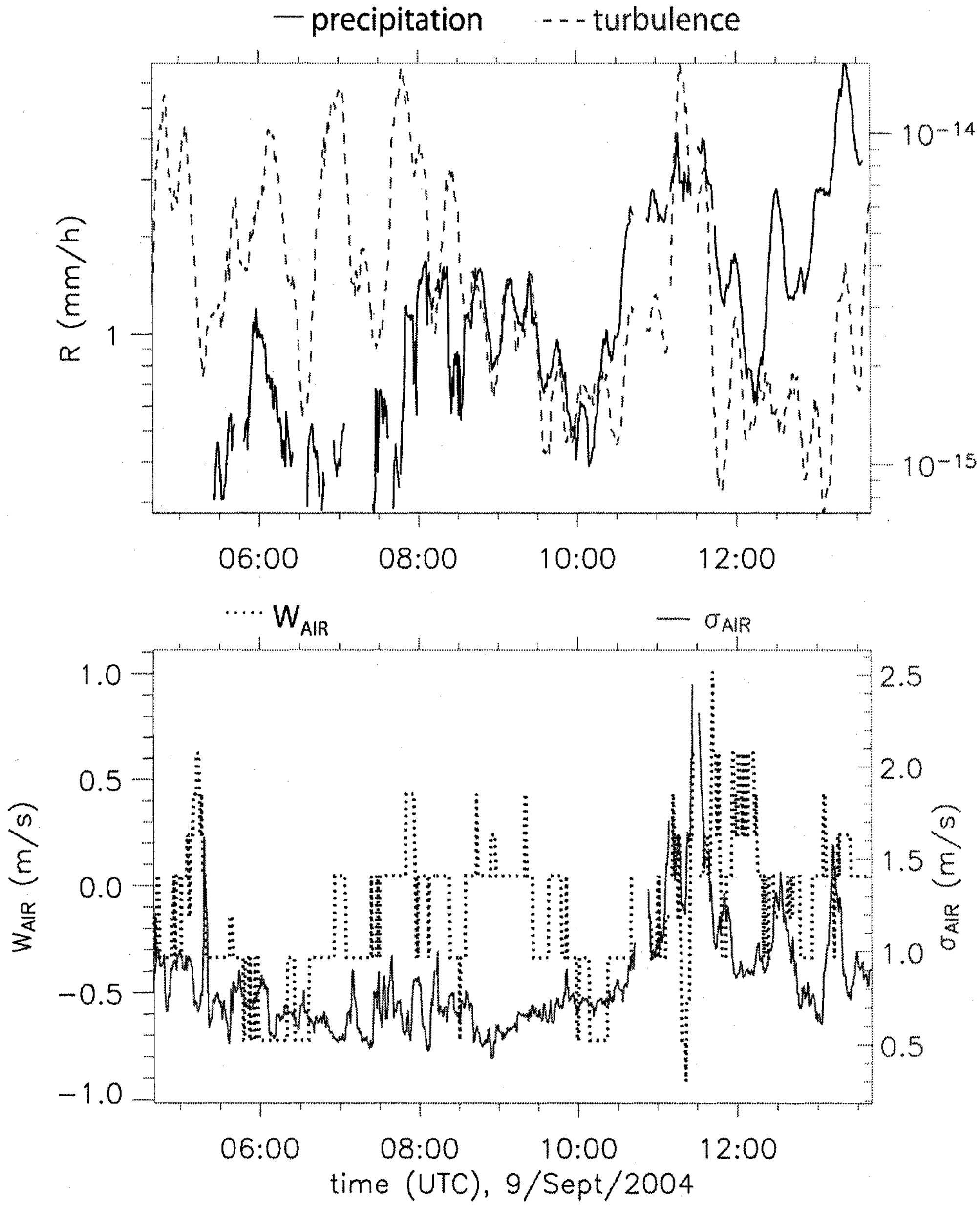

Figure 5.20. Time series of precipitation and air-turbulence variables obtained from VHF spectra at 2.5 km height, for the events on 9 September 2004. Upper panel: Rainrate (solid lines, scale on the left Y-axis) and C_n^2 (dashed lines, scale on the right Y-axis). Lower panel: vertical air velocity (dotted stepped lines, scale on the left Y-axis) and spectral width of air signal (solid lines, scale on the right Y-axis). Each VHF spectra has been smoothed in time using the median of a 10-minute moving window.

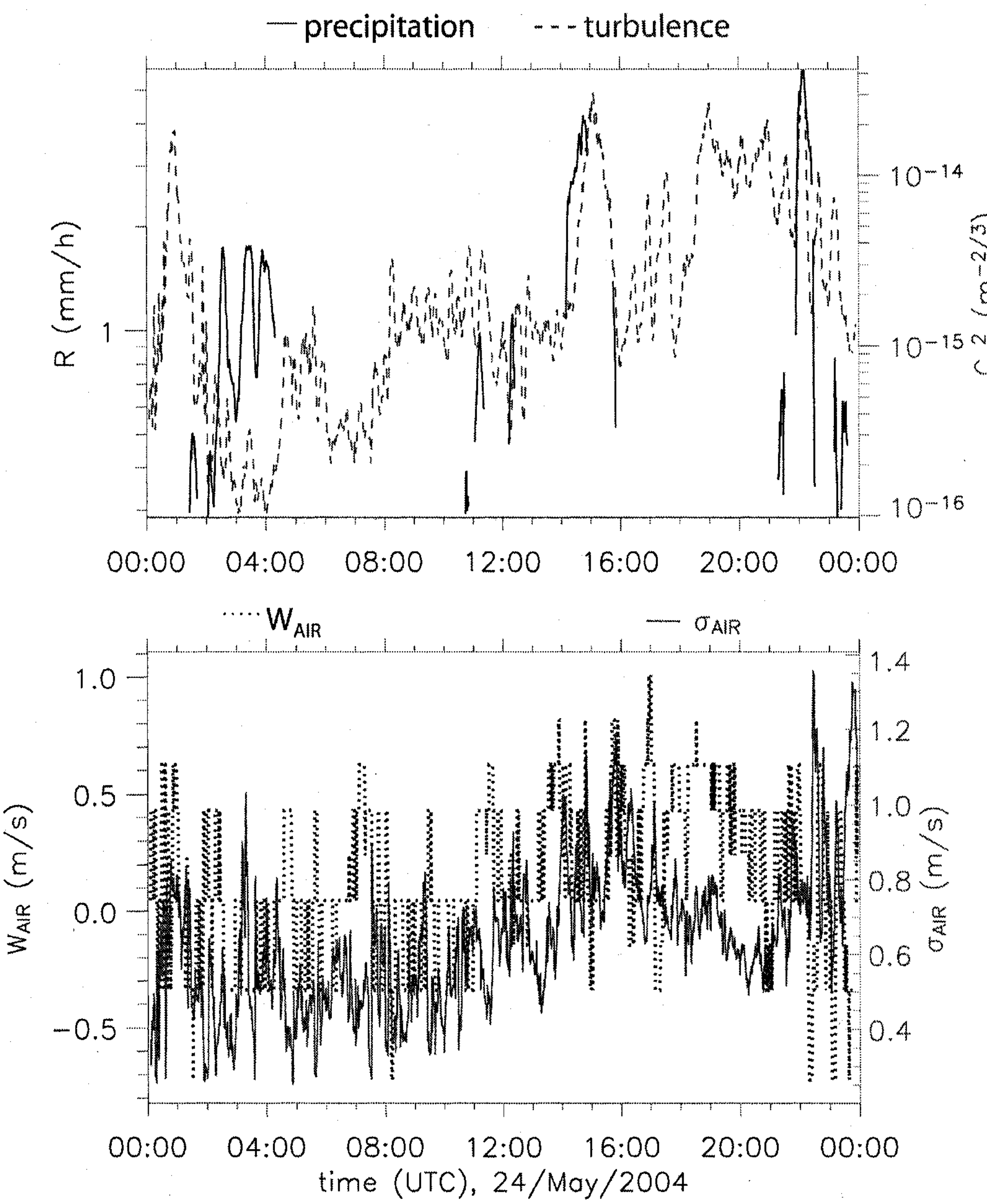

Figure 5.21. As in Figure 5.20, but for the rain events on 24 May 2004.

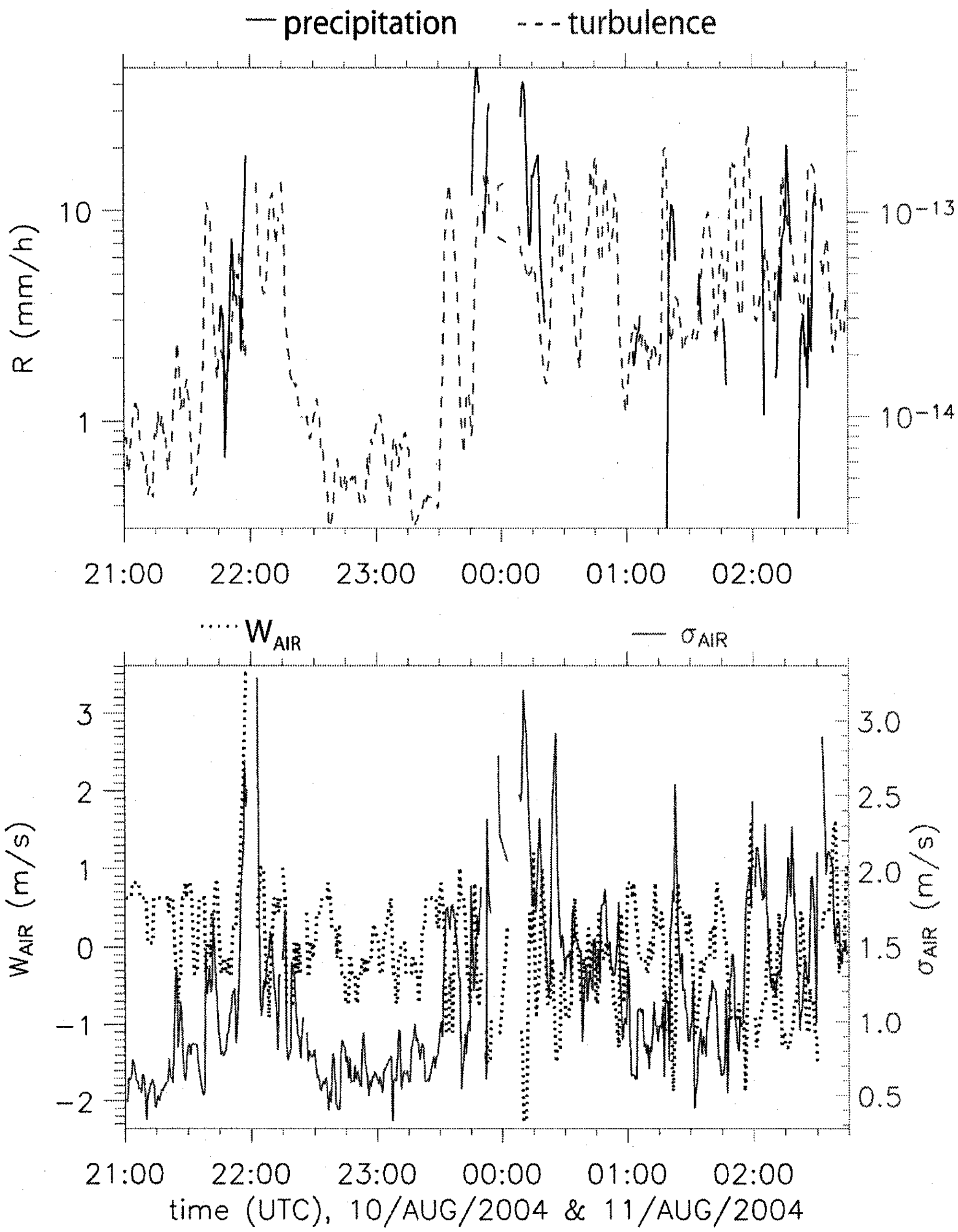

Figure 5.22. As in Figure 5.20, but for the rain events on 10 and 11 August 2004. Each VHF spectra has been smoothed in time using the median of a 3-minute moving window.

Analyses in precipitation-free environment are also presented in Figure 5.23. These observations correspond to time series of C_n^2 (dashed lines) and σ_{AIR} (solid lines), retrieved from VHF spectra, for periods before or after the precipitation events in Table 5.1. For the periods plotted in Figure 5.23, we verify that no precipitation echo was detected by the X-band VPR radar. We also checked observations by the McGill, S-band weather radar (reflectivity factor observations at 2.5 km height), to make sure that the environment around the VHF radar was free from precipitation within a range of 30 to 60 kilometers. The most relevant features observed in Figure 5.23 are perhaps the sharp short-time variations of C_n^2 with time. Comparing the C_n^2 time series for rainy and precipitation-free environments, we can also deduce that rain makes the C_n^2 time variations smoother than during precipitation-free conditions. The correlation coefficients between C_n^2 and σ_{AIR} for these precipitation-free environments are included in Table 5.2. These correlations are all negative, which indicates that changes in turbulence is not driving the C_n^2 variations during these particular periods.

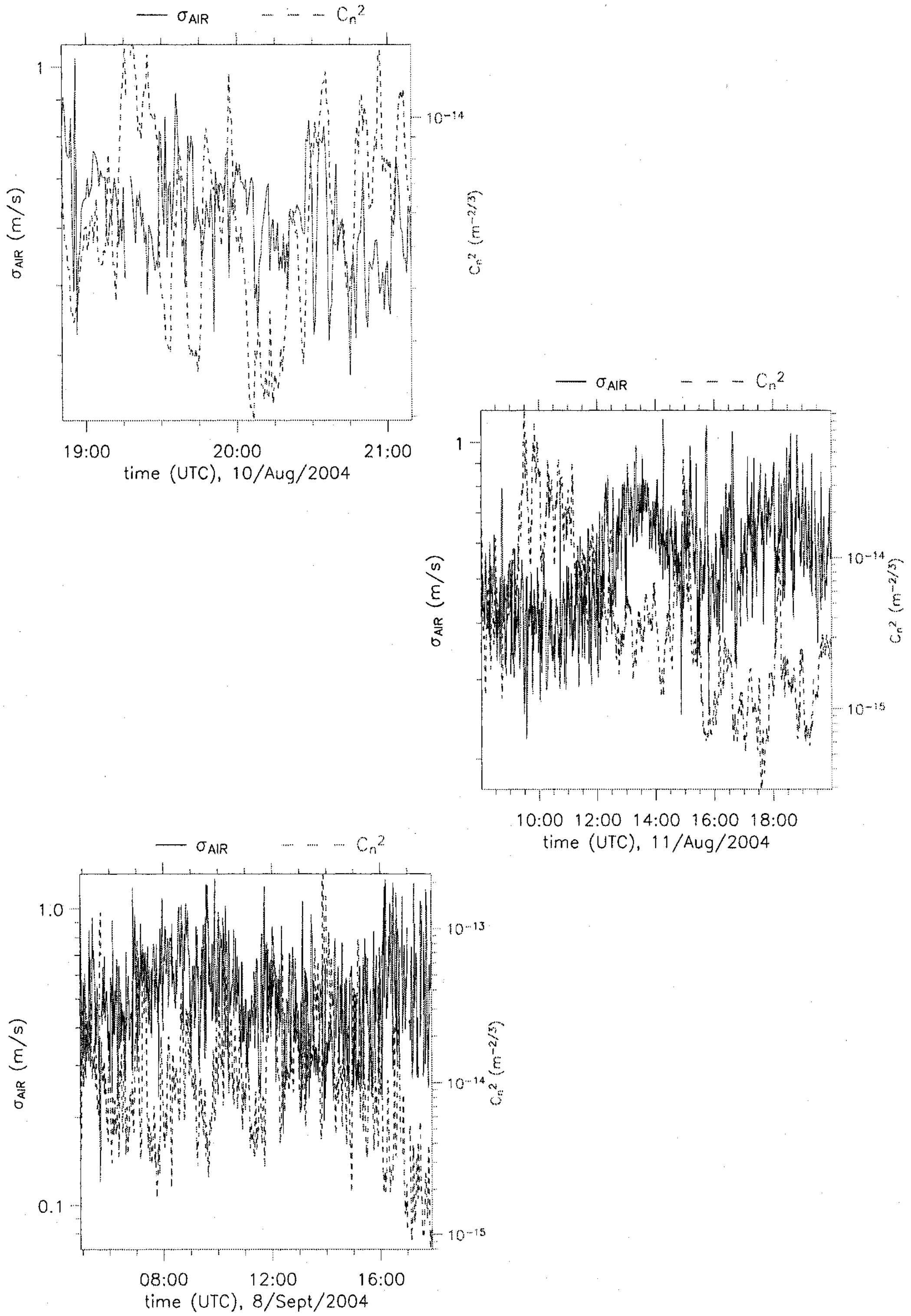

Figure 5.23. Time series for the spectral width of air signal (solid lines, scale on the left Y-axis) and C_n^2 (dashed lines, scale on the right Y-axis), for three precipitation-free environments. Each VHF spectra has been smoothed in time using the median of a 3-minute moving window.

5.3.3. Frequency distributions

Figures 5.24, 5.25 and 5.26 present the frequency distributions for the corresponding dataset plotted in Figures 5.20, 5.21 and 5.22. This time, however, the analyses also exclude any clear-air signal for those observation times when Z_e at VHF and X band are smaller than 15 dBZ. For the rainrates analyzed here (between 0.3 and 78 mm/h), and for our radar sampling volume (per unit time) of 2.3×10^5 m^3 s^{-1} (corresponding to a two-way half-power half-beamwidth of 1.6°, and a range gate between 2.25 and 2.75 km height), the vertical velocities were found between -2.3 and 3.7 m/s, while the air spectral width lay between 0.3 and 3.3 m/s. As well, the C_n^2 values lay in the range between 10^{-16} and $10^{-12.2}$ m$^{-2/3}$. In comparison, *Chilson et al.* [1993, p.665] mention that C_n^2 values between 10^{-15} and 10^{-13} m$^{-2/3}$ are representative of moderate and severe turbulence to be found in a thunderstorm. Similarly, *Ralph* [1995, p. 258] categorizes as high C_n^2 values those measurements between 10^{-15} and 10^{-13} m$^{-2/3}$, and as extreme C_n^2 values those observations larger than 10^{-13} m$^{-2/3}$. Some of these extreme C_n^2 values are present in our dataset, particularly during the convective rain on 10 and 11 August 2004 (right upper plot in Figure 5.26).

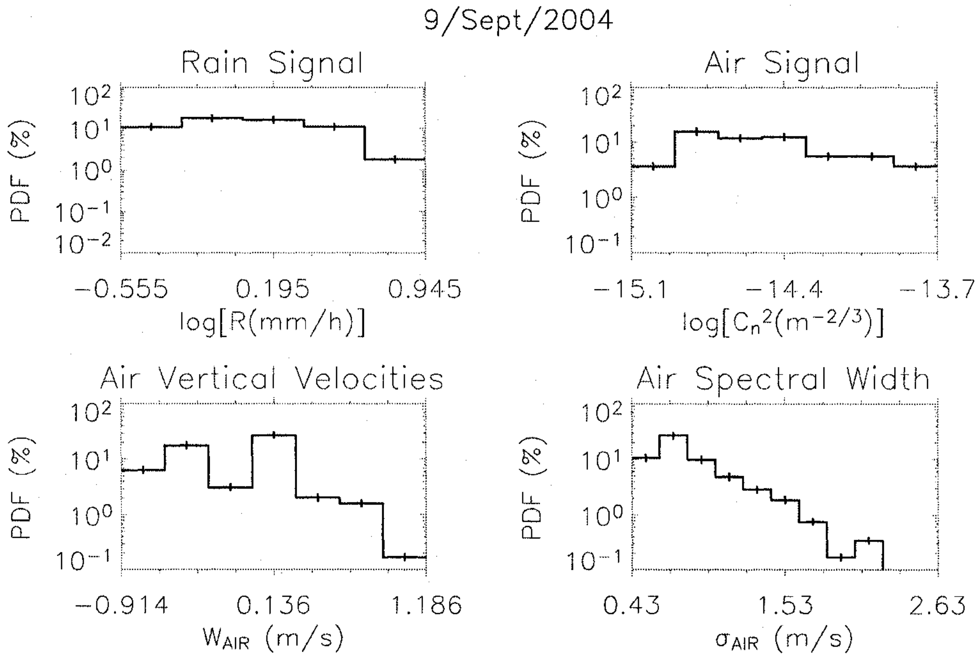

Figure 5.24. Frequency distributions for rainrate, C_n^2, vertical air velocity, and spectral width of air signal, at 2.5 km height, for the events on 9 September 2004. A total of 684 VHF spectra were analyzed during times at which the VHF and X band signals were larger than 15 dBZ.

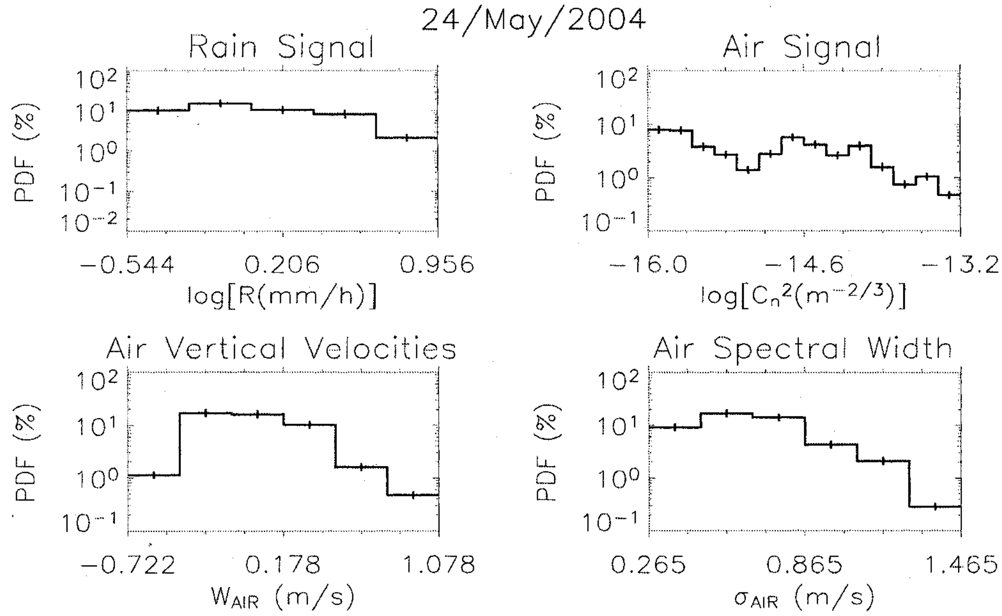

Figure 5.25. Frequency distributions for rainrate, C_n^2, vertical air velocity, and spectral width of air signal, at 2.5 km height, for the events on 24 May 2004. A total of 494 VHF spectra were analyzed during times at which the VHF and X band signals were larger than 15 dBZ.

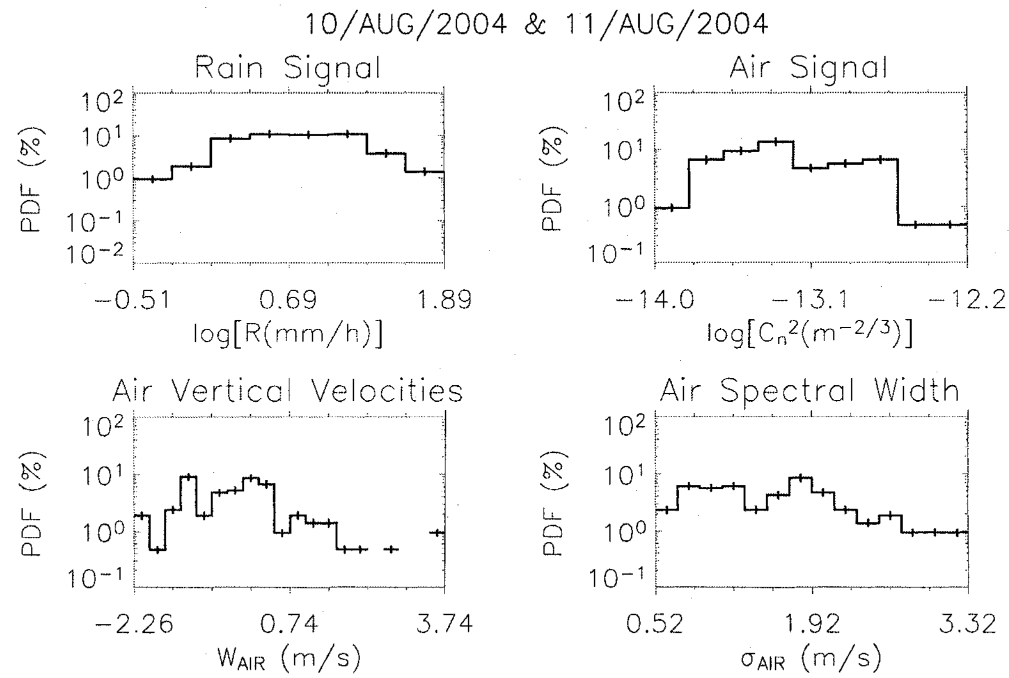

Figure 5.26. Frequency distributions for rainrate, C_n^2, vertical air velocity, and spectral width of air signal, at 2.5 km height, for the events on 10 and 11 August 2004. A total of 103 VHF spectra were analyzed during times at which the VHF and X band signals were larger than 15 dBZ.

5.4. Discussion

Our observations indicate that rain actually affects the structure of air refractive index. These C_n^2 fluctuations are smoother than in precipitation-free conditions, and can be due to changes in turbulence intensity, moisture amounts, or temperature fields. Although dynamic processes (turbulence) were dominant for the most intense rainrates, the spectral width of air signal did not always changed with C_n^2. This indicates that thermodynamic effects (moisture and temperature) are also capable of generating significant changes in the structure of air refractive index.

For a total of 1281 VHF spectra measured in rain, our observations show a tendency towards more dynamically driven changes in C_n^2 (higher correlations between C_n^2 and σ_{AIR}) for the higher rainrates. They also identify cases when rain thermodynamic processes lead to either increases or decreases in C_n^2.

The analyses in this Chapter include events free of precipitation, as well as events of convective and stratiform rain, all typical of continental mid-latitude conditions. The measured rainrates are distributed between 0.3 and 78 mm/h, and the C_n^2 values lay in the range between 10^{-16} and 10^{-12} $m^{-2/3}$. The study focuses on observations at 2.5 km height, including time series and frequency distributions that can be used in future work as characteristic magnitudes for continental mid-latitude rain.

The study shows that some (up to 30 %, e.g., Figure 5.18) velocity estimates from VHF wind profilers are in risk of being biased, if precipitation is present in the radar sampling volume, and if the precipitation signal has not been excluded from the wind retrieval. The generalization of these implications, however, will require further studies which are beyond the objectives of this Chapter.

As a following step in this research line, it is recommended to study the vertical profiles of C_n^2 in precipitation, using the same analysis techniques presented here. It will be also recommended to determine ε directly, and use it in the analyses instead of σ_{AIR}. This approach will require to know the wind profile (to compute the turbulence spectral width) and the vertical profiles of temperature and moisture [to compute the term M in equation (5.1)], all above the VHF radar. As a result, our analysis techniques in combination with radio sounding observations would lead to a refined understanding of the particulars by which precipitation modifies the structure of air refractive index.

CHAPTER 6:

SUMMARY AND CONCLUSION

This work focused on the following questions: How can we use VHF radar as an operational tool for the study of precipitation physics? What are the typical backscatter signals that rain and turbulence produce at VHF band during precipitation events? To address these questions, this work takes advantage of the unique potential that VHF radars have for simultaneously measuring air vertical velocity and precipitation intensity. We collected and analyzed a unique dataset of simultaneous and collocated measurements by the McGill VHF radar [described by *Campos and Hocking*, 2003], by the McGill X-band vertically-pointing radar [described by *Zawadzki et al.*, 2001], and by a McGill POSS instrument [described by *Sheppard*, 1990]. All these measurements were taken over Montreal (Lat. 45.41°N, Long. 73.94°W), for selected cases during the Spring, Summer and Fall of 2004.

There are four basic requirements in order to typify precipitation and turbulence signals at VHF. First, we require a detailed review to the radar calibration process. Second, we need to develop a signal-processing algorithm that allows the automatic separation of precipitation and clear-air signals. Third, we must apply this algorithm in an efficient analysis of large radar datasets taken during rain. Fourth, we must generate statistics of Z and C_n^2 values observed in the Montreal region. Accomplishments of these basic requirements are the four specific objectives of this research.

Chapter 2 presented an integrated, multi-faceted approach to calibrate VHF radars, using noise-generator calibration and sky-noise calibration methods, and intelligent integration of the methods. In addition, our calibration approach allows derivation of several antenna and receiver parameters and their corresponding uncertainties. We gave these parameters for the McGill VHF radar in Table 2.2. The application of our calibration technique to the McGill VHF radar measurements allowed us to generate calibrated power spectra (such as the one in Figure 2.15). Another advantage of our calibration technique is that, once the noise-generator part has been applied, the rest of the calibration can be performed during routine observations (without the need for additional hardware or modification of the radar operation). Furthermore, a change in the radar hardware does not require a new noise-generator calibration.

Regarding the applicability of the calibration method (in Chapter 2) to vertically-pointing radars operating at shorter wavelengths (e.g., at UHF band), equation (2.5) indicates that the sky-noise signal received by a 0.75m-wavelength (400 MHz) radar is only 0.006 times the sky-noise signal at 5.77m wavelength (the 52 MHz used here). This is a 22 dB reduction. Therefore, the application will be limited by the sensitivity of the shorter-wavelength radar for detecting such weak signals.

Chapter 3 extends the operational capabilities of the VHF radar to measure precipitation intensity (in units of $mm^6\ m^{-3}$) in addition to air velocity. To accomplish this, we presented the mathematical derivation of the VHF radar equation. We have also validated the assumption that $|K|^2$ is 0.93 ± 0.01 for rainfall measured by VHF radars. In addition, we provided an efficient method for extracting the precipitation signal out of VHF Doppler spectra.

The signal processing algorithm for Doppler-spectra separation of air and rain signals (in Chapter 3) can be easily applied to radars operating at shorter wavelengths. We would expect the air and rain signals to behave according to the curve slopes in Figure 1.2. The data collected in Chapter 5 show that C_n^2 values of 10^{-13} $m^{-2/3}$, and precipitation reflectivities of 30 dBZ, are common. Therefore, the rain signal would be stronger than the air-turbulence signal only by about 10 or 20 dB. However, the algorithm described in Chapter 3 may require minor changes when applied to different precipitation regimes, such as tropical environments, with larger turbulence signals and stronger vertical motions. In these cases, we may need to empirically adjust equation (3.40) and the spectral range where we search for the clear-air peak.

We validate our analysis methods using time series of equivalent reflectivity factors simultaneously obtained by our VHF radar, by our X-band radar, and by our POSS sensor (all instruments were co-located with a separation of a few tens of meters). We computed the correlation coefficient between Z_{POSS} and Z_{VHF}, finding a value of 0.82 (0.76 for the reflectivity factors expressed in dBZ). We also found that the VHF reflectivity-factors are about 4 dB lower than the reference POSS values. (This is not a large difference considering the fact that the measurements from these instruments do not represent exactly the same volume in space.) Using our X-band vertically-pointing radar, we verified that the differences between Z_{VHF} and $Z_{X\text{-}band}$—when using similar sampling volumes—are in the order of 1 dB. A high correlation coefficient of 0.88 (or 0.80

when dBZ units are used) were obtained between Z_{VHF} and $Z_{X\text{-}band}$. These small biases and high correlation coefficients validate our entire analysis methods.

In Chapter 4, we explored the validity of our general radar equation to compute profiles of radar reflectivity factor, for conditions of space-variable reflectivity and with an antenna pattern of non-negligible sidelobes. We simulated the precipitation signal in the VHF radar by combining X-band signals (at high range resolution) and the VHF antenna pattern into a general version of the radar equation. The simulated precipitation signal at VHF compares well with actual measurements by the VHF radar, and this validates our analysis methods. Our analysis indicates that VHF reflectivity at gates above the melting layer is artificially enhanced by the precipitation signal collected in the side-lobe direction. An idea to reduce the problem of side-lobe contamination by the bright band is to redesign the configuration of the antenna array (for smaller sidelobes in the antenna pattern).

Chapter 5 addresses the question on what effect the precipitation has on the scattering properties of the clear air. Our analysis indicates that rain actually affects the structure of air refractive index. These C_n^2 fluctuations are smoother than in precipitation-free conditions, and can be due to changes in turbulence intensity, moisture amounts, or temperature fields. Although dynamic processes (turbulence) were dominant for the most intense rainrates, the spectral width of air signal did not always changed with C_n^2. This indicates that thermodynamic effects (moisture and temperature) are also capable of generating significant changes in the structure of air refractive index.

As a following step in this research line, it is recommended to study the vertical profiles of C_n^2 in precipitation, using the same analysis techniques presented here. It will be also recommended to determine ε directly, and use it in the analyses instead of σ_{AIR}. This approach will require to know the wind profile (to compute the turbulence spectral width) and the vertical profiles of temperature and moisture [to compute the term M in equation (5.1)], all above the VHF radar. As a result, our analysis techniques in combination with radio sounding observations would lead to a refined understanding of the particulars by which precipitation modifies the structure of air refractive index.

In conclusion, this work extends the operational capabilities of VHF vertically-pointing radars by including the rainfall quantification in addition to the wind measurement. As well, the study shows how rain actually affects the scattering properties of clear air.

APPENDIX:

THE RADAR EQUATION

To begin the derivation of our radar equation, we considered a hypothetical monostatic, vertically pointing, VHF radar. Figure A1 depicts this radar during transmission.

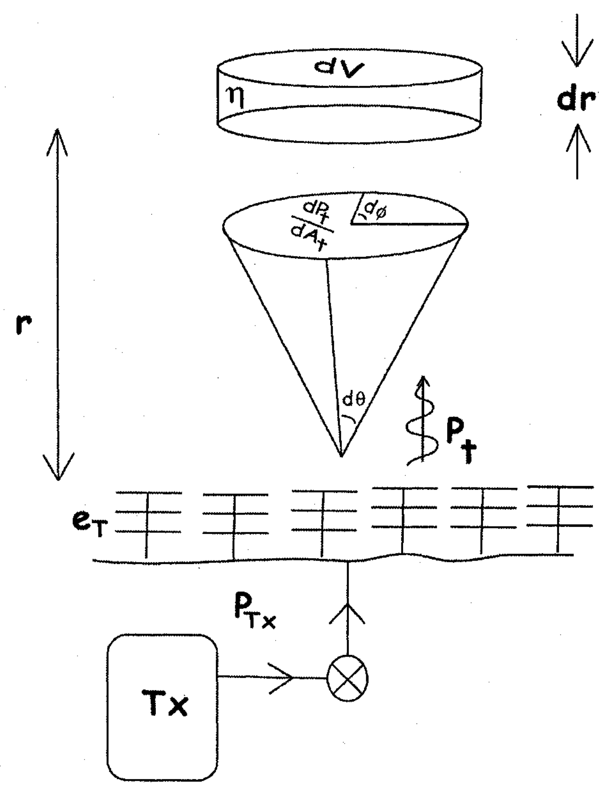

Figure A1. VHF radar during transmission.

For an isotropic radar antenna, the transmitted power flux within a small and finite area (perpendicular to the radiation direction) is given by

$$\frac{dP_t}{dA_t} = \frac{P_t}{4\pi\, r^2}\ ; \tag{A1}$$

where P_t is the total power transmitted by the antennas towards the space, r is the range, and dA_t is the finite area perpendicular to the radiation direction. Recall that equation (A1) gives the power flux density per unit area, also called intensity of radiation. However, for a real antenna, we have that the power flux is given by

$$\frac{P_t}{dA_t} = \frac{P_{Tx}\, e_T}{4\pi\, r^2}\, D(\theta,\phi) \; ; \tag{A2}$$

where P_{Tx} is the power input into the antennas by the transmitter hardware, and e_T is the antenna efficiency. D is the directivity (as a function of azimuth ϕ and zenith θ), and it is given as the ratio between the power flux transmitted by the real antenna and the power flux that an ideal isotropic antenna would transmit, i.e. [e.g., *Ulaby et al.*, 1981, p.102, equation (3.22)]:

$$\frac{\frac{dP_t}{dA_t}(antenna)}{\frac{dP_t}{dA_t}(isotropic)} \equiv D(\theta,\phi) = D_{\max}\; F(\theta,\phi) \; ; \tag{A3}$$

where F is the normalized (i.e., its maximum value is one) one-way polar diagram (or antenna pattern), and D_{max} is the maximum directivity (i.e., the D value when the zenith angle is equal to the radar beam direction).

During backscattering of the radar transmitted pulse (Figure A2), we have that the scattered power from targets contained in a volume V (i.e., the sampling volume) is given by

$$dP_s = \frac{dP_t}{dA_t}\, dA_s \; ; \tag{A4}$$

where dP_s is the scattered power and dA_s is the average scattering cross-section of the targets. This cross section is given (in spherical coordinates) by

$$dA_s = \eta\; dV = \eta\; r^2\; \sin\theta\; d\theta\; d\phi\; dr \; ; \tag{A5}$$

where η is the radar reflectivity (expressed in units of m^{-1}). Variable η is also called the scatterer cross-section per unit volume, and it assumes that power is scattered isotropically with an intensity equal to that of the backscattered radiation [e.g., *Hocking*, 1985].

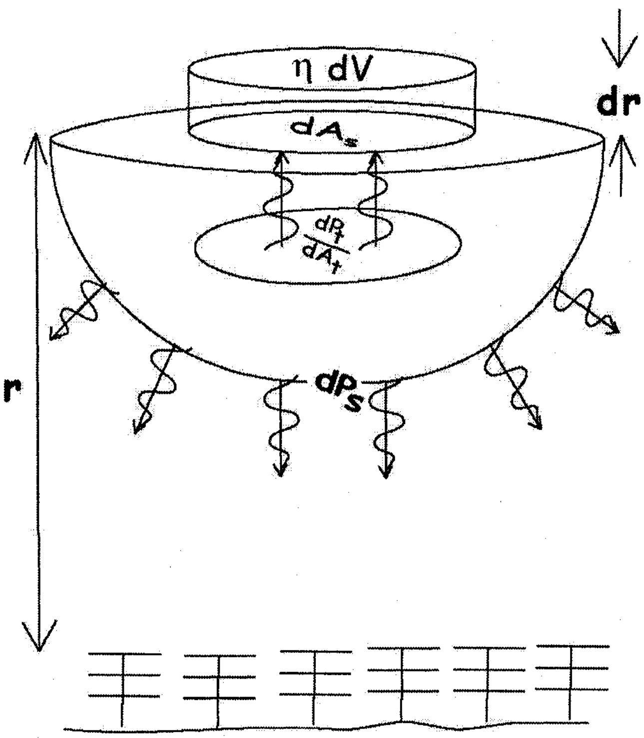

Figure A2. Scattering of a radar transmitted signal.

During reception of the backscattering power into the antenna (Figure A3), the following relation applies for the scattered power flux:

$$\frac{dP_r}{A_e} = \frac{dP_s}{4\,\pi\,r^2}\ ; \tag{A6}$$

where A_e is the effective area of the radar antenna, and it is given by [e.g., *Skolnik*, 1990, equation (6.8)]

$$A_e = \frac{D\,\lambda^2}{4\pi}\ . \tag{A7}$$

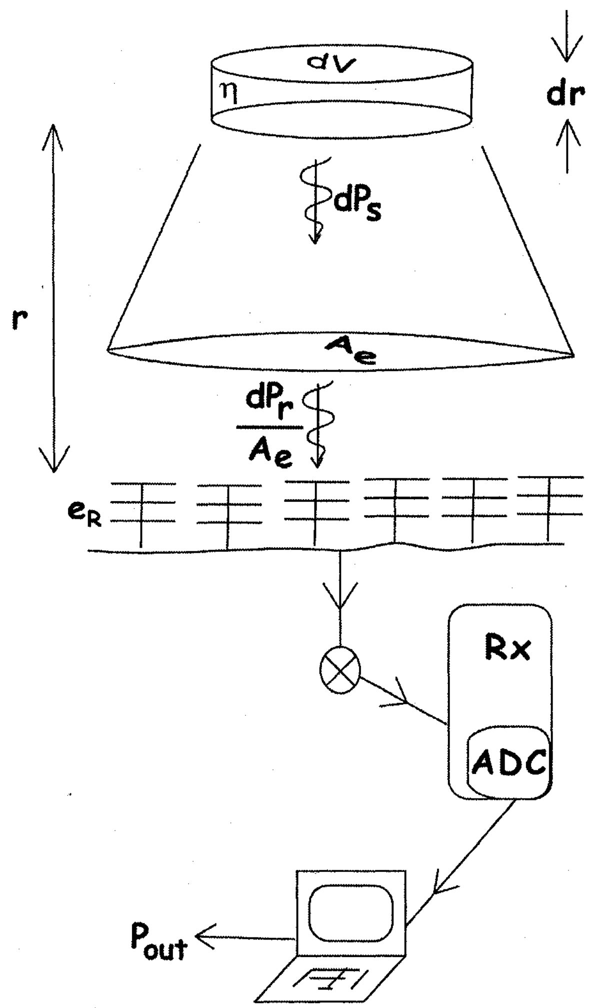

Figure A3. Reception of a radar transmitted signal.

In this analysis, we do not need to consider the antenna efficiency during reception, e_R. Instead, we consider this efficiency during our calibration procedure (described in Chapter 2), when applying the conversion between the backscatter power input into the antennas, P_r, and the power output by the radar signal processing, P_{out}.

By combining equations (A2) to (A7), we obtain the following expression:

$$dP_r = \frac{P_{Tx}\ e_T\ (D_{\max})^2\ [F(\theta,\phi)]^2\ \lambda^2\ \eta\ \sin\theta\ d\phi\ d\theta\ dr}{(4\pi)^3\ r^2}\ . \tag{A8}$$

In order to obtain the radar equation, let us solve equation (A8) within the limits of a volume confined into a given range gate. This implies that

$$P_r = \frac{P_{Tx}\, e_T\, (D_{\max})^2\, \lambda^2}{(4\pi)^3} \int_{r=R-L/4}^{R+L/4} \int_{\phi=0}^{2\pi} \int_{\theta=0}^{\pi} \frac{\eta(r,\theta,\phi)\,[F(\theta,\phi)]^2 \sin\theta}{r^2}\, d\theta\, d\phi\, dr \ ; \tag{A9}$$

where L is the transmitted pulse length (expressed in units of meters), and $L/2$ is the range resolution. The range gate is centered at R, and the values R - $L/4$ and R + $L/4$ correspond to the radial boundaries of our range gate (near-range and far-range boundaries, respectively). In equation (A8), $r^{-2}\,\eta$ is usually convolved with the shape of the transmitted pulse. This is so because the received signal is a convolution between the reflectivity profile and the radar transmitted pulse [e.g., *Hocking and Rottger*, 1983, section 4]. For simplicity, we approximate here the transmitted pulse as a square pulse, and this implies that the convolution between $r^{-2}\,\eta$ and the pulse is such that

$$\frac{\eta(r,\theta,\phi)}{r^2} \otimes g(r) \cong \frac{\eta(r,\theta,\phi)}{r^2} \ ; \tag{A10}$$

where the symbol $\otimes$ represents a convolution, and $g(r)$ describes the transmitted pulse as a function of range r.

When considering the second range gate, strictly speaking, P_t would not be the one given by equation (A2). Instead, it would be only the power that passes the first range gate without being backscattered (i.e., the power incident into the first range gate minus the power backscattered in this same first gate). However, for any given range gate, the power scattered is six or more orders of magnitude smaller than the incident power. Therefore, it is safe to assume that the incident power (per unit solid angle) at any given range gate is the same as the power (per unit solid angle) incident into the very first range gate, i.e., the one given by equation (A2). This is known as the Born approximation [e.g., *Ulaby et al.*, 1986, p.1066]. Therefore, equation (A9) is still valid for any range gate.

REFERENCES:

AMS (2000), *Glossary of Meteorology*, II edition, American Meteorological Society, Boston, MA, USA, 850 pp., available at "amsglossary.allenpress.com/glossary".

Atlas, D., K.R. Hardy, and K. Naito (1966), Optimizing the radar detection of clear air turbulence, *Journal of Applied Meteorology*, 5, 450-460.

Balsley, B.B., and K.S. Gage (1980), The MST radar technique: Potential for middle atmospheric studies, *Pure and Applied Geophysics*, 118, 452-493.

Battan, L.J. (1973), *Radar Observation of the Atmosphere*, The University of Chicago Press, Chicago, USA, 324 pp.

Beard, K.V. (1985), Simple Altitude Adjustments to Raindrop Velocities for Doppler Radar Analysis, *Journal of Atmospheric and Oceanic Technology*, 2, 468-471.

Benjamin, S.G., B.E. Schwartz, E.J. Szoke, and S.E. Koch (2004), The Value of Wind Profiler Data in U.S. Weather Forecasting, *Bulletin of the American Meteorological Society*, 85(12), 1871–1886.

Blue, M.D. (1980), Permittivity of ice and water at millimeter wavelengths, *Journal of Geophysical Research*, 85, C2, 1101-1106.

Booker, H.G., and W.E. Gordon (1950), Theory of radio scattering in the troposphere, *Proceedings of the IEEE*, 38, 401-421.

Boyer, E., M. Petitdidier, W. Corneil, C. Adnet, and P. Larzabal (2001), Application of model-based spectral analysis to wind-profiler radar observations, *Annales Geophysicae*, 19, 815-824.

Campistron, B., G. Despaux, M. Lothon, V. Klaus, Y. Pointin, and M. Mauprivez (2001), A partial 45 MHz sky temperature map obtained from the observations of five ST radars. *Annales Geophysicae*, *19*(8), 863-871.

Campos, E.F. (1998), Measurements of raindrop size distributions by three different sensors, *M.Sc. thesis*, Department of Atmospheric and Oceanic Sciences, McGill University, 96 pp.

Campos, E. F., and W. Hocking (2003), Vortical motions observed with the new McGill VHF radar and associated dynamical characteristics, in *MST10: Proceedings of the Tenth International Workshop on Technical and Scientific Aspects of MST Radar*, edited by J. Chau, J. Lau, and J. Röttger, pp. 415-418, Radio Observatorio de Jicamarca, Lima, Peru.

Campos, E., and I. Zawadzki (2000), Instrumental Uncertainties in Z-R Relations, *Journal of Applied Meteorology*, 39, 1088-1102.

Chilson, P.B, C.W. Ulbrich, M.F. Larsen, P. Perillat, and J.E. Keener (1993), Observations of a Tropical Thunderstorm Using a Vertically Pointing, Dual-Frequency, Collinear Beam Doppler Radar, *Journal of Atmospheric and Oceanic Technology*, 10, 663-673.

Chu, Yen-Hsyang, and Chun-Hsien Lin (1994), The severe depletion of turbulent echo power in precipitation observed using the Chung-Li VHF Doppler radar, *Radio Science*, 29, 1311-1320.

Cohn, S.A., R.R. Rogers, S. Jascourt, W.L. Ecklund, D.A. Carter, and J.S. Wilson (1995), Interactions between clear-air reflective layers and rain observed with a boundary layer wind profiler, *Radio Science*, 30, 323-341.

Debye, P. (1929), *Polar Molecules*, Dover Publications, New York, USA,172 pp.

Doviak, R.J., and D.S. Zrnic (1993), *Doppler Radar and Weather Observations*, Second Edition, Academic Press, Inc., San Diego, California, USA, 562 pp.

Fabry, F. (1996), On the determination of scale ranges for precipitation fields, *Journal of Geophysical Research*, 101(D8), 12819-12826.

Fabry, F., and I. Zawadzki (1995), Long-Term Radar Observations of the Melting Layer of Precipitation and Their Interpretation, *Journal of the Atmospheric Sciences*, 52, 838-851.

Fernández, D.P., A.R.H. Goodwin, E.W. Lemmon, J.M.H. Levelt-Sengers, and R.C. Williams (1997), A Formulation for the Static Permitivity of Water and Steam at Temperatures from 238 K to 873 K at Pressures up to 1200 MPa including Derivatives and Debye-Hückel Coefficients, *Journal of Physical and Chemical Reference Data*, 26, 1125-1169.

Friend, A.W. (1949), Theory and practice of tropospheric sounding by radar, *Proceedings of the IEEE*, 37, 116-138.

Gage, K. S. (1990), Radar Observations of the Free Atmosphere: Structure and Dynamics, in *Radar in Meteorology*, edited by David Atlas, pp. 534-574, American Meteorological Society, Boston, MA, USA.

Gage, K.S., and B.B. Balsley (1980), On the scattering and reflection mechanisms contributing to clear air radar echoes from the troposphere, stratosphere, and mesosphere, *Radio Science*, 15(2), 243-257.

Gage, K. S., and E. E. Gossard (2003), Recent Developments in Observations, Modeling, and Understanding Atmospheric Turbulence and Waves, in *Radar and Atmospheric Science: A Collection of Essays in Honor of David Atlas*, edited by R. M. Wakimoto and R. C. Srivastava, pp. 139-174, Meteorological Monographs #52, American Meteorological Society, Boston, Massachusetts, USA.

Gage, K.S., C.R. Williams, P.E. Johnston, W.L. Ecklund, R. Cifelli, A. Tokay, and D. Carter (2000), Doppler Radar Profilers as Calibration Tools for Scanning Radars, *Journal of Applied Meteorology*, 39, 2209-2222.

Gossard, E.E., R.B. Chadwick, W.D. Neff, and K.P. Moran (1982) The use of ground-based Doppler radars to measure gradients, fluxes and structure parameters in elevated layers, *Journal of Applied Meteorology*, 21, 211-226.

Green, J. L., W. L. Clark, J. M. Warnock, and K. J. Ruth (1983), Absolute calibrations of MST/ST Radars, in *Preprints of the 21st Conference on Radar Meteorology, Edmonton, Alta., Canada*, pp. 144-147, American Meteorological Society, Boston, Massachusetts, USA.

Gunn, K.L.S., and G.D. Kinzer (1949), The terminal velocity of fall for water drops in stagnant air, *Journal of Meteorology*, 6, 243-248.

Hippel, A.R.V., editor (1961), *Dielectric Materials and Applications*, The Technology Press of MIT and John Wiley & Sons, Inc., New York, USA, 361-367.

Hocking, W.K. (1983), On the extraction of atmospheric turbulence parameters from radar backscatter Doppler Spectra –I. Theory, *Journal of Atmospheric and Terrestrial Physics*, 45(2/3), 89-102.

Hocking, W. K. (1985), Measurement of turbulent energy dissipation rates in the middle atmosphere by radar techniques: A review, *Radio Science*, 20(6), 1403-1422.

Hocking, W. K. (1997), System design, signal-processing procedures, and preliminary results fro the Canadian (London, Ontario) VHF atmospheric radar, *Radio Science*, 32(2), 687-706.

Hocking, W.K. (1997b), Strengths and limitations of MST radar measurements of middle-atmosphere winds, *Annales Geophysicae*, 15, 1111-1122.

Hocking, W.K., and A.M. Hamza (1997), A quantitative measure of the degree of anisotropy of turbulence in terms of atmospheric parameters, with particular relevance to radar studies, *Journal of Atmospheric and Solar-Terrestrial Physics*, 59(9), 1011-1020.

Hocking, W.K, and J. Rottger (1983), Pulse length dependence of radar signal strengths for Fresnel backscatter, *Radio Science*, 18, 1312-1324.

Hocking, W.K., and R.A. Vincent (1982), Comparative Observations of D Region HF Partial Reflections at 2 and 6 MHz, *Journal of Geophysical Research*, 87(A9), 7615-7624.

Hocking, W. K., G. Schmidt, and P. Czechowsky (1983), Absolute Calibration of the SOUSY VHF Stationary Radar, *Internal Report MPAE-W-00-83-14*, 16 pp., Max-Planck-Institut für Aeronomie, Katlenburg-Lindau, Germany.

ICAO (1993), *Manual of the ICAO Standard Atmosphere extended to 80 km (262 500 feet)*, III Edition (Doc 7488), International Civil Aeronautical Organization, available on Compact Disk.

Knight, C.A., and L.J. Miller (1998), Early Radar Echoes from Small, Warm Cumulus: Bragg and Hydrometeor Scattering, *Journal of the Atmospheric Sciences*, 55, 2974-2992.

Kobayashi, T., and A. Adachi (2005), Retrieval of Arbitrary Shaped Raindrop Size Distributions from Wind Profiler Measurements, *Journal of Atmospheric and Oceanic Technology*, 22, 433-442.

Kropfli, R.A., I. Katz, T.G. Konrad, and E.B. Dobson (1968), Simultaneous radar reflectivity measurements and refractive index spectra in the clear atmosphere, *Radio Science*, 3, 991-994.

Lang, K. R. (1999), *Astrophysical Formulae, Vol. II: Space, Time, Matter and Cosmology*, 3rd Enlarged and Revised Edition, 436 pp., Springer-Verlag, Berlin, Germany.

Lee, G., and I. Zawadzki (2005), Variability of Drop Size Distributions: Time-Scale Dependence of the Variability and Its Effects on Rain Estimation, *Journal of Applied Meteorology*, 44, 241-255.

Léna, P., F. Lebrun, and F. Mignard (1998), *Observational Astrophysics*, Translated by S. Lyle, Second Revised and Enlarged Edition, 512 pp., Springer-Verlag, Berlin, Germany.

Liebe, H. J., G.A. Hufford, and T. Manabe (1991), A Model for the Complex Permittivity of Water at Frequencies below 1 THz, *International Journal of Infrared and Millimeter Waves*, 12(7), 659-675.

Lucas, C., A.D. MacKinnon, R.A. Vincent, and P.T. May (2004), Raindrop Size Distribution Retrievals from a VHF Boundary Layer Profiler, *Journal of Atmospheric and Oceanic Technology*, 21, 45-60.

Lyons, R.G. (1997), *Understanding Digital Signal Processing*. Addison Wesley Longman, Inc. Reading, Massachusetts, USA. 517pp.

Maguire II, W.B., and S.K. Avery (1994), Retrieval of Raindrop Size Distributions Using Two Doppler Wind Profilers: Model Sensitivity Testing, *Journal of Applied Meteorology*, 33, 1623-1635.

Mardoc, Inc. (2002), *WindTracker Radar Operation Manual*, Version 1.1, Edited by A. Hocking, Modular Antenna Radar Designs of Canada, London, Ontario, Canada, 105 pp.

Marshall, J.S., and K.L.S. Gunn (1952), Measurement of snow parameters by radar, *Journal of Meteorology*, 9, 322-327.

McDonald, A.J., T.K. Carey-Smith, D.A. Hooper, G.J. Fraser, and B.P. Lublow (2004), The effect of precipitation on wind-profiler clear air returns, *Annales Geophysicae*, 22, 3959-3970.

Megaw, E.C.S. (1957), Fundamental radio scatter propagation theory, *Proceedings of the IEEE*, 104, 441-456.

Meischner, P., R. Baumann, H. Höller, and T. Jank (2001), Eddy dissipation rates in thunderstorms estimated by Doppler radar in relation to aircraft in situ measurements, *Journal of Atmospheric and Oceanic Technology*, 18, 1609-1627.

Milogradov-Turin, J., and F. G. Smith (1973), A Survey of the Radio Background at 38 MHz, *Monthly Notices of the Royal Astronomical Society*, *161*(3), 269-279.

Mohr, P. J., and B. N. Taylor (2003), The Fundamental Physical Constants, *Physics Today*, *56*(8), BG6-BG13, American Institute of Physics, Melville, NY, USA.

Nautical Almanac Offices, US Naval Observatory, and UK Rutherford Appleton Laboratory (2003), *The Astronomical Almanac for the year 2003*, U.S. Naval Observatory, Washington, D.C., USA.

Ottersten, H. (1969), Atmospheric structure and radar backscattering in clear air, *Radio Science*, 4, 1179-1193.

Ottersten, H. (1969b), Mean vertical gradient of potential refractive index in turbulent mixing, and radar detection of CAT, *Radio Science*, 4, 1247-1249.

Ottersten, H. (1969c), Radar backscattering from the turbulent clear atmosphere, *Radio Science*, 4, 1251-1255.

Press, W. H., B. P. Flannery, S. A. Teukolsky, and W. T. Vetterling (1986), *Numerical Recipes: The Art of Scientific Computing*, 818 pp., Cambridge University Press, New York, USA.

Probert-Jones, J.R. (1962), The radar equation in meteorology, *Quarterly Journal of the Royal Meteorological Society*, 88, 485-495.

Pruppacker, H.R., and J.D. Klett (1997), *Microphysics of Clouds and Precipitation*, 2nd revised and enlarged edition, 955 pp., Kluwer Academic Publishers, Dordrecht, the Netherlands.

Rajopadhyaya, D., P.T. May, and R.A. Vincent (1993), A General Approach to the Retrieval of Raindrop Size Distributions from Wind Profiler Doppler Spectra: Modeling Results, *Journal of Atmospheric and Oceanic Technology*, 10, 710-717.

Ralph, F.M. (1995), Using Radar-Measured Radial Vertical Velocities to Distinguish Precipitation Scattering from Clear-Air Scattering, *Journal of Atmospheric and Oceanic Technology*, 12, 257-267.

Research Systems, Inc. (2002), *Using IDL*, Manual for IDL Version 5.6, Edited by Research Systems, Inc., Boulder, Colorado, USA. 716 pp.

Rinehart, R.E. (1997), *Radar For Meteorologists*, Third Edition, 428 pp., Rinehart Publishing, Grand Forks, North Dakota, USA.

Roger, R. S., C. H. Costain, T. L. Landecker, and C. M. Swerdlyk (1999), The radio emission from the galaxy at 22 MHz, *Astronomy and Astrophysics Supplement Series*, *137*(1), 7-19.

Rogers, R.R. (1971), The effect of variable target reflectivity on weather radar measurements, *Quarterly Journal of the Royal Meteorological Society*, 97, 154-167.

Rogers, R.R., and M.K. Yau (1989), *A Short Course in Cloud Physics*, Third Edition, 293 pp., Pergamon Press, Oxford, England.

Rogers, R.R., S.A. Cohn, W.L. Ecklund, J.S. Wilson, and D.A. Carter (1994), Experience form one year of operating a boundary-layer profiler in the center of a large city, *Annales Geophysicae*, 12, 529-540.

Röttger, J., and M.F. Larsen (1990), UHF/VHF Radar Techniques for Atmospheric Research and Wind Profiler Applications, in *Radar in*

Meteorology, edited by David Atlas, pp. 235-281, American Meteorological Society, Boston, MA, USA.

Röttger, J., and G. Schmidt (1979), High-resolution VHF radar sounding of the troposphere and stratosphere, *IEEE Transactions on Geoscience Electronics*, GE-17, 182-189.

Schafer, R., S. Avery, P. May, D. Rajopadhyaya, and C. Williams (2002), Estimation of Rainfall Drop Size Distributions from Dual-Frequency Wind Profiler Spectra Using Deconvolution and a Nonlinear Least Squares Fitting Technique, *Journal of Atmospheric and Oceanic Technology*, 19, 864-874.

Sheppard, B.E. (1990), Measurement of raindrop size distributions using a small Doppler radar, *Journal of Atmospheric and Oceanic Technology*, 7, 255-268.

Silverman, R.A. (1956), Turbulent mixing theory applied to radio scattering, *Journal of Applied Physics*, 27, 699-705.

Skolnik, M.I., editor (1990), *Radar Handbook*, Second Edition, McGraw-Hill, available at "http://www.knovel.com/knovel2/Toc.jsp?BookID=701".

Smith, P.L. (1984), Equivalent Radar Reflectivity Factors for Snow and Ice Particles, *Journal of Climate and Applied Meteorology*, 23, 1258-1260.

Subramanian, K. R. (2004), Brightness temperature and size of the quiet Sun at 34.5 MHz, *Astronomy and Astrophysics*, 426, 329-331.

Tatarski, V.I. (1961), *Wave Propagation in a Turbulent Medium*, Translated by R. A. Silverman, McGraw-Hill Book Company, Inc., New York, N.Y., USA, 285 pp.

Taylor, G.I. (1938), The spectrum of turbulence. *Proceedings of the Royal Society of London*, Series A, Mathematical and Physical Sciences, 164, 476-490.

Ulaby, F. T., R. K. Moore, and A. K. Fung (1981), *Microwave remote sensing active and passive, Volume 1: Microwave Remote Sensing Fundamentals and Radiometry*, 456 pp., Addison-Wesley Publishing Company, Massachusetts, USA.

Ulaby, F. T., R.K. Moore, and A.K. Fung (1986), *Microwave Remote Sensing, Active and Passive*, Volume III: From Theory to Applications, Addison-Wesley Publishing Company, 1117 pp.

Van Zandt, T.E., J. L. Green, K.S. Gage, and W.L. Clark (1978), Vertical profiles of refractivity turbulence structure constant: Comparison of observations by the sunset radar with a new theoretical model, *Radio Science*, 13, 819-829.

Wakasugi, K., A. Mizutani, M. Matsuo, S. Fukao, and S. Kato (1986), A Direct Method for Deriving Drop-Size Distribution and Vertical Air Velocities from VHF Doppler Radar Spectra. *Journal of the Atmospheric and Oceanic Technology*, 3, pp. 623-629.

Weinstock, J. (1978), Vertical turbulent diffusion in a stably stratified fluid, *Journal of the Atmospheric Sciences*, 35, 1022-1027.

White, A.B., C.W. Fairall, A.S. Frisch, B.W. Orr, and J.B. Snider (1996), Recent radar measurements of turbulence and microphysical parameters in marine boundary layer clouds, *Atmospheric Research*, 40, 177-221.

Zawadzki, I. (1982), The Quantitative Interpretation of Weather Radar Measurements, *Atmosphere and Ocean*, 20(2), 158-180.

Zawadzki, I., F. Fabry, and W. Szyrmer (2001), Observations of supercooled water and secondary ice generation by a vertically pointing X-band Doppler radar, *Atmospheric Research*, 59-60, 343-359.